

Exploring Strategies for Implementing Negative Inertia on The Shoulder Elbow Perturbator

Salkan Osamah (5769523)

*Department of Biomechanical Engineering, Faculty of Mechanical Engineering,
TU Delft, The Netherlands*

August 20, 2024

Abstract—This research investigates methodologies to reduce and implement negative inertia in robots for upper extremity diagnostics and rehabilitation. The robot’s responsiveness is enhanced by integrating accelerometers and Kalman filters into the control scheme, ensuring smoother physical human-robot interactions. A force gain that mimics negative inertia significantly improves system dynamics within the admittance control framework. Introducing dead zones for force and acceleration stabilizes responses at lower rendered inertia, crucial for handling spastic conditions. However, this research identifies a lack of standardized evaluation methods for negative inertia and highlights hardware constraints, such as bandwidth limitations, that restrict performance. Future research should focus on establishing evaluation standards and optimizing hardware to refine control precision. This work demonstrates the potential of advanced control strategies to optimize robotic rehabilitation, paving the way for more effective diagnostic and therapeutic interventions.

Index Terms—Rehabilitation Robotics; Physical Human-Robot Interaction; Transparency; Inertia Compensation; Negative Inertia;

I. INTRODUCTION

Each year, more than 13.7 million individuals worldwide suffer strokes, with the elderly being particularly vulnerable [1]. In The Netherlands, strokes account for approximately 9,300 deaths annually [2]. Moreover, nearly two-thirds of stroke survivors endure partial motor control loss, significantly affecting their quality of life [3, 4]. Along with cerebral palsy, strokes remain the leading cause of motor impairments, while conditions like Guillain-Barré Syndrome and traumatic brain injuries also contribute to neuromotor deficits [5, 6]. Many patients, however, can recover some motor control through intensive Neurotherapy, which promotes neuroplasticity—the brain’s ability to reorganize and form new neural pathways. Despite these advancements, the complexity of diagnosing motor impairments and the intensive nature of therapy sessions place a significant strain on healthcare resources, compounding the shortage of qualified therapists. Consequently, there is an increasing demand for robotic alternatives to bridge the gap.

A. Robots in Rehab

Robotic systems offer a promising solution to the shortage of qualified therapists and clinicians complementing traditional therapy methods. These systems, shown in Figure 1 can perform continuous observation, online analysis, and decision-making, reducing the physical demands on therapists and

allowing them to focus on more complex aspects of therapy such as treatment planning and efficacy observation.[7] Robots can provide high-intensity training and quantitative analysis, potentially improving therapy quality and efficiency. This allows therapists to treat more patients, addressing the emerging shortage of healthcare professionals.[8]

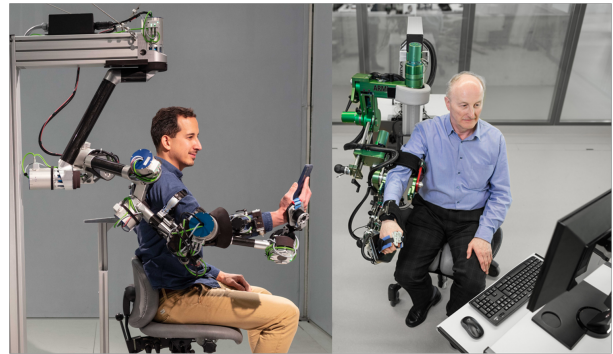


Fig. 1: The Anyexo diagnostic and rehabilitation exoskeleton (left) and the Armin V rehab robot (right).[7, 8]

1) *Mechanical Transparency in Rehab Robots:* For robotic systems to effectively aid in the rehabilitation of upper extremity motor function impairments, they must exhibit mechanical transparency. Mechanical transparency in physical human-robot interaction (pHRI) ensures that the robot transmits the correct amount of supportive or resistive force to the patient without introducing unnecessary interference. This is crucial for the patient’s inter-joint coordination and overall rehabilitation success. Various studies have shown that training with transparent robotic systems fosters motor recovery by providing consistent and precise assistance. [9–12]

2) *Evaluation Methods for Transparency:* Despite the importance of mechanical transparency, there is no standard procedure for its quantitative evaluation.[13] Different methods have been used to assess transparency. For instance, the Lokomat system uses RMS interaction torques to estimate transparency during gait rehabilitation. [14] Other systems, like the FLOAT robot, assess transparency by evaluating the deviation from desired interaction forces at different velocities and levels of body weight support.[15] In arm rehabilitation, transparency assessments often involve measuring forces exerted by the exoskeleton and analyzing these forces at the sensor level. [16] However, this approach can be influenced by misalignment

effects and passive tissue deformations, necessitating a more refined analysis at the joint level.

B. Negative Inertia in Diagnostic Robots

Negative inertia can decrease the perceived weight and resistance of robotic systems, facilitating the identification of limb properties and the accurate diagnosis of impairments by clinicians. [17, 18] Negative inertia refers to a control strategy that artificially reduces the mass and resistance experienced by the user during interaction with a robotic system. This technique enables more precise assessments of patient limb function and supports effective rehabilitation. This research systematically explores inertia-minimizing techniques to develop an exploratory strategy for implementing negative inertia on the Shoulder Elbow Perturbator (SEP). The primary focus of this research is to enhance mechanical transparency and improve diagnostic outcomes by applying negative inertia to the SEP.

C. Structure

This research is structured as follows: Section II provides the background, discussing the existing literature on control strategies, including feedforward and feedback mechanisms, inertia compensation techniques, and the hardware used. Section III details the methods employed, covering experiments such as system modelling and identification, servo tuning, the integration of additional sensors, and the implementation of the admittance controller with negative inertia. Section IV presents the results obtained from these experiments. Finally, Section V offers a discussion of the results, analyzing their implications and relevance to the field. Section VI looks ahead to possible eventualities of this research in diagnostic robots.

D. Research Goal

The primary objective of this research is to assess and reduce the inertia of the Shoulder Elbow Perturbator (SEP) robot, a single-degree-of-freedom (DoF) system equipped with a force/torque sensor at its end effector. This research will compare the performance of a controller implementing negative inertia with one that does not. By systematically analyzing different strategies, this research aims to enhance the effectiveness of robotic diagnostic systems and contribute to better clinical outcomes for patients with upper motor function impairments.

A review of the current literature reveals that strategies for implementing negative inertia largely depend on the complexity of the robots and the ability to accurately model their dynamic behaviour. Exoskeletons and multi-DoF robots increasingly rely on feedback and disturbance observer-based inertia compensation. However, since this research focuses on implementing negative inertia on a single active DoF diagnostic robot, a feedforward approach could yield promising results. Thus, the research question becomes:

"What strategies can effectively mitigate inertial and other undesired dynamics while implementing negative inertia on the Shoulder Elbow Perturbator?"

To answer the research question, the following sub-objectives have been formulated.

- 1) *Assess the Feasibility of Using Piezoelectric Force Sensors:* Evaluate the use of piezoelectric force sensors for both admittance control and as disturbance observers in implementing negative inertia.
- 2) *Implement Admittance Control:* Establish adequate admittance control on the SEP as a prerequisite for enabling negative inertia.
- 3) *Utilize Accelerometers for Position Feedback:* Evaluate the effectiveness of using accelerometers in combination with encoders for position feedback.
- 4) *Identify Limiting Factors:* Determine the limiting factors, such as time delays or controller/sensor bandwidths, for developing an effective negative inertia framework.

II. BACKGROUND

A. Controllers in Rehab Robotics

There are two distinct categories of classification when exploring robots within the domain of healthcare on human movements. These are rehabilitative robots, designed to replace or augment physiotherapists. These robots can provide repetitive movements to isolated joints or more often provide assisted compound movements to multiple joints to mimic natural movements during activities of daily living (ADL).[19, 20] On the other hand are diagnostic robots, aimed at assisting clinicians assess neurological or muscular impairment quicker. These devices are purpose-built often focusing on a singular movement or a particular joint to effectively allow for accurate identification of human limb properties like spasticity, joint viscosity and muscle weakness or muscle synergies. [21, 22]

The controllers designed therefore vary with the purpose of the devices. Some are more stringent and robust against external disturbances coming from the environment or human interaction in this case while others rely on these disturbances to enable accurate modelling.

B. Admittance or Impedance

Two popular techniques for managing human-robot interactions are impedance and admittance controllers. Both regulate the robot's dynamic behaviour, ensuring safety, precision, and adaptability to external forces.

1) *Impedance control:* focuses on the relationship between detected motion and the force applied, either through open or closed-loop control. Here, the robot behaves as a mechanical impedance, akin to a second-order mass-spring-damper system. The objective is to control the robot's response to external motions to achieve the desired dynamic behaviour. The equations of motion for such a system are:

$$F = M\ddot{x} + B\dot{x} + Kx \quad (1)$$

where F is the force, x is the displacement and M, B, K represent the desired inertia, damping and stiffness respectively.

Impedance control excels in scenarios where the robot interacts with varying and unpredictable forces, providing robust regulation of interaction dynamics, and ensuring stability and

responsiveness. It is ideal for applications requiring precise force control, such as surgical robots, robotic rehabilitation, teleoperation, and haptic rendering. [23]

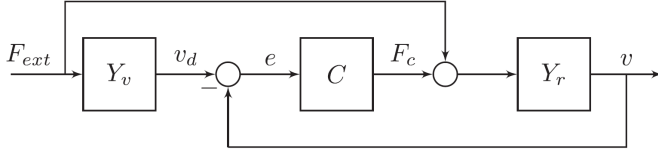


Fig. 2: The admittance control diagram illustrates the interaction between the robot dynamics, external forces, virtual dynamics, and the control system. The externally applied force F_{ext} influences the robot dynamics Y_r and passes through the virtual dynamics Y_v to generate a velocity reference v_d . The controller C enforces this velocity reference by generating a control force F_c , which is applied to the robot. The resulting motion of the robot is denoted as v . [24]

2) *Admittance control*: the inverse of impedance control, illustrated in Figure 2, focuses on the relationship between measured force and the velocity reference, determining how much a robot displaces after being perturbed by an applied force. The governing equation of motion is:

$$x = \frac{1}{M} \iint F dt + \frac{1}{B} \int F dt + \frac{1}{K} F \quad (2)$$

where, x is the displacement, F is the force and M, B, K are the inertia, damping and compliance (inverse of stiffness) respectively.

Admittance control is advantageous when the robot needs to follow specific trajectories or paths precisely in response to external forces, allowing for smoother and more compliant interactions. This makes it ideal for collaborative, assistive robots, or delicate tasks such as diagnosing upper extremity paresis.[25]

The choice between admittance and impedance control in human-robot interaction (HRI) depends on the specific application needs. Impedance control is favoured for managing how robots react to external forces, ensuring stability and adaptability. Admittance control excels in making robots follow precise motion trajectories in response to forces. Advanced HRI systems often combine both strategies to balance force responsiveness and motion precision, enhancing interaction versatility and safety. While impedance control provides robustness in modifying dynamic responses, admittance control is particularly suitable for applications like the Shoulder Elbow Perturbator (SEP), benefiting from negative inertia during dynamic interactions by enabling precise control and compensation for dynamic behaviour. [25, 26]

C. Feedforward or Feedback

Feedforward methodologies predict control inputs based on system models and expected user interactions, bypassing continuous feedback. These controllers leverage known disturbances like inertia, gravity, and friction to enhance transparency and accuracy, especially in rehabilitative movements.

While they improve trajectory tracking and disturbance compensation, inaccuracies in models can cause jittering and oscillations. Feedforward control avoids the high computational costs of differentiating position data to obtain velocity and acceleration.

In rehabilitative robotics, trajectory planning pre-programmed movement paths to minimize resistance, while inverse dynamics control calculates joint torques to preemptively apply necessary forces. In diagnostic robotics, model-based feedforward control uses detailed system models for precise control inputs, and learning-based control uses past data to predict and apply these inputs, effectively for repetitive tasks. [27]

Feedback-based methodologies rely on real-time sensor data to dynamically adjust the robot's behaviour. Disturbance observers estimate and compensate for influences like gravity and friction in real-time, offering robustness and adaptability. However, their effectiveness depends on accurate, high-rate sensors to minimize delays, and stability can be a concern. [28, 29]

In rehabilitative robotics, Proportional-Derivative (PD) control adjusts forces based on position and velocity feedback, reducing perceived inertia. Impedance control modifies the force-movement relationship to simulate lower inertia, smoothing patient movements. In diagnostic robotics, adaptive control tailors robot behaviour based on user movements, while Model Predictive Control (MPC) uses real-time feedback and predictive models for precise neuromuscular assessments.

The choice between feedforward and feedback control depends on application needs. Feedforward models excel with accurate dynamic modelling and precise trajectory tracking, while disturbance observers handle dynamic, unpredictable interactions better. Diagnostic devices benefit from enhanced transparency for assessing limb dynamics and properties like spasticity and muscle weakness.

Recent exoskeletal devices, such as ARMin IV+ and ANYexo 2.0, combine feedforward terms with disturbance observers, reflecting an evolving hybrid control strategy. [7, 8]

Feedback-based methods offer high precision and adaptability for dynamic rehabilitation but require extensive sensor integration and real-time processing, increasing complexity and cost. Feedforward methods suit predictable, repetitive diagnostic tasks but struggle with real-time adaptation, relying on accurate system models.

Other approaches, including sensorless and AI-based methods, balance simplicity, adaptability, and user experience. Sensorless methods are easier to implement but lack fine-tuned control. AI-based methods, while resource-intensive, provide high adaptability and precision, tailoring interactions to individual users.

D. Inertia Compensation

Implementing negative inertia in an impedance controller requires precise tuning to avoid instability. The system must have sufficient damping and safeguards to handle reduced effective inertia without oscillations or undesired behaviours,

TABLE I: Guidelines to minimising inertia

	Guideline	Effects
1	Feedforward Control	Effectively reduces the inherent inertia needed to be reduced by the admittance controller
2	No Force Filtering	Adds delays and excessive phase lag on the virtual dynamics
3	Minimising post-sensor inertia	Reduces apparent inertia but reduces coupled stability
4	Use Virtual Damping	Better tracking at low frequency, ideal for HRI
5	Velocity Loop Gain High	Pushes phase lag to higher frequencies, increases coupled stability
6	Optimise robotic stiffness	Internal Eigen modes introduce phase lags between force and velocity sensor measurements

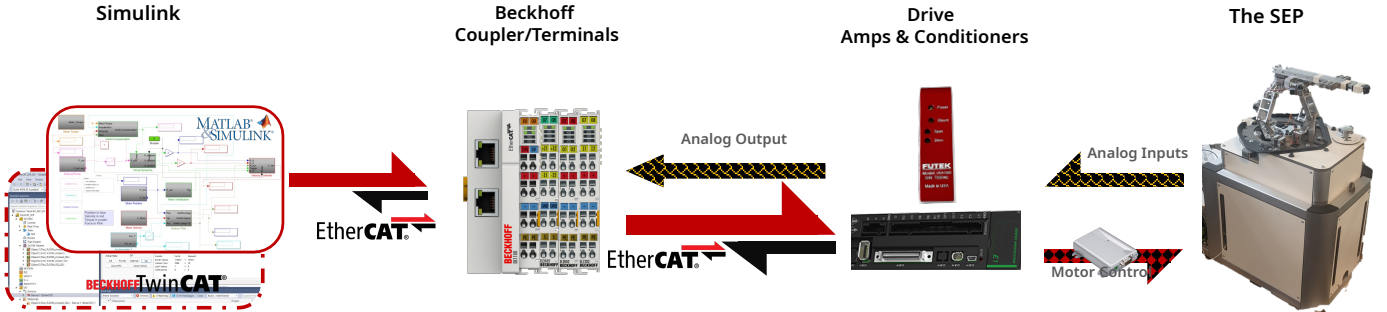


Fig. 3: The flow process of the Amsterdam SEP, from the Simulink model running on the back of TwinCAT3 to the Beckhoff terminals to the signal conditioners, motor drive and finally to the servo motor and sensors(from left to right).

such as "blowing up." This necessitates highly responsive and precise force and position sensors to accurately implement and monitor inertial deviations. Sensors with high bandwidths increase computational loads, requiring real-time target PCs for rapid inertial adjustment calculations.

In the Laplace domain, this is represented as:

$$F(s) = [(M_{\text{desired}} - M_{\text{virtual}})s^2 + Bs + K] X(s) \quad (3)$$

In an admittance controller, modifying the robot's motion response to applied forces gives the effect of reduced or negative inertia. Implementing negative inertia is simpler, as it involves adjusting the motion response rather than the force response. Precise force sensors are still needed but do not require extremely high bandwidths. Computational loads are often reduced since the controller processes motion responses to force inputs rather than force adjustments. In the Laplace domain, this is represented as:

$$X(s) = \left[\frac{1}{(M_{\text{desired}} - M_{\text{virtual}})s^2 + Bs + K} \right] F(s) \quad (4)$$

Therefore, following the six guidelines set out by Keemink et al, 2018. The inertial mitigation techniques will be implemented where possible on the Amsterdam SEP. [24] The guidelines are laid out in Table I.

E. The Hardware

The Shoulder Elbow Perturbators (SEP) trace their origins to the ACT4D haptic manipulator, built upon the ACT3D haptic master from MOOG (New York, USA) [30]. The SEP, developed by Hankamp Rehab (Eindhoven, The Netherlands) [31], perturbs the elbow joint while passively supporting the arm via a Sarrus linkage mechanism. This mechanism, using a cable-spring system routed through pulleys, provides gravity

compensation independent of height, which can be adjusted for users with an integrated jack and spring preload. Perturbations are delivered by a high-torque rotary table (HIWIN TMS3C, Taiwan) aligned with the humeral medial epicondyle, and a strain gauge load cell (Futek LCM200, USA) on the forearm. A servo controller (HIWIN N1, Taiwan) manages the rotary table, interfaced with a Beckhoff terminal (EK1100, Germany) controlled via EtherCAT.

Version 2, now used by Amsterdam UMC (Figure 3), enhances Version 1 (Rijndam) with increased rigidity, improved height adjustment, and safer enclosures. The rotary table (HiWin TMS3C) remains, now paired with an updated drive (HIWIN ED1, Taiwan) and more precise encoder. The displacement sensor has been removed, and a single force sensor (Futek LCM200) is connected to a Futek signal conditioner (IAA100). Beckhoff terminals now include 1x EL3102, 1x EL2002, and 1x EL2102. Control has shifted to TwinCAT 3 on Windows, running Simulink models at 1 kHz.

A full breakdown and comparison are provided in Section VIII-B, summarized in Table VI.

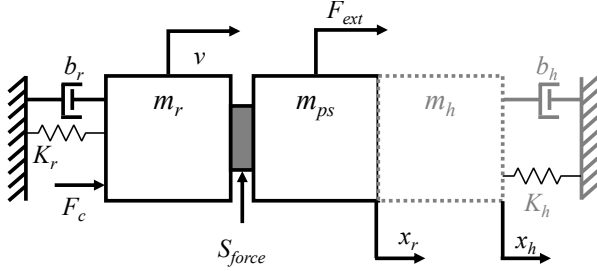
III. METHODS

A. Approach

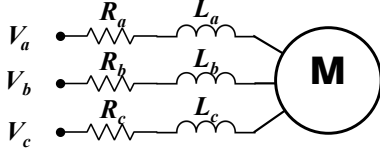
1) *System Modelling and Identification*: Modelling the SEP dynamics, shown in Figure 4, is crucial for effective control, particularly feedforward inertial compensation. Feedforward control predicts and counteracts inertia, improving system responsiveness and precision. Accurate dynamic models enable the design of controllers that anticipate motion, minimizing lag and enhancing performance in high-speed, high-accuracy tasks, as illustrated in Figure 4.

System identification offers a robust method for modelling complex mechanical systems with nonlinearities, such as mo-

tor cogging and compliance in 3D-printed parts and Sarrus linkages. Unlike traditional methods, it uses experimental data to derive models, capturing the relationship between inputs and outputs. Predefining system order improves parameter estimation and model fitting, reducing computational demands. Detailed system identification is described in Section VIII-E.



(a) A rigid robot experiences an external force F_{ext} and a control force F_c , acting on the combined inertia of the robot m_r and post-sensor inertia m_{ps} , resulting in velocity v . Energy losses are modelled as viscous damping b_r , and compliance is defined by K_r . The connection between m_r and m_{ps} is rigid via the load cell S_{force} for force measurement. The robot can also connect rigidly to a human, represented by inertia m_h , stiffness k_h , and damping b_h , as indicated by the grey dotted outline. The motion resulting from the force is defined by x_r after m_{ps} or x_h if the human arm is coupled.



(b) The voltage inputs V_a , V_b , and V_c pass through their respective resistances R_a , R_b , and R_c , as well as inductances L_a , L_b , and L_c , before entering the M block. The M block represents the internal dynamics of the motor, which is modelled as a PMSM or a three-phase servo motor, such as the Hiwin TMS3C.

Fig. 4: Mathematical modelling of the system

2) *Force Sensing*: The accuracy and responsiveness of the force sensor are crucial for effective admittance control. Piezoelectric sensors offer high sensitivity and frequency response, making them ideal for capturing dynamic force changes. However, strain gauge sensors, while typically having lower frequency bandwidth, provide robust and stable measurements over a wide range of forces. The choice between these depends on the specific application requirements, with strain gauges being more suitable for steady-state measurements and piezoelectric sensors excelling in dynamic scenarios.

3) *Servo Tuning*: Tuning a controller optimizes its response to feedback by adjusting gains for each loop (position, velocity, and torque), determining its reaction to errors. As highlighted by Keemink et al., 2018, low k_p and k_i values in the velocity controller meet passivity conditions, but high bandwidth control improves environment z-width by shifting phase lag to higher frequencies, affecting only higher human stiffness values. Increasing k_p and k_i can thus enhance environment z-width and improve disturbance rejection at the motor side, suppressing unwanted friction and parasitic dynamics despite not meeting passivity requirements. [24]

To implement negative inertia effectively, tuning the controller for higher velocity loop gains is crucial. The tuning

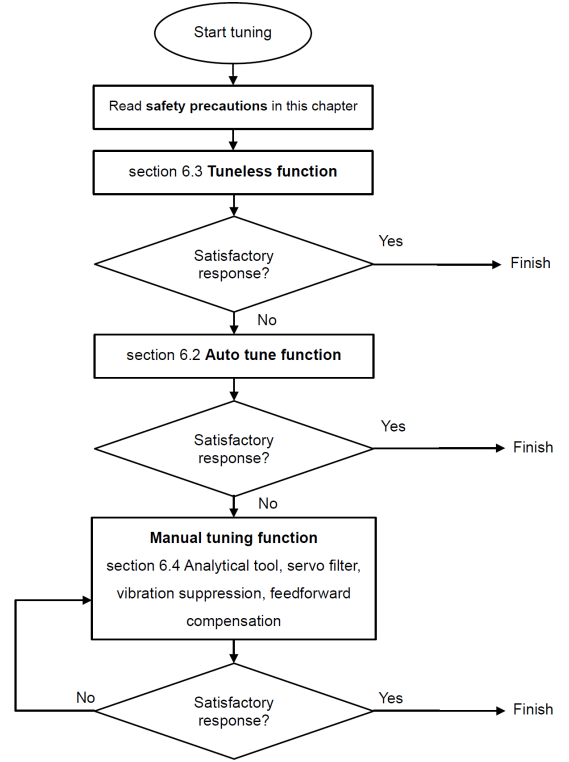


Fig. 5: The standard servo tuning and optimisation flowchart. [32]

procedure, illustrated in Figure 5, aims to find gains that balance high performance with stability. Excessive loop gains can cause instability, so multiple servo gain parameters can be adjusted for optimal response, including position loop gain, velocity loop gain, vibration suppression, feed-forward compensation, and filtering. Ideally, the PI controller for the velocity loop and the PD controller for the position loop are set to achieve the desired performance without additional delays from filters or extra gains.

- **Tuneless Function**: Automatically adjusts parameters based on system dynamics without manual intervention.
- **Autotune**: Uses a set of predefined motions to determine optimal tuning parameters.
- **Inertia Ratio**: Balances the motor inertia and load inertia to ensure stable and responsive motion.
- **Loop Gains**: Adjusts the proportional, integral, and derivative gains to refine control response and minimize errors.

These methods ensure the servo drive operates effectively, providing precise and responsive control.

4) *Additional Modalities and Filtering*: Adding an accelerometer to the system provides direct acceleration measurements, enhancing dynamic response calculations by sampling at 1000 Hz, compared to the 500 Hz derived from force data. This dual-source approach can improve accuracy and noise rejection, enabling better differentiation between noise and actual dynamic responses. The resulting precise acceleration data allows the controller to compensate more effectively for external disturbances and unmodeled dynamics,

leading to a more robust system.

Implementing negative inertia on the SEP can destabilize the system by reducing effective mass, but accurate acceleration disturbance observers can mitigate these dynamics, preventing instability and oscillations. Additionally, acceleration data can support real-time adjustments of damping coefficients, enhancing stability as noted by Keemink et al., 2018[24].

The Kalman filter, an optimal recursive algorithm, estimates a dynamic system's state from noisy measurements. Operating in prediction and update phases, it forecasts the next state using the system model and corrects predictions with new measurements. By integrating a noisy accelerometer, the Kalman filter effectively combines prediction with actual acceleration data, improving noise rejection and enhancing the accuracy and robustness of the system's dynamic response.

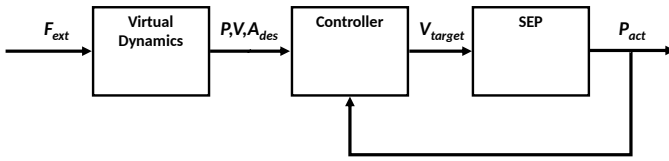


Fig. 6: The admittance control diagram for the SEP depicts the interaction between the robot dynamics, external forces, virtual dynamics, and the control system. The diagram illustrates the measured externally applied force F_{ext} , which passes through virtual dynamics to generate a reference position, velocity and acceleration P, V, A_{des} . A controller C attempts to enforce this velocity reference by generating a target velocity V_{target} , which is applied to the SEP through the Hiwin rotary table and servo drive (not shown). The resulting position of the robot is denoted as P_{act} .

5) *Admittance Controller*: Implementing an admittance controller for the Shoulder Elbow Perturbator (SEP) is shown in Figure 6. It involves modifying the robot's motion response to applied forces, giving the effect of reduced or negative inertia. This is achieved by adjusting the motion response rather than the force response, requiring precise force sensors but not extremely high bandwidths. The desired trajectory changes are processed with reduced computational loads, focusing on motion responses to force inputs.

6) *Negative inertia*: Incorporated using a force gain and a compensation force derived from the Kalman-filtered acceleration data. The compensation mass is calculated to counteract the inherent device inertia, while motor torque feedback is used to stabilize the system. By adjusting the force gain, the system can effectively reduce perceived inertia, improving responsiveness and control precision. The motor torque feedback loop ensures stability, preventing oscillations and undesired behaviours, thereby enhancing the overall performance of the SEP.

B. Experiment Design

1) *System Modelling*: The simplified dynamics of the SEP can be modelled mechanically as a mass-spring-damper system. Simplifying the mass of the robot and mass post sensor, from Figure 4a as a single mass due to rigid connection via

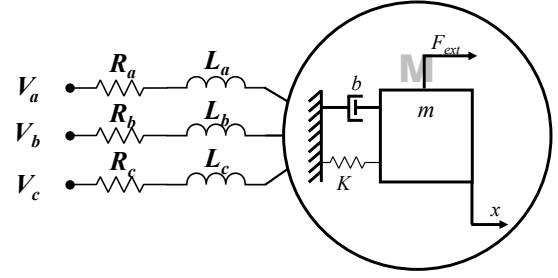


Fig. 7: The combined system dynamics, the simplified robot as a mass-spring-damper system with the electrical components in dq phase

force sensor. This turns it into a simple mass spring damper system, shown in Figure 7. In this model, the robot's joint or end-effector is represented by a mass m , connected to a spring with stiffness k and a damper with damping coefficient b . The equation of motion for the mass-spring-damper system is given by:

$$X(s) = \frac{F(s)}{m.s^2 + bs + k} \quad (5)$$

When integrating the motor dynamics, the external force F is the torque produced by the motor. Using the electromagnetic torque equation of a PMSM and considering the motor's electrical dynamics, we have:

$$V_q(s) = R_s I_q(s) + L_q s I_q(s) + \omega L_d I_d(s) + \omega \lambda_f \quad (6)$$

By combining the mass-spring-damper system dynamics with the motor's electrical model in the Laplace domain, we can fully describe the behaviour of the 1DOF robot. The overall system dynamics in the Laplace domain are given by:

$$X(s) = \frac{\frac{3}{2} P [\lambda_f I_q(s) + (L_d - L_q) I_d(s) I_q(s)]}{m.s^2 + bs + k} \quad (7)$$

where the current dynamics $I_d(s)$ and $I_q(s)$ are governed by the Laplace-transformed voltage equations. Getting the system frequency response with accurate estimated parameters. Detailed description is provided in Section VIII-D

For model estimation through system identification, the SEP is configured in Position Control Mode. It is then excited with carefully crafted multisine signals containing prime frequencies to prevent 2nd or 3rd harmonics. The inputs and outputs can then be processed for accurate model estimation using standard models in MATLAB. These models are Output Error(OE), Autoregressive with Exogenous inputs(ARX) and ARX with moving average filter(ARMAX).

2) *Force Sensing*: In the Rijndam SEP, two force sensors are available: the Futek LCM 200 strain gauge load cell and the Kistler 9237b piezoelectric transducer. The Kistler sensor, with superior sensitivity, accuracy, and rapid response time, is ideal for high-precision, dynamic measurements. In contrast, the LCM 200 offers high accuracy for static or slowly varying forces but with lower resolution. While the Kistler system excels in applications requiring a wide dynamic range and quick feedback, it is more complex and costly to integrate and is sensitive to environmental factors. The LCM 200 is robust

and cost-effective but vulnerable to electrical noise. For the SEP, the Kistler combo is optimal for dynamic performance and precision, whereas the Futek combo is suitable for static forces and ease of integration.

To validate these performance metrics, a series of experiments are conducted to evaluate the performance of these sensors based on the desired properties in Section VIII-F.

The following experiments are designed:

- *Initialising Sensors* - Connect the Kistler sensor to the terminals, coupler, and power supply to ensure force data recording functionality.
- *Calibration* - Calibrate the sensors using springs or masses of known weights to determine their accuracy.
- *Drift Comparison* - Preload the sensors for an extended period to assess drift characteristics.
- *Impulse and Oscillatory Response* - Conduct perturbation experiments using a pulley system to excite the robot with a perturbed mass or mass-spring setup. Analyze the Impulse Response Function (IRF) and Frequency Response Function (FRF) of the sensors.
- *Perturbation Signal Response* - Apply multiple sine waves to the robot in continuous synchronous position mode to determine which force sensor effectively tracks the disturbances.

Detailed descriptions of the experiments and desired sensor properties are laid out in Section VIII-F.

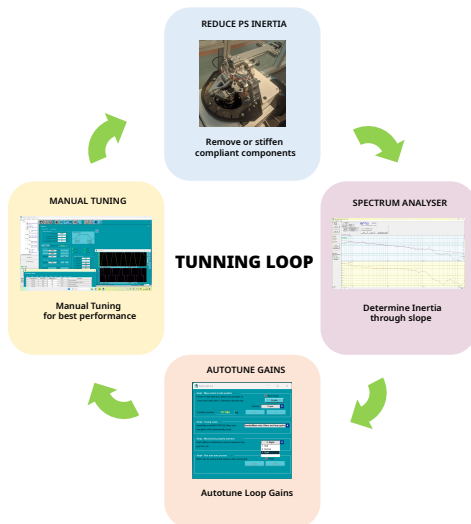


Fig. 8: The tuning loop for the SEP using Hiwin Thunder

3) *Velocity Controller*: The tuning procedure for the SEP in particular is illustrated in Figure 8 and Figure 9. Initially, the device inertia is reduced mechanically by tightening the Sarrus linkage, removing the various 3D printed enclosures, then using the spectrum analyser, a chirp perturbs the SEP and the frequency response is recorded. By placing a negative 2 slope on the plot, the inherent inertia is found. After this, the other loop gains are manually adjusted. Then the settling time is observed by executing a point-to-point movement of 90° at 180°/s with the acceleration and deceleration times set to 8ms. Subsequently, the device is autotuned, and the performance

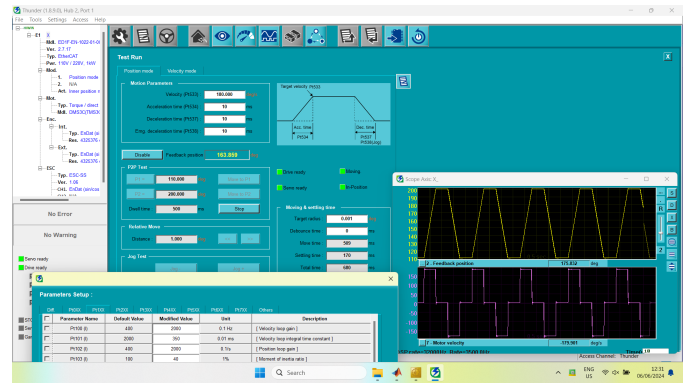
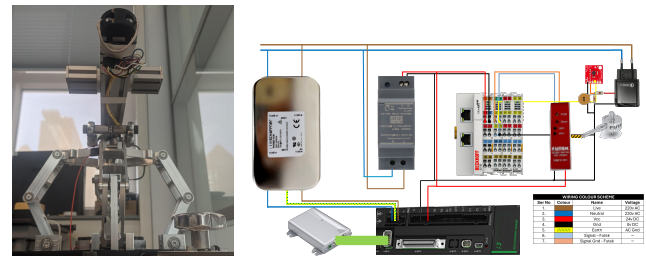


Fig. 9: The methodology of iterative tuning using the Hiwin Thunder. [33]

is compared again, the loop gains are readjusted to increase performance.



(a) The Accelerometer

(b) The wiring scheme

Fig. 10: Incorporation of the accelerometer in the SEP

4) *Accelerometer and Filtering*: For acquiring the acceleration data, an accelerometer is integrated into the distal end of the SEP's arm shown in Figure 10. A complete description of sensor choice and integration into the SEP is provided in Section VIII-G.

A Kalman filter is designed to minimally filter the raw data providing a smoother acceleration prediction, shown in Figure 11.

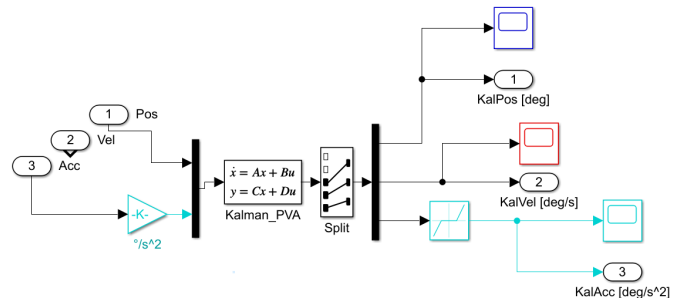


Fig. 11: The final Kalman implementation after tuning

The Kalman filter optimally estimates the state variables, position and acceleration, using measurements from a servo encoder and an accelerometer. The state-space model is defined by the state matrix A , the output matrix C , and the process noise influence matrix G :

$$\mathbf{A} = \begin{bmatrix} 0 & 1 & 0 \\ 0 & 0 & 1 \\ 0 & 0 & 0 \end{bmatrix}, \quad \mathbf{C} = \begin{bmatrix} 1 & 0 & 0 \\ 0 & 0 & 1 \end{bmatrix}, \quad \mathbf{G} = \begin{bmatrix} 1 & 0 & 0 \\ 0 & 1 & 0 \\ 0 & 0 & 1 \end{bmatrix}$$

The Kalman filter is designed by incorporating both process noise and measurement noise into the state-space model. These are fine-tuned using experiments described in Section VIII-G. The process noise covariance matrix \mathbf{Q}_N is tuned empirically:

$$\mathbf{Q}_N = \begin{bmatrix} q_1 & 0 & 0 \\ 0 & q_2 & 0 \\ 0 & 0 & q_3 \end{bmatrix}$$

Measurement noise is characterized by the encoder position noise and accelerometer noise, leading to the measurement noise covariance matrix \mathbf{R}_N :

$$\mathbf{R}_N = \begin{bmatrix} r_p & 0 \\ 0 & r_a \end{bmatrix}$$

The Kalman estimator \mathbf{K}_{est} is then calculated using the system dynamics and noise characteristics, yielding an optimal estimate of the state vector by minimizing the estimation error. This approach effectively combines the encoder and accelerometer data, considering the uncertainties in both the system model and the sensor measurements, to produce a reliable state estimation for the control system.

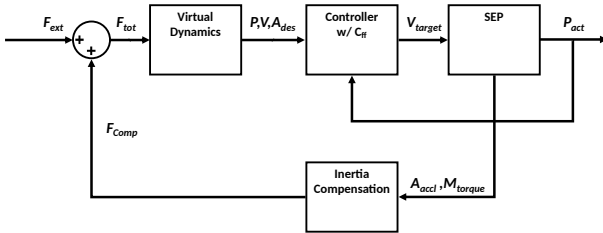


Fig. 12: The acceleration and motor torques are used as inputs to the compensation block which outputs a compensatory force F_{comp} , this is added to input force to make F_{tot} this passes through virtual dynamics to generate a reference position, velocity and acceleration P, V, A_{des} . A controller C with a feedforward element attempts to enforce this velocity reference by generating a target velocity V_{target} , which is applied to the SEP through the Hiwin rotary table and servo drive (not shown). The resulting position of the robot is denoted as P_{act} .

5) *Inertia Compensation*: Based on the guidelines from Table I for minimising inertia in admittance controllers while avoiding instability—especially during coupled movements. The following strategies will be tested and implemented.

- Reduce the physical inertia of the robot by using lightweight materials and minimizing the moving mass.
- Employ force sensors with high bandwidth and sensitivity to capture rapid changes accurately.

- Implement control algorithms that adjust parameters dynamically to maintain stability and desired performance.
- Carefully tune the feedback loop to balance responsiveness and stability, avoiding aggressive gains that may lead to instability.

An additional inertial compensation block is added to the admittance framework in Figure 12. The importance of achieving a balance between approaching intended virtual dynamics and ensuring robust stability through passivity is crucial.

IV. RESULTS

A. System Modelling

The parameters for the mathematical model are estimated based on device specifications and approximations for motor EMF and impedance. The rotary table's inertia is sourced from its manual [34], while the torsional stiffness, set at 50,000 Nm/θ , is estimated based on the servo motor's attributes. Damping is calculated using $B = 2\zeta\sqrt{MK}$ with a damping ratio (ζ) of 0.7, resulting in 58.56 Ns/m . Stator resistance, inductance, and pole pairs are derived from the manual, with flux leakage and angular velocity estimated from nominal values. The complete breakdown of the parameters is provided in Section VIII-E.

In the system identification approach, multisine signals with prime frequencies are used to analyze the joint system's dynamic response. These signals cover ranges of 0-11 Hz, 0-23 Hz, and 0-100 Hz, with amplitudes of 3° , 1° , and 0.1° , respectively. Prime frequencies ensure distinct frequency components, preventing harmonic overlap and facilitating accurate system identification. Higher amplitudes improved the signal-to-noise ratio (SNR), enhancing measurement precision.

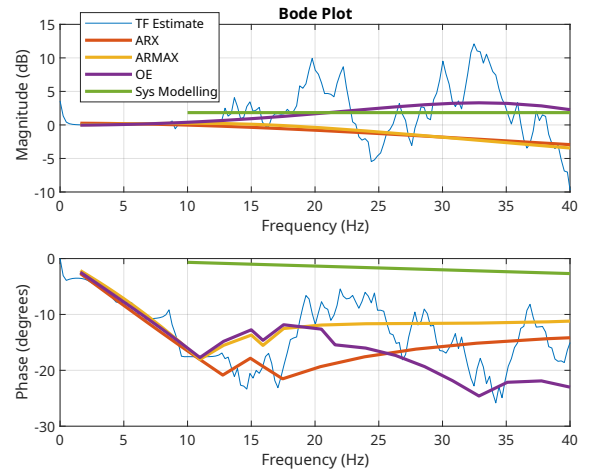


Fig. 13: In the relevant frequencies, the Output Error (OE) model is comparable to the estimated transfer function, the system model is incoherent with ground truth.

The system identification models are validated against the frequency response of the estimated system. Figure 13 shows the relevant frequency responses, revealing the magnitude plot of the mathematical model (in green) closely matches the OE model and aligns with the average estimated system

response. The phase plots for the OE, ARX (Auto Regressive Exogenous), and ARMAX (ARX with Moving Average Filter) models coincide with the estimated system's phase plot up to 11 Hz, the highest frequency excited during the experiment. From 15 to 35 Hz, the OE model's phase plot generally aligns with the estimated system response. Notably, none of the models drops below -180° without unwrapping, although the mathematical model shows instability. Therefore, the OE model is selected for feedforward compensation.

B. Force Sensing

From the experiments and results described in Section VIII-F, several key observations can be made from the four experiments: drift, impulse response, oscillatory response, and perturbation tests for bandwidth.

- *Drift Experiment:* Initial sensor loading shows slight variation before settling, indicating a longer warm-up phase for sensors or signal conditioners/amplifiers is crucial for reliable patient tests. The Kistler sensor exhibits more periodic noise spikes after load removal, suggesting increased noise sensitivity. The Kistler sensor also shows significant drift (54.85 N) compared to the Futek sensor (6.25 N). After load removal, the Futek sensor returned to $0\text{ N} \pm 0.4$, while the Kistler settled at $48.55\text{ N} \pm 5$.
- *Impulse Response:* Excited frequencies ranged from 0 to 80 Hz, suitable for system response analysis. Both sensors showed nearly identical force profiles, indicating good calibration. However, the Kistler sensor exhibits periodic noise, potentially problematic for an admittance controller, especially around 100 Hz.
- *Oscillation Experiment:* Excited frequencies are in the lower ranges, relevant for human interaction, as humans respond to frequencies below 20 Hz. Both sensors track forces similarly, but the Kistler sensor has more prominent noise around 100 Hz. Variations in load extremities (-90 N vs. -88 N) were observed. High oscillation attenuation indicates high system damping, possibly due to compliance or loose straps.
- *Perturbation Experiment:* The Kistler sensor shows significant electromagnetic interference (EMI) when the servo drive is active, rendering low-frequency response unusable compared to the Futek sensor. The high-frequency response improves but periodic noise persists.

C. Velocity Controller

Inertia is measured from the system's frequency response by applying a negative 2 slope to the curve, from Figure 14. The measured inertia, ranging from 0.040 to 0.053 kgm^2 , is slightly higher than the TMS3C motor's inertia of 0.035 kgm^2 . This range of inertia values results from removing post-sensor masses, such as wrist clamps, bolts, and the 3D-printed enclosure.

By doubling the velocity and position loop gains and halving the integral time constant, following the tuneless approach. Performance is evaluated by executing a point-to-point movement of 90° at $180^\circ/\text{s}$, with acceleration and deceleration times set to 8 ms. The initial settling time was

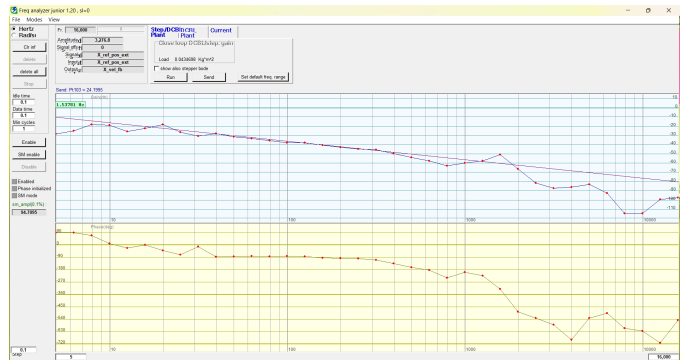


Fig. 14: The Spectrum Analyser used to plot the frequency response of the servo motor.

400 ms. Through iterative tuning, as shown in Figure 9, the settling time is reduced to 100 ms, this is deemed sufficient for implementing the admittance controller.

D. Accelerometer and Filtering

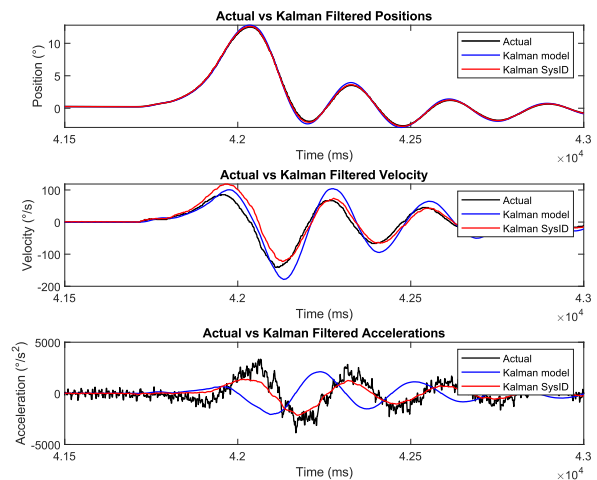


Fig. 15: Kalman filtered versus actual data for position encoder, velocity from Hiwin servo drive and acceleration from accelerometer

From Figure 15, the system identification-based model outperforms the simple model in accuracy, yielding lower RMSE values for position, velocity, and acceleration estimates. It offers slightly improved response times due to its precise representation of system dynamics. Although both models demonstrated stability, the system identification-based model exhibited less variability in estimates, indicating superior noise handling. However, in real-world SEP operations, the simple model provides smoother performance, enhancing human-robot interaction, while the accelerometer's lag limits performance.

Implementing the Kalman filter with the system identification-based state-space model produces more accurate and reliable state estimates than the simple theoretical model. The identified model's ability to capture

true system dynamics made it the preferred choice for final implementation. However, the Kalman filter fails to run on existing SEP hardware, likely due to the absence of a real-time computer. Consequently, the Kalman filter is reverted to the initial design, resulting in smoother SEP movements but with out-of-phase acceleration.

E. The Admittance Controller

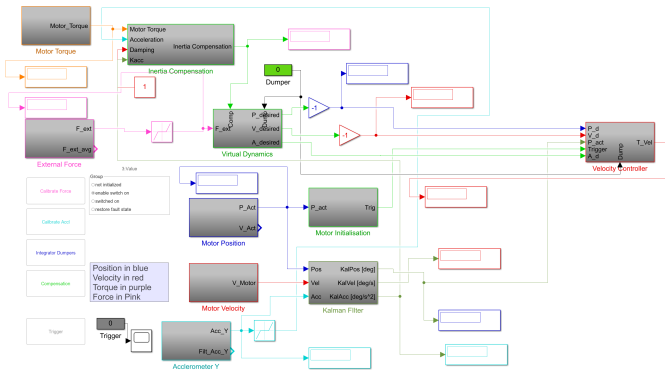


Fig. 16: The initial admittance controller framework in Simulink with external force block as an input, virtual dynamics creating the desired reference, velocity controller enforcing it and rest of the modules augmenting the operation

The admittance controller on the SEP is implemented as illustrated in Figure 16. The SEP was configured in Cyclic Synchronous Velocity mode and a Simulink model for the velocity controller with drift compensation was created to ensure a good position and velocity control loop.

- **Motor Initialization:** from Figure 17, configures the servo drive to cyclic synchronous velocity mode and enables virtual safety to stop the drive before reaching physical end stops. It also activates the Hiwin ED1 drive and starts the motor.

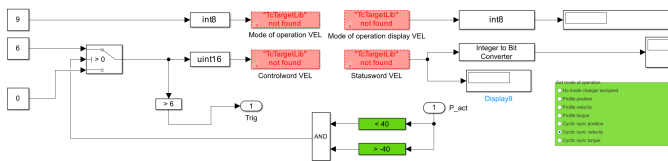


Fig. 17: Motor Initialization

- **External Force:** from Figure 18 converts force sensor readings to Newtons and applies a moving average filter to calibrate the sensor with a zero offset.
- **Virtual Dynamics:** from Figure 19 computes desired acceleration, position, and velocity using:

$$\ddot{x}_{\text{desired}} = \frac{F - B\dot{x} - Kx}{M}$$

These are sent to the velocity controller.

- **Velocity Controller:** from Figure 20, generates target velocity using desired position, motor encoder position error, and drift compensation PI gains. It acts as a position control loop by adjusting velocity based on the end

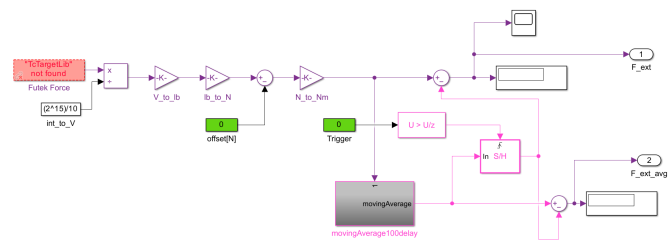


Fig. 18: External Force

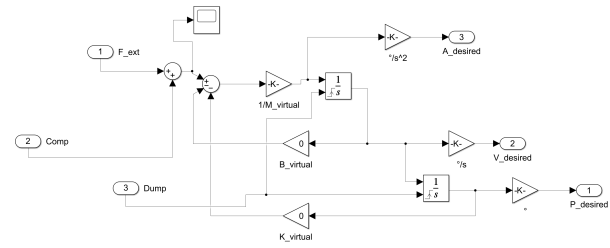


Fig. 19: Virtual Dynamics

effector position. A velocity damper resets integrators to maintain safe operation.

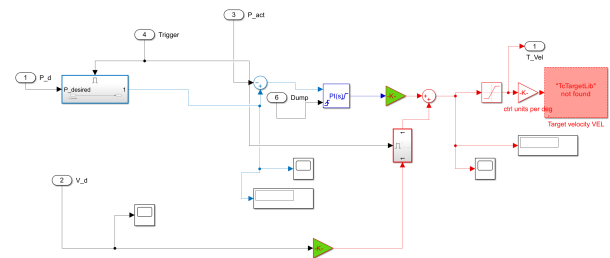


Fig. 20: Velocity Controller

- **Accelerometer Y:** provides raw and filtered acceleration data. The moving average filter introduces a 100 ms delay but aids in observing system behaviour in real time.
- **Motor Velocity and Position:** Acquires absolute motor encoder position and velocity for input to the velocity controller and the Kalman filter, which, along with accelerometer data, facilitates inertial compensation.
- **Motor Torque:** Used to set torque limits, for the torque controller and inertial compensation.

Full page images of the controllers can be found in subsection VIII-J.

F. Combining Feedforward and Feedback Control

Combining feedforward (FF) and feedback (FB) compensation strategies can enhance the SEP's performance. Feedforward control effectively neutralizes inherent system dynamics, while feedback control provides stability and error correction.

1) *Model-Based Feedforward:* The feedforward strategy employs a second-order mass-spring-damper model fitted to the system's response, using parameters such as the undamped natural frequency ω_0 , damping ratio ζ_f , and compliance C_f . The generalized transfer function of the SEP is given by:

$$G(s) = \frac{C_f \omega_0^2}{s^2 + 2\zeta_f \omega_0 s + \omega_0^2} \quad [m/N] \quad (8)$$

The feedforward controller compensates for undesired dynamics by inverting the plant's transfer function without altering static position loop gains:

$$C_{ff}(s) = \frac{s^2 + 2\zeta_f \omega_0 s + \omega_0^2}{\omega_0^2} \quad (9)$$

To ensure a realizable controller, additional poles are introduced to achieve a well-damped system:

$$C_{ff}(s) = \frac{s^2 + 2\zeta_f \omega_0 s + \omega_0^2}{s^2 + 2.1\omega_0 s + \omega_0^2} \quad (10)$$

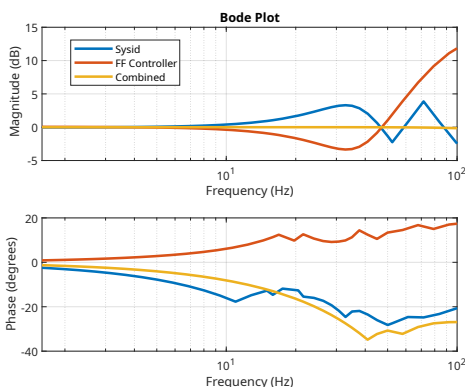


Fig. 21: The combined system response shows minimal inertia dynamics at higher frequencies

Implementing the controller as a notch filter can attenuate high-frequency resonances [35]. In theory, the controller cancels resonance and anti-resonance, resulting in a well-damped system in Figure 21. However, due to hardware limitations, the implementation of the SEP velocity controller (Figure 22) did not perform as expected. A real-time computer could resolve these issues.

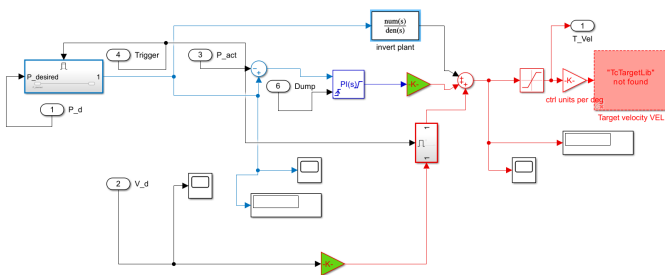


Fig. 22: The inverted plant with a second-order lowpass filter combined with feedback controller to improve system dynamics

2) *Adaptive Control*: External factors can alter a system's dynamic properties, causing deviations between model parameters and reality. Adaptive feedforward control adjusts the feedforward signal based on actual system behaviour, often used with feedback control. In the SEP, characterized by force

gain $G_f > 0$ and inertia and damping compensation $C_{ff} = \mu_{ff}s + \beta_{ff}$, this approach enhances anticipatory response and admittance tracking performance, reducing apparent inertia:

$$\mu_{ff} \geq \frac{K_p + b_m}{K_p + \beta_{ff}} m_m \quad (11)$$

The feedforward model includes inertia and damping terms for improved disturbance rejection. Feedback control refines dynamic behaviour by correcting errors between desired and actual states. Integral feedback gain K_i ensures accurate low-frequency dynamics, meeting the condition $\beta_{ff} k_r^2 \geq b_r$:

$$m_v \geq \frac{(K_p + \beta_{ff} k_r^2) m_r - (K_p + b_r) \mu_{ff} k_r^2}{(G_f k_r + 1)(K_p + b_r)} \quad (12)$$

$$0 \leq (\beta_{ff} k_r^2 - b_r) K_i \quad (13)$$

Precise feedforward control is essential when executing predefined motions with limited position error. Due to known force requirements, feedback control alone may not suffice. Figure 22 shows the use of a PI controller with clamping anti-windup. Integrators in feedforward control can cause delayed reactions to disturbances by accumulating past errors. Accurate feedforward control minimizes these delays, but SEP limitations prevent its use. Anti-windup techniques like clamping reduce integrator gain until the system returns to its linear range, ensuring stability and performance.

High-performance feedback control is crucial for following unknown target motions, stabilizing unstable systems, and mitigating disturbances. Ensuring robustness is vital due to the trade-off between stability and performance.

The combined feedforward and feedback strategies improve force control accuracy and energy efficiency, enhancing robustness against disturbances and model uncertainties. Integrating both strategies within an admittance framework significantly boosts the robot's operational effectiveness.

G. Negative Inertia

The negative inertia implementation includes an inertial compensation block within the overall control scheme, as shown in Figure 23. This block generates a compensatory force combining several elements: the force gain G_f from motor torque, adjusted by the SEP arm radius, and the Kalman-filtered angular acceleration converted to SI units from the accelerometer, multiplied by a compensatory mass. It also considers the inertia of the SEP, both pre and post-sensor, obtained from the spectrum analyzer in Figure 14, and multiplies this by the model's acceleration. A damping term is added to prevent instabilities.

A compensation trigger, shown in Figure 24, allows real-time toggling of the compensation for clear observation of its effects.

Reducing the rendered mass by decreasing virtual mass leads to vibrations and oscillations in the SEP. This instability propagates due to the noisy force input to the virtual dynamics. To address this, additional experiments determine the noise floor for both the force sensor and accelerometer. Figure 25 shows probability density functions (PDFs) obtained from

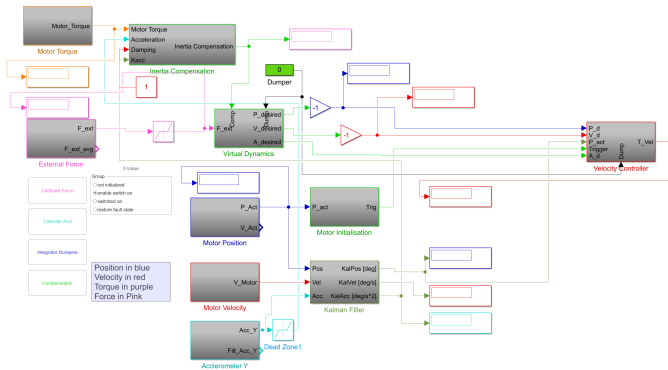


Fig. 23: Complete control scheme with inertia compensation block

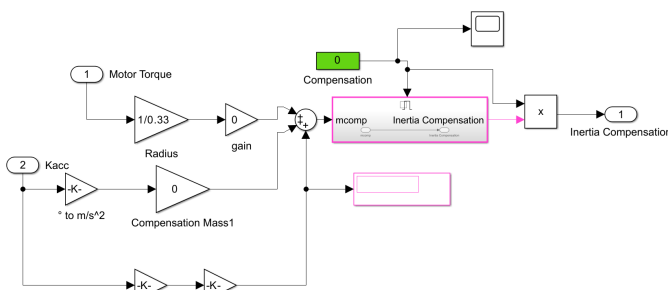
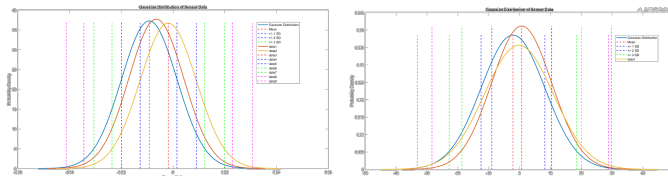


Fig. 24: Inertia compensation block

three-minute trials, establishing safe noise levels for deadband implementation. The deadband limits are set to the midpoint between the lower and upper extremities of the first standard deviation for each sensor. This implementation allows the virtual mass to be reduced down to 100 grams, previously unstable below 300 grams, without compromising sensitivity or performance. Full page images of the controllers can be found in subsection VIII-K.



(a) Probability density function for force sensor (b) Probability density function for accelerometer

Fig. 25: PDF analysis to determine safe noise levels for deadband implementation

For evaluating the mitigation strategies for inertia, a virtual dynamic model is set with the following parameters:

- Mass: $m = 0.30$ kg
- Damping: $b = 10$ Ns/m
- Stiffness: $k = 100$ N/m

The SEP arm is perturbed by pulling it $\pm 10^\circ$, followed by triggering to ensure the arm's properties do not influence the results. Trials were conducted over a 90-second window

to collect sufficient data for deriving Frequency Response Functions (FRFs).

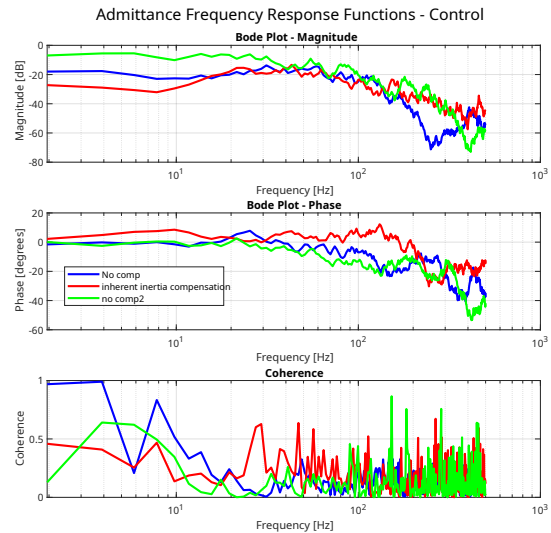


Fig. 26: Control group for the admittance FRF

As shown in Figure 26, the initial response resembles a standard mass-spring-damper system, with both red and green responses exhibiting typical inertial characteristics. The system demonstrates a stiffness slightly below 0 dB and a minor damping trough at the crossover frequency of 20 Hz, followed by a slope of -2, indicating normal inertia. However, due to insufficient high-frequency excitation, the coherence is low, limiting the ability to make definitive judgments. The phase plot reveals general lag at higher frequencies. Between the "no comp" (blue) and "no comp2" (green) responses, damping was reduced from 10 Ns/m to 3 Ns/m to allow for more oscillations.

Next, critical inertia compensation is evaluated by setting the accelerometer-based mass compensation to 0.30 kg, cancelling the virtual mass set in the virtual dynamics block. This base scenario is then augmented with inherent inertia compensation from the model, effectively removing the device's total inertia from the system. Motor torque-based disturbance rejection is included to ensure stability.

Figure 27 shows good coherence for the critical compensation (blue) and the critical compensation with inherent inertia compensation and disturbance rejection (green). The green plot, in particular, exhibits a flat response across all frequencies around 0 dB, as expected. The blue plot, showing only critical inertia compensation, reveals the presence of some stiffness in the system, reflected by the response at -5 dB. The phase plots for relevant frequencies (≤ 20 Hz) indicate slight phase lag at lower frequencies, remaining close to zero, with the green plot showing a slight phase lead, suggesting some negative inertia characteristics. This phase lead is attributed to the additional compensation for inherent inertia, and a slight reduction in this compensation would likely result in a response closer to 0 dB with a constant phase at 0° .

For negative inertia compensation, the accelerometer force

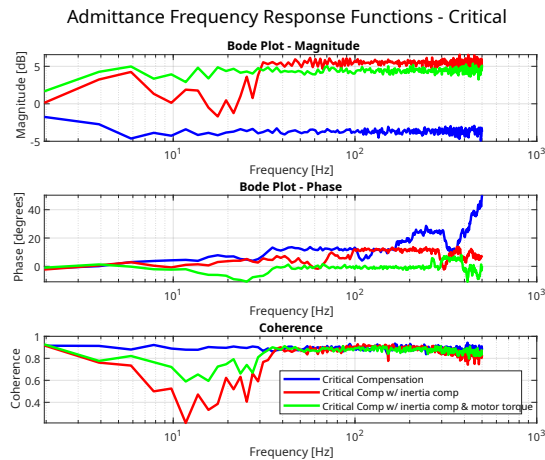


Fig. 27: Critical compensation strategies for the admittance FRF

compensation is increased to 0.50 kg, creating approximately 200 grams of negative inertia. This method of augmenting the inertia reduction is repeated to evaluate the performance differences.

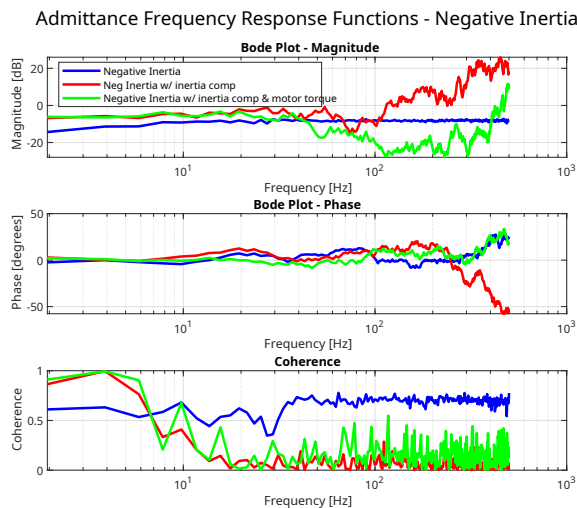


Fig. 28: Negative inertia strategies for the admittance FRF

Figure 28 reveals key trends. Initially, the green and red responses exhibit stiffness slightly below 0 dB, indicating some stiffness in the system. The blue plot, representing negative inertia compensation, starts around -15 dB, indicating higher stiffness at low frequencies. A slight damping peak at 6 Hz is observed for both green and red responses, followed by a -2 slope until 100 Hz, after which the slope becomes +2, indicating the presence of negative inertia. The red plot only slightly shows inertial characteristics, while the response becomes incoherent beyond this due to low coherence. The blue plot, however, maintains the highest coherence, starting with positive stiffness and a positive slope, moving from -15 dB to -10 dB. The presence of negative inertia is further

evidenced by the positive phase lead from 10 Hz to 80 Hz in the green and red plots, indicating its presence in the system.

Finally, Figure 29 compares no compensation, critical compensation, and negative inertia. While coherence at higher frequencies remains insufficient for conclusive results, however, the presence of negative inertia becomes more apparent when compared to control experiments and critical compensation.

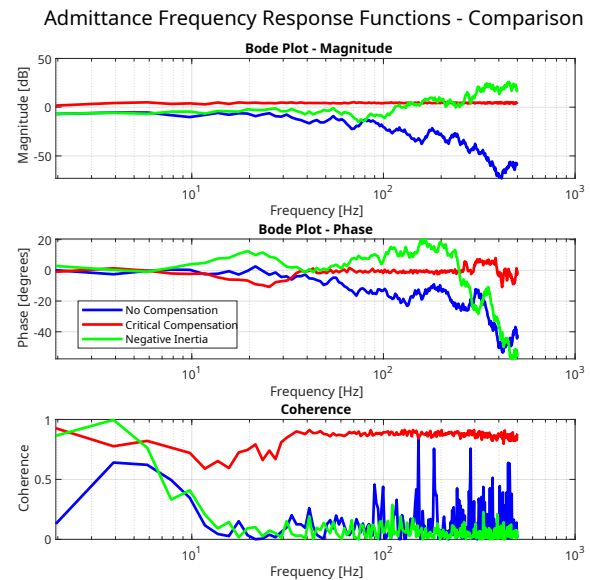


Fig. 29: Comparison of no compensation, critical compensation, and negative inertia for the admittance FRF

Improving coherence at higher frequencies will require higher-frequency excitation. Variations in responses within similar trials underscore the necessity for precise triggering to capture significant signals. By comparing coherent results, the differences between rendered virtual inertia, critical inertia (0 Kg), and negative inertia become clearer. The accelerance or dynamic mass FRF can be generated to assess the mass being negative to consolidate the presence of negative inertia.

V. DISCUSSION

A. Caveats

In this research, various strategies are explored, evaluated, and implemented on two Shoulder Elbow Perturbators: the Rijndam SEP and the Amsterdam SEP. The goal was to assess the effective implementation of negative inertia on these devices. These strategies provide valuable insights into the feasibility of achieving negative inertia. This section reviews the approaches presented in previous sections and evaluates their effectiveness in enhancing transparency and implementing negative inertia.

In Section III, initially proposed rendering negative inertia by integrating it into the virtual dynamics of the admittance controller. The goal was to achieve enhanced transparency and negative inertia by making the effective rendered mass approach zero or even negative. However, this approach fails when the rendered mass falls below 300 grams. At such low

masses, the force sensor's noise floor, amplified by $1/\text{Mass}$, causes large amplitude oscillatory reference signal at higher frequencies. These oscillations exceed the velocity controller's capability, resulting in phase lag, position deviations, and increased PI controller errors, ultimately creating a positive feedback loop that leads to instability. The SEP's end-effector frequently hits its virtual limits, preventing a stable interaction.

The strategy of using $M_{\text{effective}} = M_{\text{desired}} - M_{\text{virtual}}$ is ineffective and is therefore reverted to using only M_{virtual} for the rendered haptics. This adjustment enables the stable operation of the SEP with virtual rendered mass as low as 200 grams without unnecessary oscillations. The addition of dead zones in the force sensor noise floor suppressed undesired oscillations without the trade-off of filtering, thus avoiding added time delays. Reducing the rendered mass even lower.

B. System Modelling

System modelling and system identification are employed to accurately describe the plant, aiding multiple elements of the control system. Understanding system dynamics across low, crossover, and high frequencies is essential. The initial model, a simple mass-spring-damper system is inadequate, when compared to a system identification approach that better captures nonlinearities such as cogging, compliance in the Sarrus linkage, and post-sensor inertia, which are difficult to measure. The refined model served as a more accurate state approximation for later stages of controller design.

However, each approach has its limitations. The system identification method uses position-based multisine perturbations, requiring high signal-to-noise ratios and extensive frequency content for a comprehensive model. While theoretically feasible, physical constraints limit safe perturbation to 11 Hz, as higher frequencies risked physically compromising the SEP's structural integrity. Although not perfect, the system model adequately captures the system dynamics.

Alternatively, the Hiwin Thunder software's built-in spectrum analyzer proved more effective for determining the device's frequency response. Using a chirp signal from 0 to 2 kHz, it accurately assessed the total inertia, stiffness, and damping of the system.

C. Force Sensing

The literature review identified piezoelectric force sensors as the optimal choice for the SEP due to their high precision, reduced noise, greater sensitivity, and higher bandwidth. The Kistler piezoelectric force transducer was expected to outperform the Futek strain gauge sensor. However, during testing, the Kistler sensor exhibited periodic noise and was highly susceptible to electromagnetic interference (EMI) from the servo drive.

EMI is mitigated by using multiple grounding wire loops and shielded connections between the charge amplifier and Beckhoff terminals. A separate DC power supply for the servo drive also reduced interference. Despite these measures, periodic noise persisted at 5-6 Hz with harmonics around 100 Hz, as shown in Figure 53. Implementing a notch filter was considered but rejected due to the potential loss of critical

force information below 20 Hz, which is crucial for minimizing inertia as per the guidelines in Table I. The persistent noise suggests potential damage to the charge amplifier, likely due to mishandling. Testing confirmed the hypothesis by observing periodic noise even when the sensor is disconnected from the amplifier.

This interference compromised the Kistler sensor's true performance, rendering it unsuitable for the current setup. The communication rate of 1 kHz further limited the sensor's high bandwidth capabilities, equating its performance to that of the strain gauge sensor. This limitation underscores the need for improved shielding and communication protocols to fully utilize piezoelectric transducers in the SEP. The Futek sensor, coupled with the ICPDAS, samples at 600 Hz, while the Kistler is limited to 1 kHz due to EtherCAT communication constraints. Individual terminals can operate at a 10 kHz sampling rate but are constrained by the 1 kHz system limit. EtherCAT's synchronization protocols manage data effectively, balancing bandwidth to prevent data loss and latency.

This bottleneck is particularly evident in the Amsterdam SEP, where the Futek LCM200 strain gauge is paired with the Futek IAA 100 signal conditioner, capable of sampling rates from 1 kHz to 25 kHz, with a load cell eigenfrequency of 26 kHz. To enhance performance in the current SEP setup, rather than replacing or augmenting the force sensor with a piezoelectric variant, increasing the communication rate from 1 kHz to 4 kHz is a more efficient and cost-effective approach. Aligning the system with the ACT4D manipulator will enhance the performance of the SEP's sensing elements and improve the motion controllers. Increasing the bandwidth of the position loop will, in turn, enhance the velocity and torque loops as well.

D. Velocity Controller

1) *Drive Tuning:* Servo drive tuning is crucial for balancing performance and robustness in the SEP. The process begins with estimating the device's inertia using a Bode plot from the spectrum analyzer. The SEP has an additional inertia of 0.00888 kgm^2 compared to the rotary table's 0.035 kgm^2 , affecting the inertia ratio. Initially, the tuneless function provides a baseline by automatically adjusting parameters to match system inertia. It sets loop gains for a rigid response, suitable for the SEP's direct drive system.

However, the tuneless function alone is insufficient, prompting the use of the autotune function to refine performance. Autotune systematically adjusts position, velocity, and integral gains to optimize performance, increasing loop gains and inertia ratio by approximately 50% while reducing the time integral by 50%. This improved performance but also introduced excessive stiffness and subsequent jittering.

Additional manual tuning focused on the position loop gain, which is critical for accurate positioning. A slightly reduced position loop gain was chosen to avoid overshoot and instability. Although less relevant for the current velocity control mode, this adjustment is useful for system identification experiments requiring position control.

The velocity loop gain is increased to enhance system responsiveness. While higher velocity gain improves tracking

accuracy, exceeding a critical threshold led to diminished returns, making the drive overly stiff and causing high-frequency oscillations. The velocity loop gain is therefore iteratively adjusted from 400 to 1150, balancing responsiveness and stability without significantly increasing oscillations.

Integral gain tuning eliminated steady-state error, ensuring precise control over time. Achieving the right balance in velocity loop gain is essential for optimal performance, as excessive gains lead to overcorrection and instability.

Controller acceleration and deceleration times were constrained to 8 ms to maintain stability, forming a trapezoidal profile rather than the ideal square wave.

2) *Additional Modalities:* Adding an accelerometer at the SEP's distal end provided extra-sensory data but introduced noise. This was addressed by implementing a noise-dead zone and a Kalman filter.

Two Kalman filter designs were considered: a relation-based approach (position, velocity, acceleration) and a model-based approach from the identified system. The model-based filter, once tuned, offered less lag and better velocity and acceleration response. Although less smooth than the relation-based filter, it provided a robust response with minimal lag. However, it failed to run on existing hardware, producing an out-of-scope error, leading to reverting to the relation-based filter.

Additionally, the accelerometer's measurement range is limited to $\pm 3g$, and only the Y-axis was measured at 1.5 kHz, while Beckhoff hardware operates at 1 kHz, causing aliasing and noise. Increasing the system bandwidth to 4 kHz could mitigate these issues.

E. Inertia Compensation

The implementation of negative inertia in the Shoulder Elbow Perturbator (SEP) demonstrates a successful application of various control strategies, although evaluating performance metrics poses significant challenges. Through system modelling, system identification, and controller tuning, the SEP achieves negative inertia, enhancing transparency and responsiveness. However, accurately quantifying these improvements remains difficult due to the complexity of dynamic interactions and limitations in current measurement techniques. An alternate result analysis using dynamic stiffness is presented in Section VIII-I.

The research employs a variety of approaches to render negative inertia effectively. These included integrating negative inertia into the virtual dynamics of the admittance controller and employing multiple sensor modalities. Each approach showed promise in enhancing the SEP's performance, particularly in reducing the perceived inertia and improving human-machine interaction.

Various strategies are explored, and experiments are designed and validated to observe the implementation of negative inertia on the Shoulder Elbow Perturbator.

1) *Feed Forward Control:* Inertia minimization strategies in the Shoulder-Elbow Perturbator (SEP) have shown promising potential for enhancing its performance in physical human-robot interaction (pHRI). By applying feed-forward control,

we effectively reduce the SEP's apparent inertia, allowing for more responsive and accurate force application during perturbations. This approach, akin to anticipating external forces, has proven particularly beneficial in ensuring that the SEP responds swiftly to user inputs, thereby improving overall system stability.

"Increasing magnitude of the transfer function controller at higher frequencies with a +2 slope in the Bode plot. Such a behaviour is physically impossible so the controller needs to be modified in such a way that it becomes realisable." [35].

This is why the feed-forward control is based on a force gain and a compensatory mass, as the inverted plant for feedforward did not work as intended on the velocity controller. This requires the robot to be in torque control mode with the desired torques calculated from either the virtual dynamics (position, velocity and acceleration given as input) or by obtaining the torques from the force through the Jacobian. The limitation with this strategy is the bandwidth of the controller as a general rule of thumb for the operating bandwidth of the torque controller is roughly 16 times higher than the position loop which, given the SEP runs at 1 kHz would be only 62.5 Hz (in position loop), making it a very lethargic controller. This is elaborated in Section VIII-H.

2) *No Force Filtering:* To ensure minimal filtering, no filters are applied to the force input however this leads to the problem of controller instability when the rendered mass of the virtual dynamics approaches the actual inertia of the system. This causes two main issues.

- The noise floor of the force sensor causes an oscillatory desired position as the input to the velocity controller. These oscillations are in the region of 100 Hz which is higher than the current velocity controller limit.
- These high-frequency oscillatory targets cannot be sufficiently tracked by the velocity controller and therefore the controller overshoots becoming unstable.

To get around this issue, a dead zone is introduced to effectively remove this noise floor, the dead zone is tuned to ensure only the bare minimum noise floor is removed while enabling the sensing of the pHRI.

3) *Minimising Post Sensor Inertia:* The inertia of the rotary table is 0.035 kgm^2 , and the added inertia from the end effector, linkages and clamps increase it to nearly 0.053 kgm^2 , in line with the ACT4D and the Rijndam SEP. However removing the wrist clamps, the 3D printed enclosure decreases the inertia to 0.04388 kgm^2 .

This assisted in reducing the inherent inertia of the SEP allowing better negative inertia feel.

4) *Using Virtual Damping:* By incorporating a small amount of damping into the system, The SEP can smooth out rapid changes in force, reducing the likelihood of oscillations or instability. This approach can be particularly effective in tasks requiring precise control, such as fine motor adjustments during rehabilitation exercises. Avoiding excessive overshoots. This is a fixed term in the current controller but it can be made variable through a sliding model strategy.

5) *High Loop Gains:* Higher velocity loop gain in the controller results in increased stiffness, leading to small vibrations and a rough, more rigid pHRI experience. Conversely,

insufficient gain compromises trajectory tracking, which is undesirable. Therefore, precise tuning of the loop gain is essential to achieve an optimal balance. The introduction of clamping anti-windup significantly enhances performance, enabling a smoother velocity controller while permitting higher loop gains.

6) *Optimising Robot Stiffness*: The SEP's hardware is observed to have some unwanted compliances in the Sarrus Linkage Mechanism which reduces the effective stiffness of the device. This compromises the controller's performance. Improving the hardware is not part of the scope of this research however, some crude modifications are made to reduce this compliance as much as possible. As mentioned earlier, the additional post-sensor components are removed along with components like the enclosure to remove unwanted flexing. Additional shims are added to the Sarrus linkage mechanism to remove slop. Finally, the linkage mechanism is compressed and fixed via zip ties to reduce the leverage from the connections where the slop originates.

All in all, this reduces the compliance in the mechanism, making the SEP more responsive but for human trials, an extensive redesign of the system is required.

The successful implementation of negative inertia in the SEP highlights the potential for incorporating more advanced control strategies to enhance its capabilities. Despite the challenges in evaluation, the approaches used in this research demonstrate major improvements in system transparency and responsiveness. Future work should focus on refining evaluation metrics and exploring further sensor integration to optimize the SEP's performance.

In conclusion, the integration of these inertia minimization strategies in the SEP has the potential to substantially improve its performance in pHRI. By carefully balancing responsiveness, stability, and accuracy, a robust controller framework for the SEP is developed, capable of meeting the complex demands of shoulder-elbow diagnostics and rehabilitation. Future work can focus on further refining these strategies, particularly in optimizing the trade-offs between noise reduction and system responsiveness, to enhance the SEP's capabilities in real-world applications.

VI. FUTURE WORK AND LIMITATIONS

The research presented here demonstrates progress in understanding the performance of force sensors and system dynamics for incorporating negative inertia within the SEP's admittance controller framework. However, several limitations exist. Notably, there are no established standards for measuring the SEP's negative inertia within an admittance control framework. This lack of standardization complicates the evaluation of controller performance and comparison across different systems.

Additionally, while the experiments utilized the servo drive for the position control loop through velocity control mode, higher bandwidth velocity and/or torque controllers could potentially be more beneficial if tuned using Simulink. The servo drive operates at up to 3.2 kHz, which is significantly higher than the 1 kHz limitation of the Beckhoff hardware. This

discrepancy suggests that using a real-time computer could enhance feedforward compensation in torque control mode using torques from force Jacobian. By leveraging an inverted plant model, the system's inertia can be further minimised, enhancing control precision and responsiveness.

Implementing a cascaded controller scheme could also improve the system's response. This approach would allow for a more responsive controller by addressing different dynamic aspects of the system at multiple levels (torque loop gains, velocity loop gains). Furthermore, introducing sliding mode control for damping could provide adaptive damping, particularly when negative inertia is active. This adaptive damping would contribute to more stable negative inertia rendering in physical human-robot interaction (pHRI).

Future work should focus on addressing these limitations by developing standardized methods for measuring negative inertia in admittance control frameworks. Additionally, redesigning the SEP's Sarrus linkage for less compliance would ensure a more robust control design. Integrating real-time computing capabilities and exploring advanced control strategies such as cascaded controllers and sliding mode control could enhance system performance and stability.

VII. CONCLUSION

This research successfully explores and demonstrates methodologies for reducing inertia and implementing negative inertia in robots designed for upper extremity diagnostics and rehabilitation. By incorporating accelerometers and Kalman filters into the control scheme, we achieved smoother and more responsive physical human-robot interactions. The application of force gain to simulate negative inertia further enhanced the robot's responsiveness within the admittance control framework.

The introduction of dead zones for force and acceleration proved crucial in ensuring stable responses at lower rendered inertia, particularly in the presence of spastic conditions. Our experiments highlighted some improvements in system performance and stability, confirming the potential of advanced control strategies to optimize robotic rehabilitation.

However, this research also revealed certain limitations. The absence of standardized methodologies for measuring negative inertia remains a challenge, complicating the evaluation of system performance. Additionally, hardware constraints, particularly the discrepancy in bandwidth between the servo drive and Beckhoff hardware, limit the maximum achievable performance.

Future work should focus on developing standardized evaluation methods and optimizing hardware to minimize compliance and enhance control precision. Further exploration of advanced control strategies, such as cascaded controllers and sliding mode control, could provide additional improvements in system performance and stability.

Overall, this research demonstrates the feasibility and benefits of implementing negative inertia in robotic systems for upper extremity diagnostics and rehabilitation, paving the way for more effective and responsive therapeutic interventions.

REFERENCES

- [1] M Patrice Lindsay et al. *World Stroke Organization (WSO): global stroke fact sheet 2019*. 2019.
- [2] URL: <https://www.vzinfo.nl/beroerte/sterfte>.
- [3] Maryam Mostajeran. “A Path for Improving Stroke Recovery. Effects of MEK-ERK1/2 Inhibition”. In: (2018).
- [4] Stephanie A. Combs et al. “Effects of an intensive, task-specific rehabilitation program for individuals with chronic stroke: A case series”. In: *Disability and Rehabilitation* 32.8 (Oct. 2009), 669–678. ISSN: 1464-5165. DOI: 10.3109/09638280903242716. URL: <http://dx.doi.org/10.3109/09638280903242716>.
- [5] Johns Hopkins Medicine. *Cerebral Palsy*. Accessed: 2024-08-12. n.d. URL: <https://www.hopkinsmedicine.org/health/conditions-and-diseases/cerebral-palsy>.
- [6] Mayo Clinic. *Guillain-Barré Syndrome - Doctors and Departments*. Accessed: 2024-08-12. n.d. URL: <https://www.mayoclinic.org/diseases-conditions/guillain-barré-syndrome/doctors-departments/ddc-20363037>.
- [7] Yves Zimmermann et al. “ANYexo 2.0: A Fully Actuated Upper-Limb Exoskeleton for Manipulation and Joint-Oriented Training in All Stages of Rehabilitation”. In: *IEEE Transactions on Robotics* 39.3 (June 2023), pp. 2131–2150. ISSN: 1552-3098, 1941-0468. DOI: 10.1109/TRO.2022.3226890. URL: <https://ieeexplore.ieee.org/document/10008060/> (visited on 12/25/2023).
- [8] Tobias Nef et al. “Three-dimensional multi-degree-of-freedom arm therapy robot (ARMin)”. In: *Neurorehabilitation technology*. Springer, 2022, pp. 623–648.
- [9] Agostino De Santis et al. “An atlas of physical human-robot interaction”. In: *Mechanism and Machine Theory* 43.3 (2008), pp. 253–270.
- [10] Hermano Igo Krebs et al. “Robot-aided neurorehabilitation: a robot for wrist rehabilitation”. In: *IEEE transactions on neural systems and rehabilitation engineering* 15.3 (2007), pp. 327–335.
- [11] Sivakumar Balasubramanian, Alejandro Melendez-Calderon, and Etienne Burdet. “A robust and sensitive metric for quantifying movement smoothness”. In: *IEEE transactions on biomedical engineering* 59.8 (2011), pp. 2126–2136.
- [12] Paweł Maciejasz et al. “A survey on robotic devices for upper limb rehabilitation”. In: *Journal of neuroengineering and rehabilitation* 11 (2014), pp. 1–29.
- [13] Nathanaël Jarrassé et al. “Robotic exoskeletons: a perspective for the rehabilitation of arm coordination in stroke patients”. In: *Frontiers in human neuroscience* 8 (2014), p. 947.
- [14] Wietse van Dijk et al. “Improving the transparency of a rehabilitation robot by exploiting the cyclic behaviour of walking”. In: *2013 IEEE 13th International Conference on Rehabilitation Robotics (ICORR)*. IEEE. 2013, pp. 1–8.
- [15] Mathias Bannwart et al. “Systematic analysis of transparency in the gait rehabilitation device the FLOAT”. In: *2016 14th International Conference on Control, Automation, Robotics and Vision (ICARCV)*. IEEE. 2016, pp. 1–6.
- [16] Damiano Zanotto et al. “Improving transparency of powered exoskeletons using force/torque sensors on the supporting cuffs”. In: *2013 IEEE 13th international conference on rehabilitation robotics (ICORR)*. IEEE. 2013, pp. 1–6.
- [17] Etienne Burdet, David W Franklin, and Theodore E Milner. *Human robotics: neuromechanics and motor control*. MIT press, 2013.
- [18] Gerdienke B Prange et al. “Systematic review of the effect of robot-aided therapy on recovery of the hemiparetic arm after stroke”. In: (2009).
- [19] Rui CV Loureiro et al. “Advances in upper limb stroke rehabilitation: a technology push”. In: *Medical & biological engineering & computing* 49 (2011), pp. 1103–1118.
- [20] Tobias Nef, Marco Guidali, and Robert Riener. “ARMin III—arm therapy exoskeleton with an ergonomic shoulder actuation”. In: *Applied Bionics and Biomechanics* 6.2 (2009), pp. 127–142.
- [21] Nathanaël Jarrassé and Guillaume Morel. “Connecting a human limb to an exoskeleton”. In: *IEEE Transactions on Robotics* 28.3 (2011), pp. 697–709.
- [22] V Squeri et al. “Wrist rehabilitation in chronic stroke patients by means of adaptive, progressive robot-aided therapy”. In: *IEEE transactions on neural systems and rehabilitation engineering* 22.2 (2013), pp. 312–325.
- [23] HI Krebs et al. “Increasing productivity and quality of care: Robot-aided neuro-rehabilitation”. In: *Journal of rehabilitation research and development* 37.6 (2000), pp. 639–652.
- [24] Arvid QL Keemink, Herman van der Kooij, and Arno HA Stienen. “Admittance control for physical human-robot interaction”. In: *The International Journal of Robotics Research* 37.11 (2018), pp. 1421–1444.
- [25] Luigi Villani and J De Schutter. *Handbook of robotics, chapter force control*. 2008.
- [26] Neville Hogan. “Impedance control: An approach to manipulation”. In: *1984 American control conference*. IEEE. 1984, pp. 304–313.
- [27] H Igo Krebs et al. “Robot-aided neurorehabilitation”. In: *IEEE transactions on rehabilitation engineering* 6.1 (1998), pp. 75–87.
- [28] Kouhei Ohnishi, Masaaki Shibata, and Toshiyuki Murakami. “Motion control for advanced mechatronics”. In: *IEEE/ASME transactions on mechatronics* 1.1 (1996), pp. 56–67.
- [29] Jaeheung Park and Oussama Khatib. “Multi-link multi-contact force control for manipulators”. In: *Proceedings of the 2005 IEEE International Conference on Robotics and Automation*. IEEE. 2005, pp. 3613–3618.
- [30] Arno HA Stienen et al. “The ACT-4D: a novel rehabilitation robot for the quantification of upper limb motor impairments following brain injury”. In: *2011 IEEE International Conference on Rehabilitation Robotics*. IEEE. 2011, pp. 1–6.

- [31] Levinia Lara Van Der Velden et al. “Development of a single device to quantify motor impairments of the elbow: proof of concept”. In: *Journal of NeuroEngineering and Rehabilitation* 19.1 (Dec. 2022), p. 77. ISSN: 1743-0003. DOI: 10.1186/s12984-022-01050-2. URL: <https://jneuroengrehab.biomedcentral.com/articles/10.1186/s12984-022-01050-2> (visited on 11/27/2023).
- [32] Hiwin Technologies Corp. *ED1 Series Servo Drive User Manual*. First. <https://www.hiwin.tw/>, accessed on August 7, 2024. Hiwin Technologies Corp. Taichung, Taiwan, 2023.
- [33] Hiwin Technologies Corp. *Thunder*. <https://www.hiwin.tw/>. Version 2.1.0. Software, accessed on August 7, 2024. 2023.
- [34] Hiwin Technologies Corp. *TMS3C Series Rotary Table User Manual*. First. Accessed: August 7, 2024. Hiwin Technologies Corp. Taichung, Taiwan, 2023. URL: <https://www.hiwin.tw/>.
- [35] R Munnig Schmidt, Georg Schitter, and Adrian Rankers. *The design of high performance mechatronics: high-Tech functionality by multidisciplinary system integration*. Ios Press, 2020.
- [36] Kuo Yang et al. “Adaptive Trajectory Compensation of Large Inertia Robot”. In: *International Journal of Control, Automation and Systems* 22.3 (2024), pp. 1066–1076.
- [37] Mark Van De Ruit et al. “System identification: a feasible, reliable and valid way to quantify upper limb motor impairments”. In: *Journal of NeuroEngineering and Rehabilitation* 20.1 (May 25, 2023), p. 67. ISSN: 1743-0003. DOI: 10.1186/s12984-023-01192-x. URL: <https://jneuroengrehab.biomedcentral.com/articles/10.1186/s12984-023-01192-x> (visited on 11/27/2023).
- [38] Levinia Lara Van Der Velden et al. “Reliability and Validity of a New Diagnostic Device for Quantifying Hemiparetic Arm Impairments: An Exploratory Study”. In: *Journal of Rehabilitation Medicine* 54 (May 11, 2022), jrm00283. ISSN: 1651-2081. DOI: 10.2340/jrm.v54.12. URL: <https://medicaljournalssweden.se/jrm/article/view/12> (visited on 11/27/2023).
- [39] DJ Reinkensmeyer et al. “Understanding and treating arm movement impairment after chronic brain injury: progress with the arm guide. Journal of Rehabilitation Research and Development”. In: (2000).
- [40] E de Vlugt et al. “A force-controlled planar haptic device for movement control analysis of the human arm”. In: *JOURNAL OF NEUROSCIENCE METHODS* 129.2 (Oct. 30, 2003), pp. 151–168. ISSN: 0165-0270. DOI: 10.1016/S0165-0270(03)00203-6.
- [41] QC Wu et al. “Design and Fuzzy Sliding Mode Admittance Control of a Soft Wearable Exoskeleton for Elbow Rehabilitation”. In: *IEEE ACCESS* 6 (2018), pp. 60249–60263. ISSN: 2169-3536. DOI: 10.1109/ACCESS.2018.2875550.
- [42] QC Wu, ZJ Wang, and Y Chen. “sEMG-Based Adaptive Cooperative Multi-Mode Control of a Soft Elbow Exoskeleton Using Neural Network Compensation”. In: *IEEE TRANSACTIONS ON NEURAL SYSTEMS AND REHABILITATION ENGINEERING* 31 (2023), pp. 3384–3396. ISSN: 1534-4320. DOI: 10.1109/TNSRE.2023.3306201.
- [43] D Tsetserukou et al. “Development of a whole-sensitive teleoperated robot arm using torque sensing technique”. In: *University of Tokyo. WORLD HAPTICS 2007: SECOND JOINT EUROHAPTICS CONFERENCE AND SYMPOSIUM ON HAPTIC INTERFACES FOR VIRTUAL ENVIRONMENT AND TELEOPERATOR SYSTEMS, PROCEEDINGS*. 2007, pp. 476–+. ISBN: 978-0-7695-2738-3.
- [44] S Morante et al. “Force-Sensorless Friction and Gravity Compensation for Robots”. In: *Universidad Carlos III de Madrid. ROBOT 2015: SECOND IBERIAN ROBOTICS CONFERENCE: ADVANCES IN ROBOTICS, VOL 2*. Ed. by LP Reis et al. Vol. 418. 2016, pp. 57–68. ISBN: 2194-5357. DOI: 10.1007/978-3-319-27149-1_5.
- [45] R Kelly, V Santibanez, and F Reyes. “On saturated-proportional derivative feedback with adaptive gravity compensation of robot manipulators”. In: *INTERNATIONAL JOURNAL OF ADAPTIVE CONTROL AND SIGNAL PROCESSING* 10.4 (July 1996), pp. 465–479. ISSN: 0890-6327.
- [46] T Viriyasaranon and IEEE. “Parameters Estimation for an Upper-Extremity Rehabilitation Robot Using Force-sensorless Method”. In: *Asian Institute of Technology. 2016 9TH BIOMEDICAL ENGINEERING INTERNATIONAL CONFERENCE (BMEICON)*. 2016. ISBN: 2334-3052.
- [47] JF Schorsch et al. “The Influence of Human-Robot Interaction Order During Fast Lifting Tasks for Different Levels of Weight Compensation”. In: *Delft University of Technology. 2014 5TH IEEE RAS & EMBS INTERNATIONAL CONFERENCE ON BIOMEDICAL ROBOTICS AND BIOMECHATRONICS (BIOROB)*. 2014, pp. 426–431. ISBN: 2155-1782.
- [48] FC Huang et al. “Negative viscosity can enhance learning of inertial dynamics”. In: *Shirley Ryan AbilityLab. 2009 IEEE 11TH INTERNATIONAL CONFERENCE ON REHABILITATION ROBOTICS, VOLS 1 AND 2*. 2009, pp. 552–557. ISBN: 1945-7898.
- [49] HB Nguyen and PS Lum. “Compensation for the intrinsic dynamics of the InMotion2 robot”. In: *JOURNAL OF NEUROSCIENCE METHODS* 214.1 (Mar. 30, 2013), pp. 15–20. ISSN: 0165-0270. DOI: 10.1016/j.jneumeth.2013.01.001.
- [50] FC Huang, JL Patton, and IEEE. “Evaluation of negative viscosity as upper extremity training for stroke survivors”. In: *Northwestern University. 2011 IEEE INTERNATIONAL CONFERENCE ON REHABILITATION ROBOTICS (ICORR)*. 2011. ISBN: 1945-7898.
- [51] FC Huang and JL Patton. “Augmented Dynamics and Motor Exploration as Training for Stroke”. In: *IEEE TRANSACTIONS ON BIOMEDICAL ENGINEERING* 60.3 (Mar. 2013), pp. 838–844. ISSN: 0018-9294. DOI: 10.1109/TBME.2012.2192116.

- [52] O Baser and EI Konukseven. “Utilization of motor current based torque feedback to improve the transparency of haptic interfaces”. In: *MECHANISM AND MACHINE THEORY* 52 (June 2012), pp. 78–93. ISSN: 0094-114X. DOI: 10.1016/j.mechmachtheory.2012.01.012.
- [53] R VOLPE and P KHOSLA. “A THEORETICAL AND EXPERIMENTAL INVESTIGATION OF IMPACT CONTROL FOR MANIPULATORS”. In: *INTERNATIONAL JOURNAL OF ROBOTICS RESEARCH* 12.4 (Aug. 1993), pp. 351–365. ISSN: 0278-3649. DOI: 10.1177/027836499301200403.
- [54] B Ugurlu et al. “Proof of Concept for Robot-Aided Upper Limb Rehabilitation Using Disturbance Observers”. In: *IEEE TRANSACTIONS ON HUMAN-MACHINE SYSTEMS* 45.1 (Feb. 2015), pp. 110–118. ISSN: 2168-2291. DOI: 10.1109/THMS.2014.2362816.
- [55] B Kim et al. “Impedance Control Based on a Position Sensor in a Rehabilitation Robot”. In: *University of Texas System. 7TH ANNUAL DYNAMIC SYSTEMS AND CONTROL CONFERENCE, 2014, VOL 3. 2014*. ISBN: 978-0-7918-4620-9.
- [56] Y Okada et al. “Motion Support of Upper Extremity with Agonist alone under Negative Admittance Control”. In: *Santa Clara University. 2012 IEEE INTERNATIONAL CONFERENCE ON ROBOTICS AND BIOMIMETICS (ROBIO 2012). 2012*. ISBN: 978-1-4673-2127-3.
- [57] JP Desai et al. “Towards the development of a humanoid arm by minimizing interaction forces through minimum impedance control”. In: *Drexel University. 2001 IEEE INTERNATIONAL CONFERENCE ON ROBOTICS AND AUTOMATION, VOLS I-IV, PROCEEDINGS. 2001*, pp. 4214–4219. ISBN: 1050-4729.
- [58] IS Howard, JN Ingram, and DM Wolpert. “A modular planar robotic manipulandum with end-point torque control”. In: *JOURNAL OF NEUROSCIENCE METHODS* 181.2 (July 30, 2009), pp. 199–211. ISSN: 0165-0270. DOI: 10.1016/j.jneumeth.2009.05.005.
- [59] George Mochizuki et al. “Movement kinematics and proprioception in post-stroke spasticity: assessment using the Kinarm robotic exoskeleton”. In: *Journal of neuroengineering and rehabilitation* 16 (2019), pp. 1–13.
- [60] M Mistry et al. “Arm movement experiments with joint space force fields using an exoskeleton robot”. In: *University of Southern California. 2005 IEEE 9TH INTERNATIONAL CONFERENCE ON REHABILITATION ROBOTICS. 2005*, pp. 408–413. ISBN: 1945-7898.
- [61] M Mistry et al. “An exoskeleton robot for human arm movement study”. In: *University of Southern California. 2005 IEEE/RSJ International Conference on Intelligent Robots and Systems, Vols 1-4. 2005*, pp. 3114–3119. ISBN: 0-7803-8912-3. DOI: 10.1109/IROS.2005.1545450.
- [62] K Shi et al. “Design and analysis of a cable-driven gravity compensation mechanism for spatial multi-DoF robotic systems”. In: *MECHANISM AND MACHINE THEORY* 190 (Dec. 2023). ISSN: 0094-114X. DOI: 10.1016/j.mechmachtheory.2023.105452.
- [63] D Chakarov et al. “Evaluation of the Capabilities of a Hybrid Driven Exoskeleton in Passive Mode of Interaction”. In: *Bulgarian Academy of Sciences. PROCEEDINGS OF THE 18TH INTERNATIONAL CONFERENCE ON INFORMATICS IN CONTROL, AUTOMATION AND ROBOTICS (ICINCO). Ed. by O Gusikhin, H Nijmeijer, and K Madani. 2021*, pp. 442–449. ISBN: 978-989-758-522-7. DOI: 10.5220/0010569004420449.
- [64] J Pan et al. “NESM- γ : An Upper-Limb Exoskeleton With Compliant Actuators for Clinical Deployment”. In: *IEEE ROBOTICS AND AUTOMATION LETTERS* 7.3 (July 2022), pp. 7708–7715. ISSN: 2377-3766. DOI: 10.1109/LRA.2022.3183926.
- [65] SA Ajwad et al. “A COMPREHENSIVE STATE-OF-THE-ART ON CONTROL OF INDUSTRIAL ARTICULATED ROBOTS”. In: *JOURNAL OF THE BALKAN TRIBOLOGICAL ASSOCIATION* 20.4 (2014), pp. 499–521. ISSN: 1310-4772.
- [66] A Riani et al. “Adaptive Integral Terminal Sliding Mode Control of an Upper Limb Exoskeleton”. In: *Universite Paris Saclay. 2017 18TH INTERNATIONAL CONFERENCE ON ADVANCED ROBOTICS (ICAR). 2017*, pp. 131–136. ISBN: 978-1-5386-3157-7.
- [67] RC Luo et al. “Cartesian Position and Force Control with Adaptive Impedance/Compliance Capabilities for a Humanoid Robot Arm”. In: *National Taiwan University. 2013 IEEE INTERNATIONAL CONFERENCE ON ROBOTICS AND AUTOMATION (ICRA). 2013*, pp. 496–501. ISBN: 1050-4729.
- [68] F Zahedi, D Chang, and H Lee. “User-Adaptive Variable Damping Control Using Bayesian Optimization to Enhance Physical Human-Robot Interaction”. In: *IEEE ROBOTICS AND AUTOMATION LETTERS* 7.2 (Apr. 2022), pp. 2724–2731. ISSN: 2377-3766. DOI: 10.1109/LRA.2022.3144511.
- [69] Tobias Nef, Marco Guidali, and Robert Riener. “ARMin III – arm therapy exoskeleton with an ergonomic shoulder actuation”. In: *Applied Bionics and Biomechanics* 6.2 (July 27, 2009), pp. 127–142. ISSN: 1176-2322, 1754-2103. DOI: 10.1080/11762320902840179. URL: <http://content.iospress.com/doi/10.1080/11762320902840179> (visited on 12/23/2023).
- [70] RO Hailey et al. “Impact of Gravity Compensation on Upper Extremity Movements in Harmony Exoskeleton”. In: *Auburn University System. 2022 INTERNATIONAL CONFERENCE ON REHABILITATION ROBOTICS (ICORR). 2022*. ISBN: 1945-7898. DOI: 10.1109/ICORR55369.2022.9896415.
- [71] Anna Olczak, Aleksandra Truszczyńska-Baszak, and Adam Stepień. “The Use of Armeo® Spring Device to Assess the Effect of Trunk Stabilization Exercises on the Functional Capabilities of the Upper Limb—An Observational Study of Patients after Stroke”. In: *Sensors* 22.12 (2022), p. 4336.
- [72] S Goto et al. “Forcefree control with independent compensation for inertia, friction and gravity of industrial

- articulated robot arm”. In: *Saga University*. 2003 IEEE INTERNATIONAL CONFERENCE ON ROBOTICS AND AUTOMATION, VOLS 1-3, PROCEEDINGS. 2003, pp. 4386–4391. ISBN: 1050-4729.
- [73] K. Park et al. “Bimanual shoulder flexion system with surface electromyography for hemiplegic patients after stroke: A preliminary study”. In: *IEEE Int. Conf. Rehabil. Rob.* IEEE International Conference on Rehabilitation Robotics. Journal Abbreviation: IEEE Int. Conf. Rehabil. Rob. 2011. ISBN: 19457901 (ISSN); 978-142449862-8 (ISBN). DOI: 10.1109/ICORR.2011.5975388. URL: <https://www.scopus.com/inward/record.uri?eid=2-s2.0-80055034599&doi=10.1109%2fICORR.2011.5975388&partnerID=40&md5=21df070bbd5c2130701a9a36ecf1c7ad>.
- [74] K Park et al. “Development of mirror image motion system with sEMG for shoulder rehabilitation of post-stroke hemiplegic patients”. In: *INTERNATIONAL JOURNAL OF PRECISION ENGINEERING AND MANUFACTURING* 13.8 (Aug. 2012), pp. 1473–1479. ISSN: 2234-7593. DOI: 10.1007/s12541-012-0194-0.
- [75] Fabian Just et al. “Exoskeleton transparency: feed-forward compensation vs. disturbance observer”. In: *at-Automatisierungstechnik* 66.12 (2018), pp. 1014–1026.
- [76] MS Erden and A Billard. “Robotic Assistance by Impedance Compensation for Hand Movements While Manual Welding”. In: *IEEE TRANSACTIONS ON CYBERNETICS* 46.11 (Nov. 2016), pp. 2459–2472. ISSN: 2168-2267. DOI: 10.1109/TCYB.2015.2478656.
- [77] F Zahedi et al. “Variable Damping Control for pHRI: Considering Stability, Agility, and Human Effort in Controlling Human Interactive Robots”. In: *IEEE TRANSACTIONS ON HUMAN-MACHINE SYSTEMS* 51.5 (Oct. 2021), pp. 504–513. ISSN: 2168-2291. DOI: 10.1109/THMS.2021.3090064.
- [78] YP Pan et al. “Adaptive Command-Filtered Backstepping Control of Robot Arms With Compliant Actuators”. In: *IEEE TRANSACTIONS ON CONTROL SYSTEMS TECHNOLOGY* 26.3 (May 2018), pp. 1149–1156. ISSN: 1063-6536. DOI: 10.1109/TCST.2017.2695600.
- [79] F Tajaddodianfar et al. “TRANSPARENCY ENHANCEMENT OF HAPTIC SYSTEMS BASED ON COMPENSATION OF DEVICE DYNAMICS”. In: *Sharif University of Technology*. IMECE 2009: PROCEEDINGS OF THE ASME INTERNATIONAL MECHANICAL ENGINEERING CONGRESS AND EXPOSITION, VOL 10, PTS A AND B. 2010, pp. 103–110. ISBN: 978-0-7918-4383-3.
- [80] D Kim. “Compliant Motion Control for a Compliant Rehabilitation System”. In: *University of Michigan System*. PROCEEDINGS OF THE IEEE/RAS-EMBS INTERNATIONAL CONFERENCE ON REHABILITATION ROBOTICS (ICORR 2015). Ed. by HY Yu, D Braun, and D Campolo. 2015, pp. 422–427. ISBN: 1945-7898.
- [81] S Dalla Gasperina et al. “Development and Electromyographic Validation of a Compliant Human-Robot Interaction Controller for Cooperative and Personalized Neurorehabilitation”. In: *FRONTIERS IN NEURO-ROBOTICS* 15 (Jan. 18, 2022). ISSN: 1662-5218. DOI: 10.3389/fnbot.2021.734130.
- [82] Levinia Lara van der Velden et al. “The diagnostic levels of evidence of instrumented devices for measuring viscoelastic joint properties and spasticity; a systematic review”. In: *Journal of NeuroEngineering and Rehabilitation* 19.1 (2022), pp. 1–8.
- [83] Mokhlis Salah-eddine, Said Sadki, and Bahloul Bensassi. “Microcontroller based data acquisition and system identification of a dc servo motor using arx, armax, oe, and bj models”. In: *Advanced Science and Technology Engineering System (ASTES) Journal* 5.6 (2020), pp. 507–513.
- [84] Qing-Chang Zhong. *Robust control of time-delay systems*. Springer Science & Business Media, 2006.
- [85] Roger M Enoka. *Neuromechanics of human movement*. Human kinetics, 2008.
- [86] Henry W Ott. *Electromagnetic compatibility engineering*. John Wiley & Sons, 2011.

VIII. APPENDIX

A. Systematic Review

Effective compensation for gravity and friction in robotic systems is well-established. However, inertia compensation strategies remain underdeveloped due to the absence of standardized evaluation methods for comparing techniques and assessing transparency [36].

Using the PRISMA method, a systematic review analyzed controller strategies in diagnostic and rehabilitative upper limb robotic devices. The search query, detailed in Table II, addressed challenges posed by inertia and factors affecting human-robot interaction, such as friction, gravity, and nonlinear dynamics. The review identified various controllers aimed at mitigating inertia while enhancing transparency between human and robotic devices.

Most studies implement Proportional-Derivative (PD) or Proportional-Integral (PI) controllers to actuate robotic drives. PD controllers are widely preferred for their stability in systems with inertia and damping, as well as their fast response times and ability to reduce undesired oscillations. These features ensure smooth and controlled movements, critical for patient safety. However, PD controllers are less effective in minimizing steady-state errors compared to Proportional-Integral-Derivative (PID) controllers.

Following the PRISMA method, articles are selected or excluded based on defined criteria. Of the 459 articles initially identified, 64 (13.9%) undergo critical review. These studies are categorized based on additional criteria and summarized in Table III, which also illustrates robotic devices grouped by Degree of Freedom.

1) *Feedforward Approach*: Feedforward control methodologies predict control inputs based on system models and anticipated user interactions, avoiding continuous feedback. These controllers utilize known disturbances, such as inertia, gravity, and friction, by employing precise models to cancel their effects. This approach enhances transparency and accuracy, particularly in rehabilitative movements, and improves trajectory tracking. However, the effectiveness diminishes with model inaccuracies or nonlinearities, potentially leading to jittering and oscillations. Feedforward control, initially favored over feedback methods, avoids the computational burden and error propagation associated with differentiating position into velocity and acceleration.

In rehabilitative robotics, trajectory planning and inverse dynamics control are widely used. Trajectory planning involves pre-programming movement paths that account for inertia, minimizing perceived resistance. Inverse dynamics control calculates the required joint torques to achieve desired movements, compensating for inertia by pre-emptively applying the necessary forces.

In diagnostic robotics, both model-based and learning-based feedforward controls are applied. Model-based feedforward control relies on detailed system models to compute control inputs for specific diagnostic movements, reducing inertia. Learning-based feedforward control uses data from previous interactions to predict and apply control inputs, proving particularly effective for repetitive diagnostic tasks.

2) *Feedback Approaches*: Feedback-based methodologies, summarized in Table IV, utilize real-time sensor data to dynamically adjust the robot's behaviour. These systems continuously monitor the robot's interaction with the user, adjusting control inputs to create the effect of negative inertia. A common technique involves disturbance observers, which estimate and compensate for external influences such as gravity, friction, and inertia in real-time. This approach offers greater robustness and adaptability to unforeseen disturbances compared to feedforward control. Disturbance observers estimate position through double integration, reducing computational costs and errors, and making them suitable for diagnosing and rehabilitating patients with neurological or motor impairments. However, their effectiveness relies on accurate, high-sampling-rate sensors to minimize feedback delays. Stability challenges in certain scenarios may limit this approach.

In rehabilitative robotics, Proportional-Derivative (PD) control and impedance control are frequently employed. PD control dynamically adjusts forces based on feedback from position and velocity sensors, reducing perceived inertia by fine-tuning proportional and derivative gains. Impedance control modifies the dynamic relationship between force and movement, simulating lower inertia to make movements smoother and easier for patients.

In diagnostic robotics, adaptive control and Model Predictive Control (MPC) prove effective. Adaptive control continuously adjusts the robot's behaviour based on user movements, tailoring assistance or resistance to achieve precise control. MPC utilizes real-time feedback and predictive models to anticipate future states, adjusting control inputs to enable accurate neuromuscular assessments.

3) *Unexplored Approaches - Sensorless or AI*: This category includes methods that do not fit neatly into feedback or feedforward classifications, such as sensorless techniques and AI-based approaches.

In rehabilitative robotics, both sensorless control and AI-based methods are explored. Sensorless control relies on minimal sensor data, using the robot's intrinsic properties to approximate inertia effects through passive compliance or intrinsic joint damping. AI-based control employs machine learning algorithms to predict and adjust control inputs based on both historical and real-time data, delivering customized negative inertia effects.

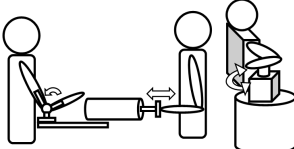
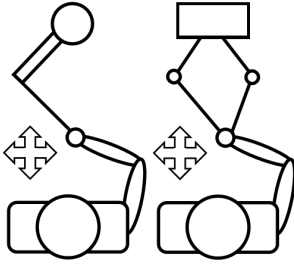
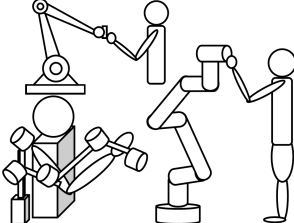
In diagnostic robotics, sensorless estimation and AI techniques play significant roles. The sensorless estimation uses motor current measurements to infer applied forces, adjust control inputs and simplify the system while maintaining effective inertia compensation. AI and machine learning techniques analyze large datasets from diagnostic sessions to develop predictive models, enhancing accuracy and user experience over time.

4) *Which is Better?*: Each strategy for implementing negative inertia presents distinct advantages and challenges, depending on the application context. The choice between feedforward model-based controllers and disturbance observers depends on specific requirements. Feedforward models excel when accurate dynamic modelling is achievable and precise trajectory tracking is essential. In contrast, disturbance ob-

TABLE II: Search Query Formulation

CONCEPTS							
SYNONYMS	Goal	AND	Dynamics	AND	Device	AND	Target
	OR		OR		OR		OR
	“Negative” “Compensation” “Transpar*”		“Inertia” “Admittance” “Impedance”		“Rehabilitative” “Assistive” “Robotics” “Exoskeleton” “Ortho*” “Haptics” “Identification”		“Arm” “Hand” “Shoulder” “Elbow”

TABLE III: Graphic Representation of Device Type and Purposes

Scheme	DOF	Devices	Purpose
	1	SEP Hankamp[37, 38] ARM Guide[39] TU Delft Hydraulic Manipulator [40] Wearable Exoskeletons[41] [42] Joint manipulators [43–47]	These devices allow focused assessments, isolating specific joint or muscle limitations. In therapy, their simplicity enables targeted exercises, closely mimicking real-world movements for effective and tailored rehabilitation
	2-3	Planar robots [40, 48–52] MIT-MANUS*[53] InMotion2[49] Exoskeletons[54] Robotic Arm[55–57] vBOT, WristBot [58] Enhanced planar robots (i.e. Kinearm) [59]	These provide enhanced haptic interfaces and force field implementation during reaching movements. The added DOF enables therapists to simulate natural interactions of ADL tasks while allowing for better diagnoses as well as subsequent rehabilitation
	4-14	Exoskeletons [60–64] Robotic Arm[65–68] Armin I-V[69] ANYexo[7] Bimanual Arms[63, 70] Armeo Exoskeleton [71]	These offer a more comprehensive range of motion in the joint space, enabling complex, compound movements. This allows for muscle synergies facilitation of more natural movement and thus improving rehabilitation. Providing a more holistic approach to rehabilitation and diagnoses enhancing coordination of muscle groups and improving neurological impairments

*MIT-MANUS is a 2-DOF planar robot with a 3-DOF manipulator in the robot’s wrist.

servers better adapt to dynamic and unpredictable interactions, making them more suitable when human input introduces uncertainties. Enhanced transparency is particularly valuable for diagnostic devices, which prioritize evaluating limb dynamics and properties such as viscoelasticity, spasticity, muscle weakness, and synergies.

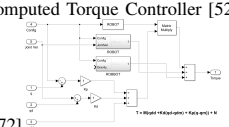
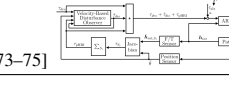
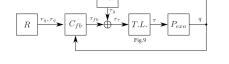
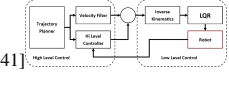
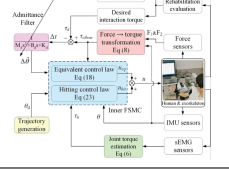
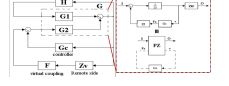
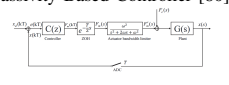
Recent advancements in exoskeletal devices, such as ARMin IV+ and ARMin V, increasingly favour disturbance observers over feedforward compensatory control. The ANYexo 2.0 exoskeleton, for example, integrates feedforward terms for position, velocity, and torque control with observers to mitigate unknown disturbances. This hybrid approach reflects evolving strategies in advanced robotic systems.

Feedback-based methodologies offer high precision and

adaptability, making them ideal for dynamic rehabilitation exercises. However, they require extensive sensor integration and real-time data processing, increasing system complexity and cost. Feedforward-based methods provide effective control for predictable, repetitive diagnostic procedures but struggle with real-time adaptation. They simplify control design by relying on precomputed models, which demand accurate system modelling.

Alternative approaches, including sensorless and AI-based methods, balance simplicity, adaptability, and user experience. Sensorless methods simplify implementation but may lack fine-tuned control. AI-based approaches, though computationally intensive, offer high adaptability and precision by tailoring interactions to individual users.

TABLE IV: Low-level controller strategies

Control Techniques	Description	Advantages	Disadvantages
<p>Computed Torque Controller [52, 72]</p> 	calculating the torques required to generate the desired joint accelerations and compensating for factors such as gravity, inertia, and friction. By accurately computing and applying these torques, the controller aims to achieve the desired motion while ensuring the stability and accuracy of the robotic arm's movements	Feedback and Energy gains are marginal. Reduction of computational expense after defining trajectory.	precise model required. Reduced stability for unmodelled dynamics.
<p>Disturbance Observer Control [46, 54, 65, 68, 73–75]</p> 	An observer that continuously estimates and compensates for external disturbances or uncertainties affecting the system. The disturbance observer monitors and reacts to disturbances such as unexpected forces or changes in the environment.	Provides estimation of friction. Individual joint control. No additional sensor is required	Saturation of torque due to higher disturbances. Frequency tuning is difficult, complex friction calculation.
<p>Model Predictive Control [76]</p> 	MPC uses a dynamic model of the system to predict its behaviour over a future time horizon. The controller then generates a sequence of control inputs that minimizes a cost function, considering both the current state of the system and the predicted future states	Easy tuning. Model uncertainties handled. Actuator limitation handled	Complex number of coefficients required
<p>Linear Quadratic Regulator [41]</p> 	employs optimal control theory to determine the feedback gains that minimize the specified cost function. It provides a systematic way to balance the trade-off between achieving desired performance and minimizing control effort	State feedback is utilised to compute the best input. Guarantees stability. The same dynamics for MIMO and SISO systems	Model inaccuracy causes instability. Observer inclusion makes the system complex
<p>Sliding Model Control [41, 66, 77, 78]</p> 	the sliding surface is defined based on the difference between the desired and actual states of the system. The control law is designed to ensure that the system state converges to this sliding surface and stays on it, providing robust performance in the face of disturbances and uncertainties. Sliding mode control is known for its ability to handle nonlinearities and uncertainties	Model-independent trajectory in sliding phase. Low sensitivity to uncertainty in the model.	cogging or chattering due to discontinuities. lack of robustness in the reaching phase.
<p>H - Infinity Controller [79]</p> 	control formulates the control design as an optimization problem to minimize the worst-case impact of disturbances on the system's performance. It involves specifying a performance criterion, such as tracking accuracy, and simultaneously minimizing the influence of disturbances and uncertainties	Can handle model uncertainty, and complexity. Cross-coupling and multivariate systems are better controlled	Poor torque saturation handling. Controller limited to defined cost-function
<p>Passivity Based Controller [80]</p> 	the control design focuses on maintaining the system's energy balance. The controller is designed to ensure that the total energy in the system is dissipated over time, preventing the accumulation of energy and ensuring stability. This approach can enhance the robustness of the robotic arm's control	damping term ensures passivity and desired dynamics are achieved for non-linearities. asymptotic stability guaranteed.	Complicated tuning. Passivity through error mapping only.

5) *The Right Controller Strategy?*: Choosing between admittance and impedance control depends on the specific application requirements. Admittance control provides natural interaction and adaptability, making it well-suited for scenarios with variable user input and critical compliance. In contrast, impedance control excels in tasks requiring precise force and position regulation, offering stability in controlled environments. Some devices integrate both control strategies in a hybrid approach to accommodate different therapeutic or diagnostic functions. For instance, Dalla Gasperina et al. and Van der Velden et al. implement various operational modes to address passive, transparent, corrective, and weight counter-gravity modes, or to perform specific diagnostic tasks such as assessing muscle strength, synergy, elasticity, and spasticity [31, 81].

The choice of negative inertia compensation strategy should be guided by the application's needs, desired interaction level, and available resources. Feedback-based methodologies are optimal for dynamic, interactive tasks, while feedforward-based methods are ideal for controlled, repetitive procedures. Sensorless and AI-based techniques present alternative solutions that enhance user experience and adaptability. Understanding these strategies in rehabilitative and diagnostic

robotics is crucial for developing responsive and effective systems for upper extremity impairments.

6) *Conclusion*: Robotic technologies have significantly advanced diagnostic and rehabilitative practices for upper extremity impairments. Diagnostic robots offer valuable insights into neuromuscular and biomechanical functions, while rehabilitative robots enhance recovery by improving movement and coordination. Implementing negative inertia makes interactions feel natural and effortless. This thesis explores strategies for implementing negative inertia in diagnostic robots to enhance responsiveness and sensitivity. Feedback-based methodologies provide high precision for dynamic rehabilitation tasks, feedforward-based methods excel in controlled diagnostic settings, and sensorless and AI-based approaches improve user experience and adaptability. Understanding these strategies is essential for developing responsive and effective robotic systems for upper extremity impairments.

B. The Hardware

1) *The ACT4D*: The ACT-4D, illustrated in Figure 30, quantifies arm impairments during functional movements using a modified MOOG HapticMaster. The blue JR3 6-DOF force/torque sensor in Figure 31 is used for the HapticMaster's



Fig. 30: The very first shoulder elbow perturber [30]

admittance control, but not for the Elbow System. A horizontally mounted sensor drum on ball bearings rotates freely around its vertical axis, connected via cables and a gearbox drum to the Harmonic Drive actuator and gearbox.

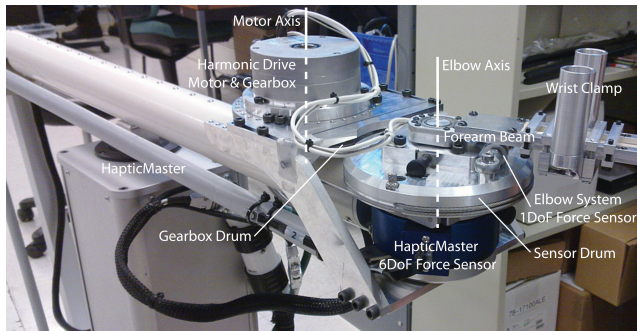


Fig. 31: The breakdown of the ACT4D Hardware [30]

From Figure 31, the forearm beam attached to the sensor drum is hinged with ball bearings around the vertical axis of the Elbow System but is rotationally locked to the sensor drum. A 1-DOF force sensor, fixed at a distance from the elbow axis, measures applied elbow torques. Elbow rotations are measured by a magnetic potentiometer in the sensor drum and two accelerometers on the beam. The forearm is secured to the beam via an orthosis and wrist cylinders or a subject-specific forearm cast.

2) Shoulder Elbow Perturbator - Rijndam, Erasmus MC:

The shoulder elbow perturbator, developed by Hankamp Rehab in Figure 32, perturbs the elbow joint angle while passively supporting the arm through an innovative Sarrus linkage mechanism. A cable attached to a spring routed through pulleys ensures gravity compensation is independent of mechanism height.

Perturbation is provided by a high torque rotary table (HiWin TMS3C) aligned with the elbow joint. Two force sensors, a strain gauge load cell (Futek LCM200) and a piezoelectric load cell (Kistler 9321B), are attached in series with the forearm support. An infrared proximity sensor (Sharp 2Y0A21) measures vertical displacement. A servo controller (HiWin D1) controls the drive, while sensors connect to a Beckhoff terminal, controlled via a real-time PC (HP work-book) using EtherCAT protocol.

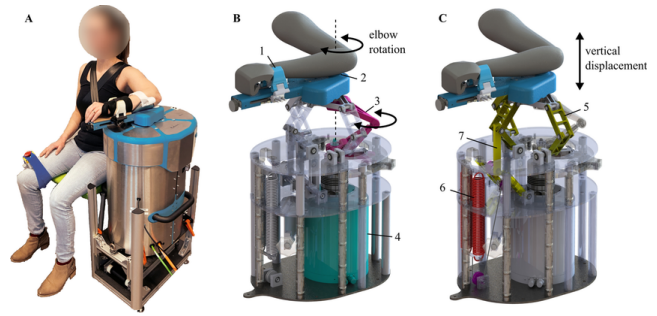


Fig. 32: The First Purpose-Built SEP [82]

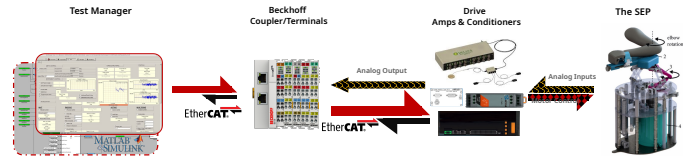


Fig. 33: Operation of the Rijndam SEP

A test manager program created in Simulink (Matlab) communicates with the Beckhoff coupler and HiWin drive at a 1 kHz rate using the EtherCAT library. The SEP also reserves analog inputs for an EMG amplifier (Delsys) connection for participants, though the Kistler sensor remains unconnected in this setup. Illustrated in Figures 33 and 34

The SEP comprises two components: a unit housing the rotary table platform with the Sarrus linkage and gravity compensation mechanism, and a separate control cabinet housing the control laptop, motor driver, power supplies, signal conditioners, terminals, and couplers.

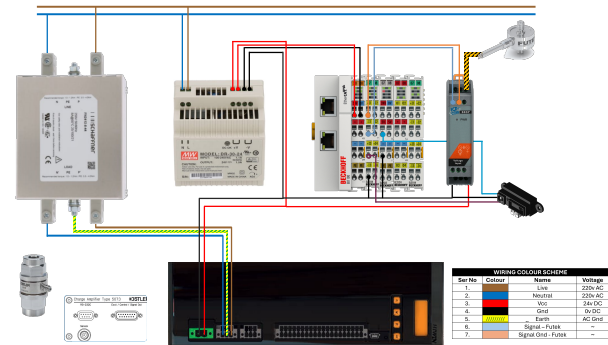


Fig. 34: The wiring scheme for the Rijndam SEP

3) Shoulder Elbow Perturbator - Amsterdam UMC:

Version 2 of the Shoulder Elbow Perturbator (SEP), used by Amsterdam UMC, incorporates several key improvements over Version 1 used by Rijndam. The Sarrus mechanism is reworked for increased rigidity and the forearm height adjustment jack is modified. The enclosure is enhanced for better patient safety, and the entire package is consolidated into a single unit, making it heavier but more stable and reducing its overall footprint.

The electronics also see significant changes. While the rotary table remains the same (HiWin TMS3C), the drive is upgraded to the Hiwin ED1, providing a more precise

TABLE V: Specification Comparison

	ACT4D	SEP Rijndam	SEP Amsterdam
Motor	FHA-17C-DC24	Hiwin TMS3C	Hiwin TMS3C
Encoder	3600 lines/cycle *100	3600 lines/cycle	4325376 or 8192 counts/rev
Drive	Accelnet ACP-090-36	Hiwin D1n-36	Hiwin ED1-01
Mechanism	1:100 Harmonic Reducer	Direct drive	Direct Drive
Force Sensor	Omega LC201	Futek LCM200 Kistler 9321b	Futek LCM200
Signal Conditioner		ICPDAS SG3016 Kistler 5073	AIAA100
Accelerometer	2 x 3 axis Accelerometers	-	1 x 3-Axis ADXL 337
Target PC	Quansar	HP Workbook (Linux)	Lenovo Ideapad(Windows)
Coupler		EK1100	EK1100
Terminals		2x EL3104 1x EL9505 1x EL2124	1x EL3102 1x EL2002 1x EL1202
Device Inertia	0.050 Kgm^2	0.045 Kgm^2	0.043 Kgm^2
Torque	75 Nm	60 Nm (180 Nm peak)	60 Nm (180 Nm peak)
Velocity	450 $^\circ/s$	1800 $^\circ/s$	1800 $^\circ/s$
Acceleration	4500 $^\circ/s^2$	18000 $^\circ/s^2$	18000 $^\circ/s^2$

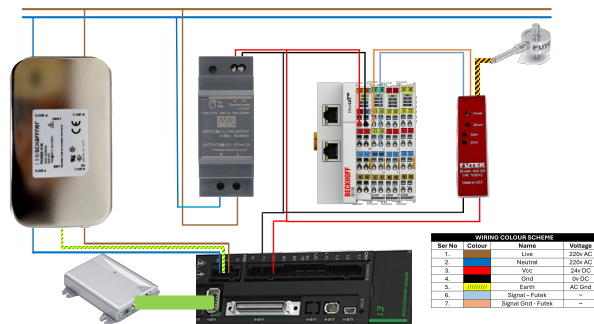


Fig. 35: Wiring and Component Scheme for the Amsterdam SEP

rotary encoder. Only one force sensor (Futek LCM 200) is used, connected to a Futek signal conditioner (Futek IAA100). The displacement sensor is omitted, and the Beckhoff coupler (EK1100) now uses fewer terminals (1x EL3102, 1x EL2002, 1x EL2102). Illustrated in Figure 36.

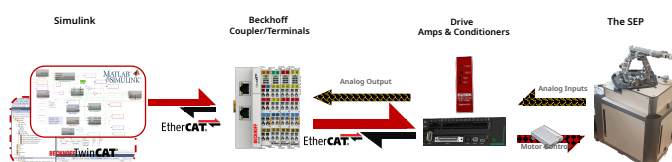


Fig. 36: Operation of the Amsterdam SEP

The control system transitions from a Linux-based test

manager to Twincat 3 for Windows. The workflow, illustrated in Figure 36, involves compiling the model in Simulink and running it with Twincat 3 at a 1 kHz rate. The comparison is summarised in Table V.

C. The Right Controller

1) *Background*: To assess the performance of negative inertia, a high-level control methodology is implemented. Two popular techniques, impedance and admittance controllers, are fundamental for managing human-robot interactions. Both controllers regulate the robot's dynamic behaviour, ensuring safety, precision, and adaptability to external forces.

2) *Impedance Control*: Impedance control regulates the relationship between detected motion and applied force through open or closed-loop control. The robot behaves like a second-order mass-spring-damper system, aiming to control its response to external motions. The equation of motion is:

$$F = M\ddot{x} + B\dot{x} + Kx \quad (14)$$

where F is the force, x is the displacement and M, B, K represent the desired inertia, damping and stiffness respectively. Impedance control is advantageous in scenarios with varying and unpredictable forces, providing robust interaction dynamics, stability, and responsiveness. It's ideal for precise force control in applications like surgical robots, robotic rehabilitation, and teleoperation.

Implementing negative inertia requires precise tuning to avoid instability, necessitating highly responsive sensors and real-time computation.

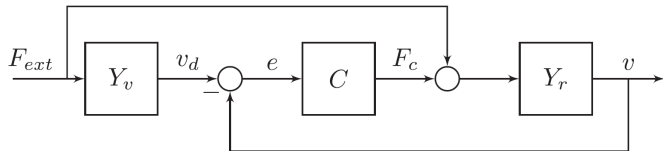


Fig. 37: The admittance control diagram for a robot depicts the interaction between the robot dynamics, external forces, virtual dynamics, and the control system. The diagram illustrates the measured externally applied force F_{ext} , which influences the robot dynamics Y_r directly and passes through virtual dynamics Y_v to generate a velocity reference v_d . A controller C attempts to enforce this velocity reference by generating a control force F_c , which is applied to the robot through an actuator (not shown). The resulting motion of the robot is denoted as v . [24]

3) *Admittance Controller*: Admittance control as shown in Figure 37 regulates the relationship between measured force and velocity reference, defining how much a robot displaces after force application. The equation of motion is:

$$x = \frac{1}{M} \iint F, dt + \frac{1}{B} \int F, dt + \frac{1}{K} F \quad (15)$$

where, x is the displacement, F is the force and M, B, K are the inertia, damping and compliance (inverse of stiffness) respectively.

Admittance control is ideal for robots needing precise trajectory following in response to external forces, making it suitable for collaborative and assistive robots.

This approach simplifies motion response modification rather than force response, requiring precise but not extremely high-bandwidth force sensors.

4) *Summary*: The choice between admittance and impedance control depends on specific application needs. Impedance control manages robot reactions to external forces, ensuring stability and adaptability, while admittance control excels in precise motion trajectory following. Advanced HRI systems often combine both strategies for balanced force responsiveness and motion precision. Impedance control, easier for modifying dynamic responses, is generally preferable for implementing negative inertia, although challenging for rendering stiff virtual surfaces. Admittance control, while simpler for stiff surfaces, struggles with low inertia, making it suitable for applications like the SEP where negative inertia enhances dynamic interactions.

D. System Modelling

1) *Background*: From Figure 38, the motion control system integrates both feedforward and feedback control to regulate the plant, which consists of the power amplifier, actuator, and mechanical dynamics. The diagram identifies different points where disturbances can interfere with the system. The

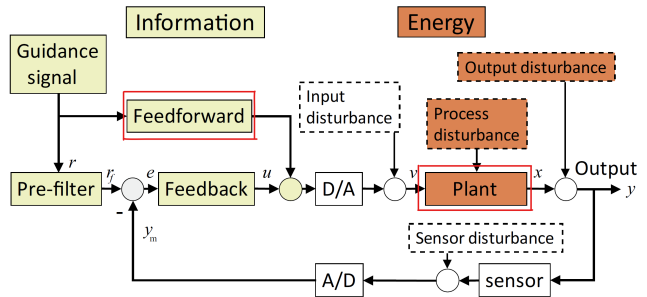


Fig. 38: A standard control loop for high-performance robots. [35]

commonly used symbols in control engineering are: r [m] representing the reference signal, r_f [m] as the filtered reference signal, e [m] as the error signal, u [N] as the control force to be applied, v [N] as the real force applied, x [m] as the plant output motion, y [m] as the measured output motion, and y_m [m] as the measurement value of the measured output motion.

In this system, the reference signal r represents the desired position or motion. After passing through a filter to remove high-frequency components, it becomes the filtered reference signal r_f . The error signal e is the difference between the filtered reference signal r_f and the measured output y . The controller calculates the control force u to correct this error. However, the real force applied v may differ from u due to disturbances. The actual motion of the plant, including any response to disturbances, is denoted as x . The measured output motion y is obtained from sensors, and the measurement value y_m includes any noise or inaccuracies from the measurement system.

Disturbances can affect the system at various points, such as between the control force u and the real force v , or within the plant affecting the output motion x . Effective control strategies aim to minimize the impact of these disturbances, ensuring the system follows the reference signal as closely as possible.

2) *System Modeling*: Modelling the dynamics of a robot is crucial for implementing effective control strategies, especially for feedforward inertial compensation. Feedforward control aims to predict and counteract the effects of inertia, improving the system's responsiveness and precision. Accurate dynamic models enable the design of controllers that can anticipate and compensate for the robot's motion, reducing lag and enhancing performance in tasks requiring high-speed and high-accuracy movements.

The dynamics of the SEP (one degree of freedom) robot can be modelled mechanically as a mass-spring-damper system. Simplifying the mass of the robot and the mass post sensor as a single mass due to the rigid connection via the force sensor turns it into a simple mass-spring-damper system. In this model, the robot's joint or end-effector is represented by a mass m , connected to a spring with stiffness k and a damper with damping coefficient b . The equation of motion for the mass-spring-damper system is given by:

$$m \frac{d^2x}{dt^2} + b \frac{dx}{dt} + kx = F \quad (16)$$

Applying the Laplace transform to this equation, assuming zero initial conditions, we get:

$$ms^2X(s) + bsX(s) + kX(s) = F(s) \quad (17)$$

Solving for $X(s)$:

$$X(s) = \frac{F(s)}{ms^2 + bs + k} \quad (18)$$

When integrating the motor dynamics, the external force F is the torque produced by the motor. Using the electromagnetic torque equation of a PMSM and considering the motor's electrical dynamics, we have:

$$F(s) = T_e(s) = \frac{3}{2}P[\lambda_f I_q(s) + (L_d - L_q)I_d(s)I_q(s)] \quad (19)$$

The voltage equations in the dq -reference frame in the Laplace domain are:

$$V_d(s) = R_s I_d(s) + L_d s I_d(s) - \omega L_q I_q(s) \quad (20)$$

$$V_q(s) = R_s I_q(s) + L_q s I_q(s) + \omega L_d I_d(s) + \omega \lambda_f \quad (21)$$

By combining the mass-spring-damper system dynamics with the motor's electrical model in the Laplace domain, we can fully describe the behaviour of the 1DOF robot. The overall system dynamics in the Laplace domain are given by:

$$X(s) = \frac{\frac{3}{2}P[\lambda_f I_q(s) + (L_d - L_q)I_d(s)I_q(s)]}{ms^2 + bs + k} \quad (22)$$

where the current dynamics $I_d(s)$ and $I_q(s)$ are governed by the Laplace-transformed voltage equations above. By obtaining the system frequency response with accurately estimated parameters, we can enhance the robot's performance for high-speed and high-accuracy tasks.

3) *Parameter Selection*: The parameters for the mathematical model are estimated based on device specifications and approximate figures for the motor EMF and impedance parameters. The inertia of the rotary table is obtained from the manual, while the torsional stiffness is estimated based on the size, weight, and type of the servo motor, specifically the rotary table. The damping is calculated using $B = 2\zeta\sqrt{MK}$, with a damping ratio ζ of 0.7 for an underdamped system. The torsional stiffness is estimated to be 50,000 Nm/ θ , resulting in a damping coefficient of 58.56 Nm/s. The stator resistance, inductances, and pole pairs were obtained from the manual, while the flux leakage and angular velocity were estimated from nominal values.

The parameters are as follows:

- Inertia: $m = 0.035 \text{ kg} \cdot \text{m}^2$
- Damping: $b = 58.56 \text{ Nm/s}$
- Stiffness: $k = 50,000 \text{ Nm}/\theta$
- Stator Resistance: $R_s = 17.1 \Omega$
- d-axis Inductance: $L_d = 0.0844 \text{ H}$
- q-axis Inductance: $L_q = 0.0844 \text{ H}$
- Flux Leakage: $\omega_b = 1.12 \text{ H}$
- Pole Pairs: $P = 11$
- Electrical Angular Velocity: $\omega = 100 \text{ rad/s}$

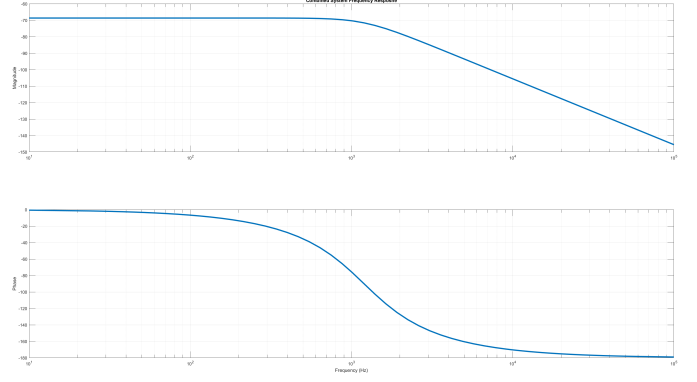


Fig. 39: The system behaves like a conventional mass-spring-damper system with stiffness around -70dB for the lower frequencies, damping around 1kHz after which the system has a -2 inertial slope while the phase lags approaches -180° for the higher frequencies $\leq 10\text{kHz}$ showing asymptotic stability.

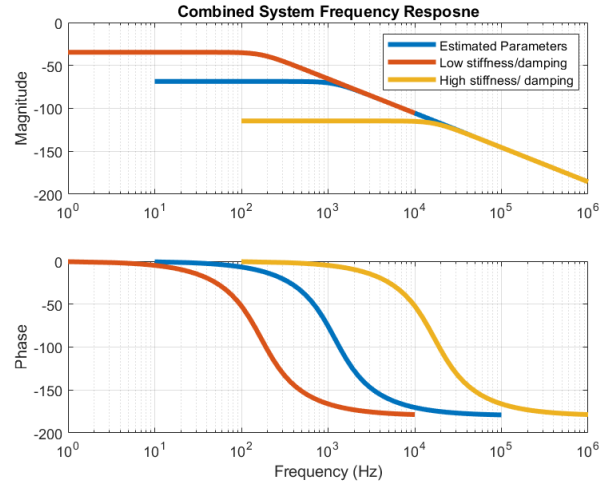


Fig. 40: By changing the stiffnesses and damping coefficients, the magnitude changes due to stiffness, and the phase shifts as well.

4) *Frequency Response Analysis*: The frequency response in Figure 39 aligns with the expected outcome for a conventional mass-spring-damper (M-B-K) system. However, given that some parameters were estimated, two additional frequency responses were generated with different stiffness values and the corresponding derived damping coefficients. Initially, the torsional stiffness was set to a lower value of 1000 Nm/ θ , resulting in a calculated damping coefficient of 8.365 Nm/s. The other scenario involved a higher stiffness of $10^7 \text{ Nm}/\theta$, with a calculated damping of 836.5 Nm/s. The results are illustrated in Figure 40.

Lower stiffness and damping result in a higher magnitude for the stiffness and a transition from stiffness behaviour to inertial behaviour at 200 Hz compared to the standard model at 1200 Hz. The phase also transitions at 30 Hz instead of 300 Hz. Conversely, the higher stiffness scenario shows a lower stiffness magnitude and a transition frequency of around 10 kHz.

Comparing system identification and mathematical modelling approaches for M-B-K systems offers distinct insights and limitations, especially concerning nonlinear dynamics. System identification can capture complex behaviours not modelled here, including nonlinearities like cogging, mechanical compliance, friction, resonance, and other parasitic dynamics, reflecting their significant impact on the system response. In contrast, M-B-K models often simplify these effects, potentially omitting critical nonlinear characteristics. While M-B-K models provide a foundational understanding of system dynamics, system identification can offer a more comprehensive and precise representation, essential for high-precision applications where these nonlinearities critically affect performance. Comparing both approaches reveals the necessity of addressing complex dynamics for accurate modelling and control.

E. System Identification

1) *The Recipe*: System identification offers a robust approach to model complex mechanical systems with nonlinearities like cogging in motors, additional compliances from 3D printed parts, and compliance in Sarrus linkages. Unlike traditional methods, system identification derives models directly from experimental data, effectively accommodating these nonlinear behaviours. This method is crucial for accurately capturing interactions between components, optimizing control strategies, and enhancing overall system performance. Moreover, the system order can be predefined, allowing for better parameter estimation and model fitting, reducing computational costs.

The process for system identification is as follows:

1) Prepare Experiment

- Define a model for the system.
- Choose a sampling frequency that is high enough to observe the relevant dynamics and prevent aliasing. However, a higher sampling frequency can lead to larger data set sizes. Select an adequate observation time. Longer observation times are better for noise removal from an ergodic signal, though it is a trade-off with available memory for recording.
- Multiple repetitions are beneficial for noise reduction and observing discrepancies between recordings.
- Define the perturbation signals based on expected system dynamics. Multisine or pseudorandom binary sequences are ideal as they need to be persistently exciting and prevent leakage, with prime numbers preventing even or odd harmonics.

2) Perform Experiment

- Apply the perturbation signal to the system and record the output response. It is important to record the same modality of signals; if the input signal is a position perturbation, the output should also be a position perturbation, not force, torque, or velocity.
- Take exceptional care to prevent noise, whether from the environment (mechanical or electromagnetic) or irrelevant sources.

3) Analyze the Results

- Analyze the input and output signals.
- Check for linearity through coherence and determine whether open or closed-loop algorithms are required.
- Perform system identification to obtain a non-parametric description of the system using frequency or impulse response functions.
- Derive a parametric model and fit it to the data using various techniques. Evaluate the fit and validity of the model using metrics such as Variance Accounted For (VAF) or Standard Error of the Mean (SEM).

System identification is an essential tool for modelling complex mechanical systems, providing detailed insights and accurate representations of system dynamics. This approach ensures precise control and optimization, especially in applications where nonlinearities significantly impact performance.

2) *The Right Signals*: In a system identification experiment using the shoulder-elbow perturbator (SEP) robot operating in cyclic synchronous position mode, multiple multisine signals are synthesized, shown in Figure 41 to study the dynamic response of the joint system. These multisine signals consist of prime frequencies within the ranges of 0 to 11 Hz, 0 to 23 Hz, and 0 to 100 Hz. Using prime frequencies ensures that each frequency component remains distinct, avoiding harmonic overlap and facilitating clearer system identification. The amplitudes of these signals are set to 3° , 1° , and 0.1° , respectively, as higher amplitudes yield a higher signal-to-noise ratio (SNR), improving measurement accuracy.

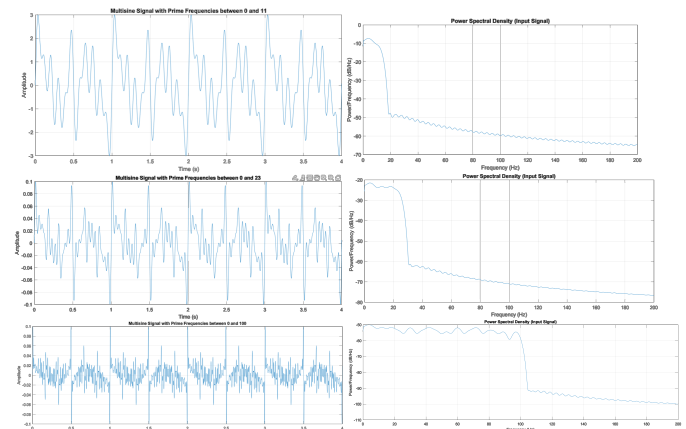


Fig. 41: Three multisine signals with their frequency contents and varying amplitudes

During the experiment, these multisine signals are applied to the SEP robot, and the resulting joint movements are recorded. By measuring the robot's output response to these perturbations, dynamic characteristics of the system are derived. Analyzing the output signals allows for the identification of key parameters and behaviours of the SEP, offering valuable insights into its dynamic response. This method leverages multisine excitation combined with prime frequencies to effectively characterize the system's response across a broad frequency spectrum.

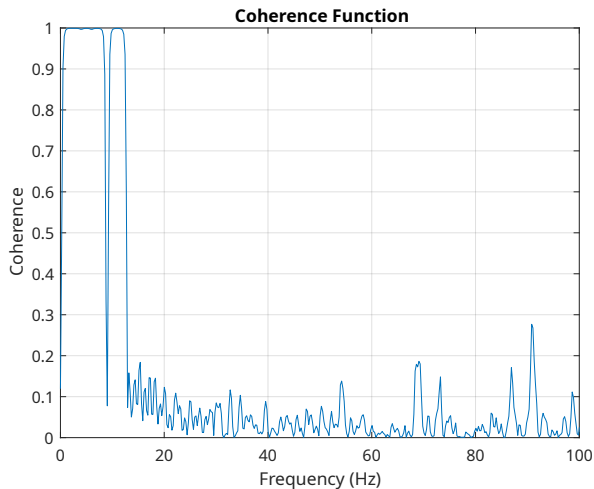


Fig. 42: High coherence for excited frequencies showing system linearity

3) *The Results:* In the system identification experiment involving the shoulder-elbow perturbator (SEP) robot running in cyclic synchronous position mode, multiple multisine signals were synthesized to investigate the dynamic response of the joint system. These signals, composed of prime frequencies ranging from 0 to 11 Hz, 0 to 23 Hz, and 0 to 100 Hz, ensure distinct frequency components, avoiding harmonic overlap and improving system identification. Signal amplitudes were set at 3° , 1° , and 0.1° , with higher amplitudes enhancing the signal-to-noise ratio (SNR) for improved measurement accuracy.

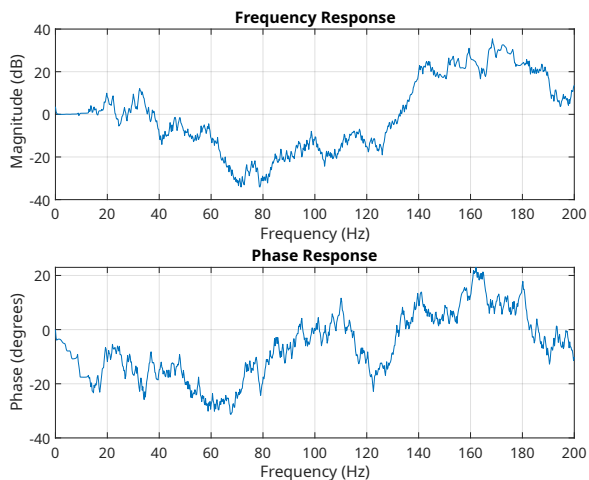


Fig. 43: Estimated transfer function of the system response as shown by the Bode plot

The coherence, shown in Figure 42, indicates a response near 1 for excited frequencies, suggesting system linearity and making open-loop system identification feasible. Despite applying adequate windowing and overlap through the Pwelch method, discrepancies appeared in the higher frequency range (≤ 20 Hz) in Figure 43, likely due to unexcited frequencies. Parametric estimation was pursued by defining the system order and selecting an appropriate model structure. Given

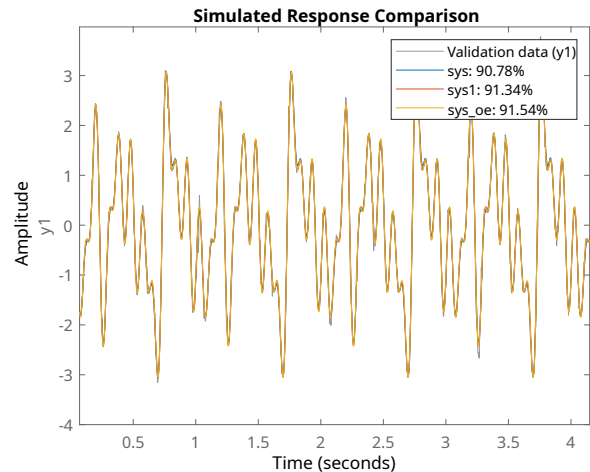


Fig. 44: Validation of various models with the original input signal

the system's behaviour, resembling a mass-spring-damper, a second-order model was selected. Based on performance in Salah (2020) [83], three models were considered:

- **ARX** (Autoregressive with Exogenous Inputs): Utilizes past inputs and outputs to predict the current output, assuming a simple structure.

$$A(q)y(t) = B(q)u(t) + e(t)$$

- **ARMAX** (Autoregressive Moving Average with Exogenous Inputs): Adds a moving average filter to the ARX model, improving noise capture.

$$A(q)y(t) = B(q)u(t) + C(q)e(t)$$

- **OE** (Output Error): Models the relationship between input and output using polynomials, minimizing the prediction error.

$$y(t) = \frac{B(q)}{F(q)}u(t) + e(t)$$

After fitting the models, all showed strong validation results, as indicated in Figure 44, with over 90% accuracy. The ARX model performed the worst at 90.78%, followed by the ARMAX model at 91.34

The system identification models and the mathematical model were validated against the frequency response of the estimated system, as shown in Figure 45. To clarify trends, the frequency response for relevant frequencies was plotted in Figure 46. In this range, the magnitude plot for the mathematical model (green) and the OE model closely aligns with the estimated system response. Phase plots for the OE, ARX, and ARMAX models align well with the estimated phase up to 11 Hz, the highest excited frequency in the experiment. Between 15 and 35 Hz, the OE model's phase plot tracks the estimated system response more closely. The mathematical model's phase shows instability without phase unwrapping.

Thus, the OE model is selected for feedforward compensation from input 'u1' to output 'y1'.

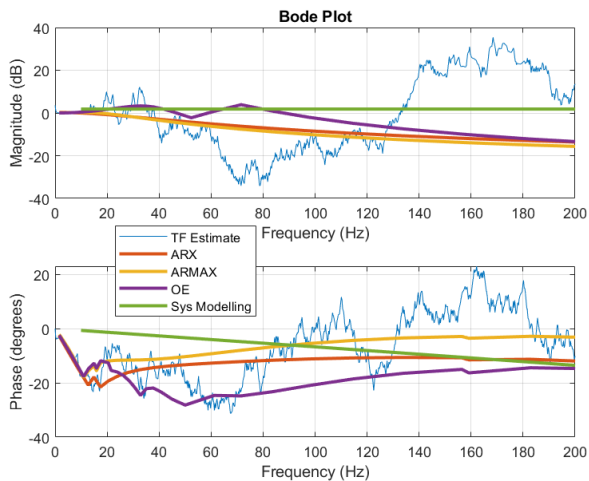


Fig. 45: Frequency response of all models, including the mathematical model

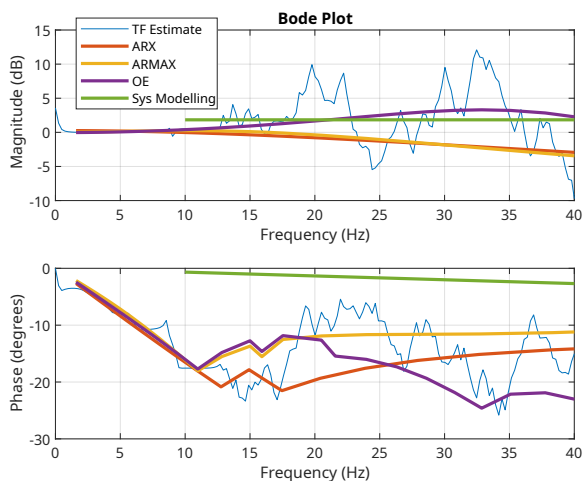


Fig. 46: FRF for frequencies of interest $\leq 40\text{Hz}$.

$$\frac{0.06367z^{-2} - 0.01066z^{-1}}{1 - 1.783z^{-1} + 0.8365z^{-2}} \quad (23)$$

4) *Key Takeaways:* While the system model effectively captures the response at lower frequencies ($<20\text{ Hz}$), it exhibits limitations at higher frequencies. Since the excited frequencies were limited to 11 Hz, modelling and discerning the system's higher frequency dynamics is challenging. This falls short of achieving the desired perturbation signals capable of exciting the system response across low, medium, and high frequencies. Consequently, the inertial and damping dynamics may not be fully captured by Equation 23.

To address this, two additional multisine inputs with higher frequency content were designed, albeit with reduced amplitudes. This trade-off was necessary to avoid damaging the 3D-printed components and linkage mechanisms. Earlier experiments revealed that excitation near the resonance frequency caused cracks in the 3D-printed housing and compromised the device's integrity due to the loosening of bolts on multiple

components, including the linkage mechanism and the frame bolt connecting the jack to the elbow perturbator.

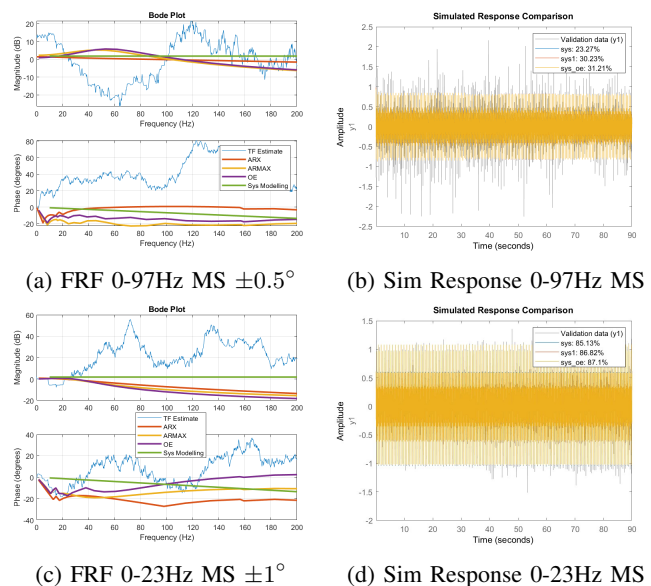


Fig. 47: Higher excited frequencies with lower amplitudes

As shown in Figure 47, the multisine signal designed for the 0 to 100 Hz range, with an amplitude of $\pm 0.1^\circ$, resulted in a poor signal-to-noise ratio (SNR), negatively affecting system identification and model validation. A compromise was reached with a multisine from 0 to 23 Hz at $\pm 1^\circ$, though this also showed suboptimal performance.

The simulated response for the 0 to 23 Hz multisine reached approximately 86%, but the frequency response did not correlate well with the estimated system response, despite good coherence. The simulated response for the 0 to 97 Hz multisine was significantly lower at 30%, with a marked difference in frequency response. These results indicate that the models are insufficient for capturing system dynamics at higher frequencies. While increasing the input signal amplitude could improve system identification, the associated risks to the device outweigh the potential benefits. Therefore, the system identification experiments are concluded at this stage.

F. Force Sensing

1) *Time Delays or Bandwidth:* For implementing the admittance control scheme on the SEP, the priority between minimizing time delays and achieving higher bandwidth depends on the specific operational requirements. Reducing time delays is critical for ensuring prompt and accurate responses to external forces, particularly in applications requiring precise force sensing and rapid adjustments. This responsiveness enhances the overall accuracy and stability of the admittance control system. In contrast, achieving higher bandwidth allows for faster tracking of dynamic force inputs, improving transparency and agility in force control tasks. However, balancing these priorities is essential to maintain stability and avoid noise amplification associated with higher bandwidth. Ultimately, minimizing time delays often takes precedence to

optimize real-time interaction and control precision, especially in diagnostic and sensitive manipulation scenarios [84].

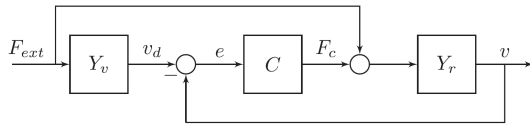


Fig. 48: The admittance control scheme starts with force input via the force sensor.

2) *Selecting an Appropriate Force Sensor for Admittance Control*: Selecting the right force sensor is crucial for effective admittance control, as shown in Figure 48. The following qualities are essential for optimal performance:

- **High Sensitivity** – Sensors must detect subtle variations in force, enabling fine-tuned control and smooth interaction.
- **Accuracy** – Sensors should deliver precise and consistent measurements with minimal errors. Drift should be minimal, and offsets can be adjusted in the control system.
- **Wide Band** – Sensors must capture a broad range of forces, from small jerks to slow, gradual applications.
- **Fast Response** – Real-time force feedback is essential for stable admittance control. Faster sensors improve the overall system’s responsiveness.
- **Robustness** – Sensors should withstand overloads, shocks, and vibrations while maintaining performance under varying environmental conditions.
- **Low Noise** – Sensors should generate minimal inherent noise to avoid the need for excessive filtering, which could introduce time delays and degrade controller performance.
- **Ease of Calibration** – Sensors must be easy to calibrate, ensuring long-term stability and consistent accuracy over time.
- **Miscellaneous** – Additional considerations include cost, compatibility with existing systems, ease of integration, and the availability of mechanical integration packages.

3) *Piezoelectric vs Straingauge*: The Rijndam SEP is equipped with two force sensors: the Futek LCM 200 strain gauge load cell and the Kistler 9237B piezoelectric force transducer. Table VI outlines the general specifications of these sensors. The Kistler piezoelectric transducer offers superior speed, sensitivity, and accuracy, making it more robust for high-precision, dynamic measurements. In comparison, the LCM 200 with the SG3016 conditioner provides high accuracy for static or slowly varying forces but operates with lower resolution.

The Kistler 9321B/5073A combination excels in applications requiring a broad dynamic range and fast response times, ideal for real-time feedback. In contrast, the LCM 200 system is more suited for static or low-dynamic scenarios, though it struggles with high-speed measurements.

While the Kistler system offers exceptional durability, it is more sensitive to environmental factors, such as temperature fluctuations and noise. The Futek LCM 200, although robust, is more prone to electrical noise if not adequately isolated.

Integrating the Kistler system involves greater complexity and cost, but it delivers unmatched performance for high-precision applications. The LCM 200, on the other hand, is easier and more cost-effective to integrate, making it suitable for scenarios where budget and simplicity take priority.

For the SEP, the Kistler combination is ideal for high dynamic performance, sensitivity, and precision. The Futek combination, however, is more appropriate for applications involving static or slowly varying forces, where cost-effectiveness and ease of integration are more critical.

4) *Experimental Validation of Force Sensors*: To validate the performance metrics of the force sensors, a series of experiments will be conducted based on the desired properties outlined in Section VIII-F-2.

The following experiments are planned:

- **Both Sensors Operational** – The Kistler sensor, currently not electrically connected, will be connected to the terminals, coupler, and power supply to ensure force data can be recorded.
- **Calibration** – Calibration tests will be performed using springs or masses with known weights to assess the accuracy of both sensors.
- **Drift Comparison** – The sensors will be preloaded for an extended duration to evaluate any drift that may occur over time.
- **Impulse and Oscillatory Response** – Impulse Response Function (IRF) and Frequency Response Function (FRF) experiments will be conducted to characterize the sensors. The robot will be connected to a pulley system to introduce perturbations, and the sensors’ responses will be analyzed.
- **Perturbation Signal Response** – Multiple sine waves will be applied to the robot in continuous synchronous position mode to determine how effectively each sensor tracks disturbances.

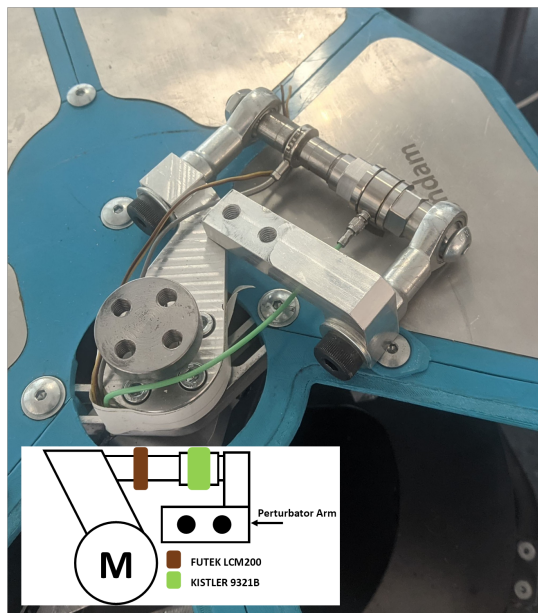
These experiments will provide a thorough evaluation of the sensors’ performance, ensuring the most suitable sensor is selected for the SEP’s admittance control system.

Figure 49 illustrates both sensors laid out in series. While the Futek LCM200 was already connected, the Kistler 9321B was initially disconnected. To integrate the Kistler 9321B, it was connected to the Kistler charge amplifier 5731A, which was configured to record force data in the same $\pm 10V$ range as the ICPDAS SG3016 to ensure consistency between the sensors. The Kistler sensor was first tested on a lab bench, and once signals were verified via a digital multimeter and powered by an external 12V DC supply, the charge amplifier was integrated into the SEP Rijndam system. The wiring schematics are shown in Figure 49b.

5) *Calibration and Drift Experiments*: To conduct the calibration test, the test manager program is first modified to include additional offset calibration for the Kistler force sensor. The charge amplifier is configured to output in mV/V, ensuring a valid comparison between the Futek and Kistler sensors. The SEP arm is moved to an end stop, and springs are attached as shown in Figure 50. A spring weight gauge is connected in series to measure the applied force.

TABLE VI: Comparison of FUTEK LCM 200 with ICPDAS SG3016 and Kistler 9321B with 5073A

Sensors	LCM 200 with ICPDAS SG3016	Kistler 9321B with 5073A
Type	Strain Gauge	Piezoelectric Force Transducer
Force Range	1.1 kN	± 2.5 kN
Output	mV/V	mV/V
Natural Frequency	26.8 kHz	55 kHz
Accuracy	± 0.05 within measuring range	$\leq \pm 0.05$ within measuring range
Resolution	4.88 mV	2 mV
Bandwidth	600 Hz (Conditioner limited)	20 kHz
Size and Weight	17 g	90 g
Signal Conditioner	ICPDAS SG3016	Kistler 5073A
Conditioner Features	12-bit resolution, up to 600 Hz sampling rate, RS-485 Modbus RTU	High resolution, high sampling rate, analog and digital outputs, RS-232 Modbus
Cost	€1237	€3800



(a) Both sensors lcm 200 (left) and 9231b (right) on SEP Rljndam

(b) Wiring scheme for force sensor on SEP

Fig. 49: Initial Experimental setup

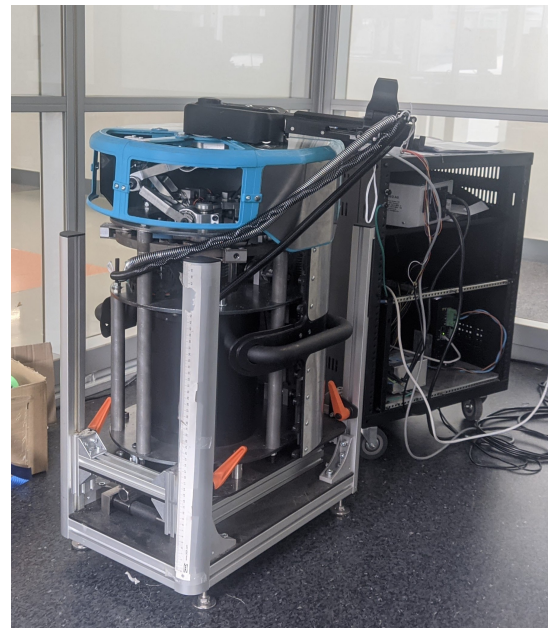


Fig. 50: Calibration and drift set up

allowing for extended data collection without generating an overly large dataset, given the system's limited memory. Once the configuration was complete, the drift experiment began.

Initially, the SEP is powered on, the sensors are calibrated, and any offsets are removed. The sensors are left to idle for 30 seconds before loading the arm with a spring applying approximately 25 kg of force. This setup remains in place for nearly 15 hours. Afterwards, the force is removed, and the SEP is again left idle for an additional 20 minutes to observe any drift.

Figure 51 reveals several key observations. In Figure 51b, there is a noticeable variation between the initial sensor loading and the eventual settling value. This indicates that the sensors, or potentially the signal conditioner/amplifier, require a longer warm-up period to reach optimal operating conditions—an important consideration for participant or patient testing. In Figure 51c, after the load was removed the next day,

The SEP's data logging service is set to record at 1 Hz,

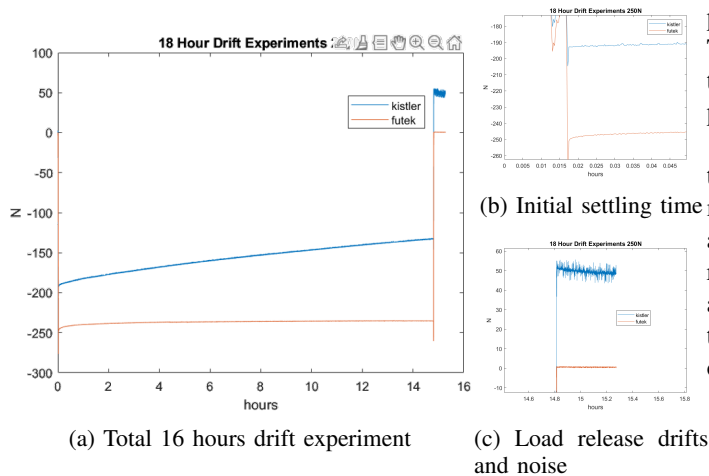


Fig. 51: Drift experiment results with areas of interest magnified on the right

the Kistler sensor showed significantly more periodic noise spikes compared to its behaviour during the settled phase of the drift experiment.

Although both sensors initially exhibited an offset, the piezoelectric Kistler sensor experienced significantly more drift during the settled phase compared to the strain gauge-based Futek sensor. The Kistler sensor initially settled at -186.61 N and drifted to -131.76 N, indicating a drift of 54.85 N. In contrast, the Futek sensor settled at -241.77 N and drifted to -235.52 N, resulting in a much smaller drift of 6.25 N. When the load is removed, the Futek sensor returns to an average of 0 N ± 0.4 , while the Kistler sensor displays a residual force of 48.55 N ± 5 .

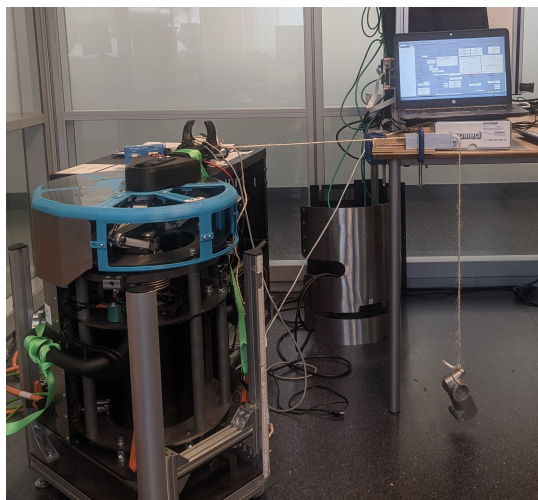


Fig. 52: The impulse experiments where the impulse is provided via a cable pulley load mechanism.

6) *Impulse Experiments:* To validate the frequency response of the sensors, an impulse response test is conducted. Since an impulse excites the entire frequency band (low, medium, and high frequencies), it is an effective method for evaluating sensor performance. The impulse is generated by locking the SEP arm near an end stop and attaching a cable

pulley perpendicular to the arm, with a mass on the other end. The arm is tightly secured with ratchet straps to ensure that the entire impulse acts directly on the sensors, minimizing parasitic damping or stiffness effects, as shown in Figure 52.

Once the setup is secured, the weight is dropped, and the force response is recorded. This experiment is repeated multiple times. Before each test, the sensors are calibrated, and the load is held for 10 seconds to establish a stable idle response. The weight is then dropped, and the response is allowed to settle for 20 seconds. This process is repeated five times to ensure reliable results and allow for averaging in case of persistent periodic noise.

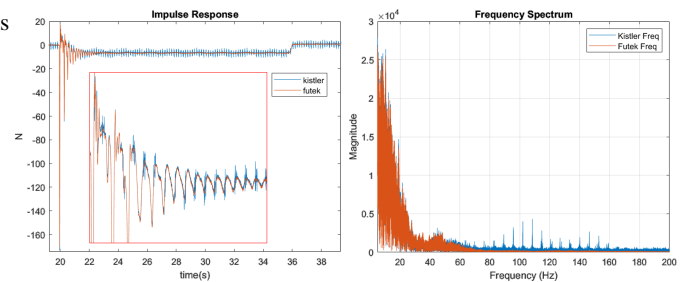


Fig. 53: One cycle of the impulse response illustrated (left) and the frequency spectrum (right).

Figure 53 shows the impulse response and corresponding frequency spectrum of the sensors, with excited frequencies ranging from 0 to approximately 80 Hz. This range is sufficient for determining the system's dynamic response. The force profiles for both sensors are nearly identical, indicating good calibration between the two sensor types. However, periodic noise remains evident in the Kistler sensor, which could lead to undesirable behaviours in the admittance controller. This noise is observed as frequency spikes around 100 Hz, resembling harmonics.

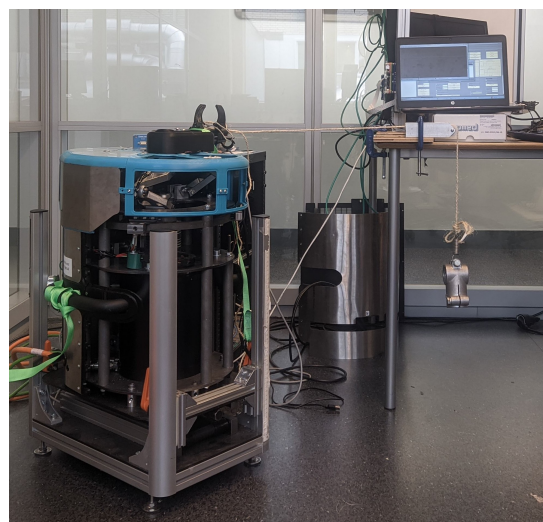


Fig. 54: Similar setup to the impulse response with the addition of a spring in series between the load and SEP arm.

7) *Oscillatory Experiments:* In a setup similar to the impulse experiments, adding a spring between the mass and the

SEP arm induces an oscillatory response, enabling observation of the system’s low-frequency behaviour and its damping characteristics. A theoretically rigid system would allow infinite oscillations with an ideal spring, while a compliant system would exhibit rapid damping.

A helical spring was introduced between the mass and the cable, as shown in Figure 54. After calibrating both sensors, the load is pulled close to the ground, applying tension to preload the system. Following a 10-second preload, the load is released, allowing natural oscillations to occur. The system is allowed to oscillate for 30 seconds until the motion ceases. This procedure was repeated five times to ensure reliable data collection.

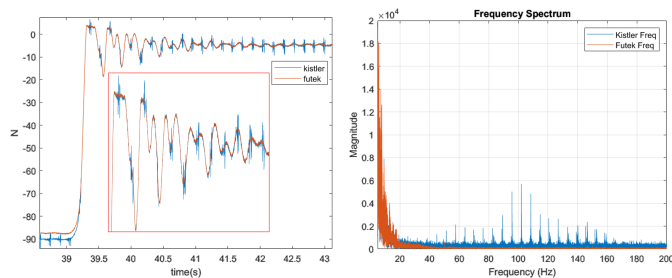


Fig. 55: One cycle of the oscillatory response illustrated (left) and the frequency spectrum (right).

As with the impulse experiments, the oscillation tests produce similar results. Figure 55 shows the excited frequencies, which are primarily at the lower end of the spectrum. This is notable since humans typically cannot respond to frequencies above 20 Hz, even in spastic conditions.[85] The force tracking between the strain gauge and piezoelectric sensors remains nearly identical. However, noise is more prominent in this experiment, particularly in the frequency spectrum, where Gaussian noise is centred around 100 Hz.

A slight variation in the extremities of the loading scenario is observed, with the sensors reporting slightly different loads of -90 N and -88 N, respectively. Another significant finding is the rapid damping of the oscillations, despite the end-effector being securely fastened with straps. This suggests high internal damping within the system, due to compliance in the setup or slack in the ratchet straps.

8) *Bandwidth Tests:* For the bandwidth tests, the SEP is subjected to a $\pm 1^\circ$ sine wave ranging from 1 Hz to 10 Hz. The frequency is limited to 10 Hz to avoid physical damage to the 3D-printed components of the system. And to maintain its structural integrity

As shown in Figure 56, significant electromagnetic interference (EMI) impacts the Kistler sensor wiring, particularly when the servo drive is activated. The noise level spikes dramatically, rendering the low-frequency response in Figure 56b unusable for the Kistler sensor when compared to the Futek sensor. The performance improves at higher frequencies, as seen in Figure 56c, but periodic noise remains a persistent issue.

9) *Key Takeaways:* Despite the piezoelectric sensor’s superior specifications, as shown in Table VI, its response was significantly affected by noise interference. This noise

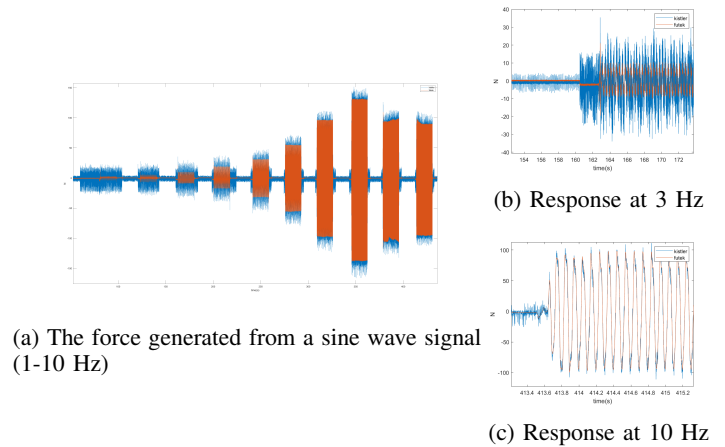


Fig. 56: The complete bandwidth experiment on left and low/higher frequency response on right.

compromised the sensor’s performance, making it less reliable for precise measurements compared to the strain gauge sensor.

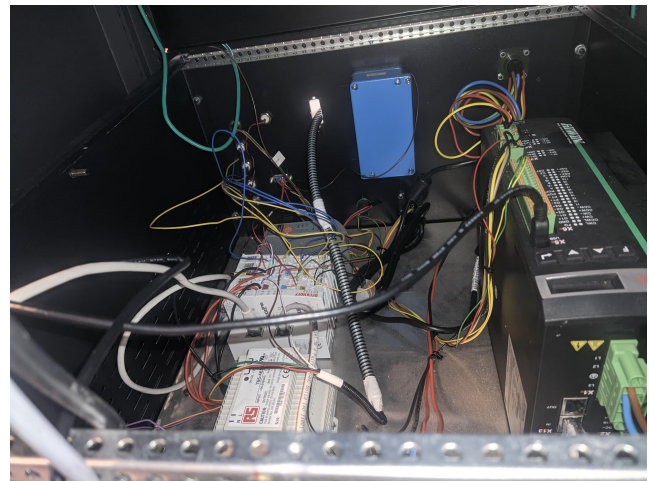


Fig. 57: Shielding for the sensor wires inside the SEP main-frame.

As shown in Figure 57, attempts were made to reduce the noise by externally grounding the charge amplifier and shielding the sensor wires to attenuate electromagnetic interference (EMI) when the motor was activated. An external 24V DC power supply was added to the Hiwin ED1 drive, which eliminated motor-induced noise, though the periodic noise persisted.

Post-processing techniques such as notch filtering based on the power spectral density, Empirical Mode Decomposition (EMD), and Wavelet decomposition were applied to remove noise. However, the periodic noise was traced to the charge amplifier itself, as the noise remained even after disconnecting the piezoelectric sensor. While analog filtering through RC filters within the charge amplifier was considered [86], this solution is not ideal given the high cost of the Kistler system, which is three times that of the Futek sensor.

These post-processing methods introduce additional delays, which is highly undesirable for implementing negative inertia

on the SEP. In contrast, the Futek strain gauge, based on experimental results, demonstrates adequate performance. With an eigenfrequency of 26 kHz and a signal conditioner sampling rate of 600 Hz on the SEP Rijndam, the Futek system is capable of handling the requirements. The signal conditioner is upgraded on the SEP Amsterdam to the Futek IAA100, which supports a minimum sampling rate of 1 kHz.

However, running the Simulink model and signal amplifier at 1 kHz introduces risks of aliasing, especially if the signal contains components near or above 500 Hz. Additionally, leakage can occur if sampling is not perfectly synchronized with the signal. Therefore, a higher sampling rate for the Simulink model is recommended to mitigate these issues. Overall, the Futek strain gauge is sufficient for the admittance controller with negative inertia implementation.

G. Accelerometer and Filtering

1) *Accelerometer*: An effective admittance controller requires a robust inner velocity loop to enforce the desired velocity derived from virtual dynamics. Accurate feedback for position, velocity, and acceleration is essential for effective error compensation. While a high-resolution motor encoder provides precise position data, combining it with a gyro or accelerometer can enhance multimodal sensory output when an encoder alone is insufficient. By integrating accelerometer data twice, position values can be estimated, and a Kalman filter can further improve the accuracy of position estimation through sensor fusion.

The accelerometer, as shown in Figure 59, provides direct acceleration measurements, which offer several advantages. Compared to deriving acceleration from force data, direct measurement yields more accurate dynamic responses. With a sampling rate of 1000 Hz, compared to 500 Hz from force-derived values, having dual sources of acceleration data enhances noise rejection and improves the controller's ability to distinguish between noise and actual dynamics. This accurate acceleration feedback allows the controller to better compensate for external disturbances and unmodeled dynamics, improving robustness.

Implementing negative inertia on the Series Elastic Actuator (SEA) can destabilize the system by reducing the effective mass. Accurate acceleration disturbance observers help counteract this destabilization, preventing instability and unwanted oscillations. Additionally, acceleration data allows for real-time adjustment of damping coefficients, enhancing stability as demonstrated by Keemink et al. (2018) [24].

To evaluate the suitability of integrating a gyro or accelerometer with the SEA, the following experiments are proposed:

- **Data Accuracy and Noise Filtering**: Mount each sensor on the robot and collect position data during controlled movements. For the ADXL337, double integrate the acceleration data to obtain the position. For the GY-521, track the angular position using the gyroscope and integrate the accelerometer data to obtain the linear position. Compare these position estimates with high-resolution encoder data to assess accuracy and noise levels.

- **Sensor Fusion and Drift Compensation**: Use a Kalman filter to fuse data from the GY-521 accelerometer and gyroscope. Test the robot through dynamic motions to evaluate the effectiveness of sensor fusion in reducing drift and improving accuracy compared to the ADXL337 alone. Analyze the stability and consistency of position and velocity estimates over extended periods.

These experiments will determine which sensor provides the most accurate and reliable position and velocity feedback for the SEP's admittance control requirements.

The ADXL337, shown in Figure 59 accelerometer is mounted at the distal end of the SEP end effector with a radius of 0.298 m. Wiring follows the scheme in Figure 10, with an external 5V adapter stepping down to 3.3 V via a voltage divider, stabilized by a 100 nF ceramic capacitor to minimize noise in the accelerometer output. The output is converted to degrees per second squared ($^{\circ}/s^2$) using the following equation:

$$Acc = \frac{Measured\ signal - Zero_g\ Bias}{Sensitivity} \times \frac{g}{Radius} \times Rad2deg \quad (24)$$

where:

$$Zero_g\ Bias = 2900$$

$$Sensitivity = 340\ mV = 466.67$$

$$g = 9.81\ m/s^2$$

$$Radius = 0.298\ m$$

$$Rad2deg = \frac{180}{\pi} = 57.295$$

From Figure 58, the raw accelerometer signal contains significant noise, particularly for the multisine signal, which is expected. A moving average filter highlights the underlying trends, which align more closely with the ground truth (sine/multisine waves). However, filtering introduces a 100 ms delay and phase lag, which can impair performance. Therefore, minimal filtering is applied. Kalman filtering with position encoder data can reduce noise further but introduces additional phase lag, delaying the accelerometer's measurements.

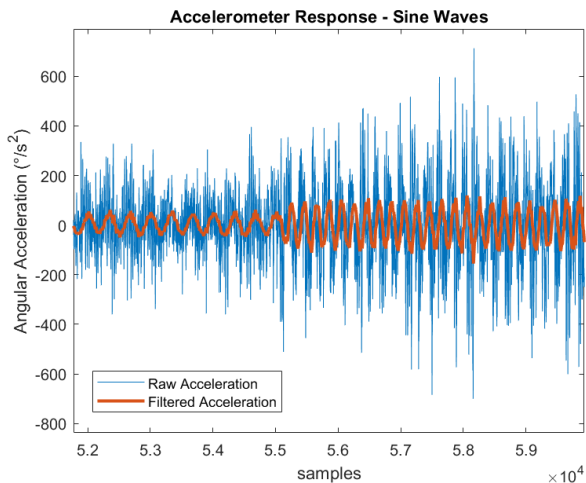
2) *Kalman Filter Tuning*: A Kalman filter is designed to minimally filter the raw data, providing a smoother acceleration prediction, as illustrated in Figure 60.

The first state-space model is a theoretical representation based on basic physical principles. The state vector \mathbf{x} includes position (p), velocity (v), and acceleration (a):

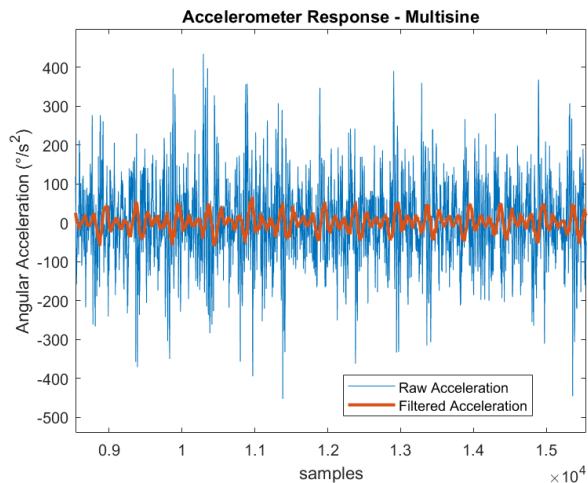
$$\mathbf{x}(k) = \begin{bmatrix} p(k) \\ v(k) \\ a(k) \end{bmatrix}$$

The system dynamics are described by the following state-space matrices:

$$\mathbf{A} = \begin{bmatrix} 1 & \Delta t & 0 \\ 0 & 1 & \Delta t \\ 0 & 0 & 1 \end{bmatrix}, \quad \mathbf{B} = \begin{bmatrix} 0 \\ 0 \\ 1 \end{bmatrix}, \quad \mathbf{C} = \begin{bmatrix} 1 & 0 & 0 \\ 0 & 1 & 0 \\ 0 & 0 & 1 \end{bmatrix}$$



(a) Sine waves at two different frequencies.



(b) Periodic multisine signal.

Fig. 58: Raw and filtered accelerometer response.

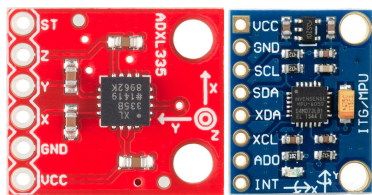


Fig. 59: The ADXL337 (left) and the MPU6050 (right).

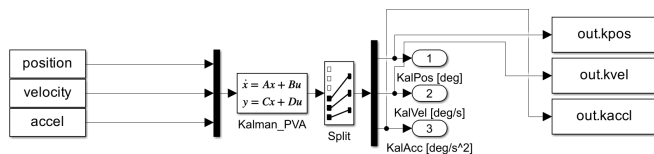


Fig. 60: The Kalman filter gain tuning scheme.

Here, Δt represents the sampling time. The process noise covariance matrix \mathbf{Q} and the measurement noise covariance matrix \mathbf{R} are tuned based on sensor characteristics and experimental data:

$$\mathbf{Q} = \begin{bmatrix} q_1 & 0 & 0 \\ 0 & q_2 & 0 \\ 0 & 0 & q_3 \end{bmatrix}, \quad \mathbf{R} = \begin{bmatrix} r_p & 0 & 0 \\ 0 & r_v & 0 \\ 0 & 0 & r_a \end{bmatrix}$$

A second state-space model is developed through system identification techniques, providing a more accurate empirical representation of the system dynamics. The identified system matrices are:

$$\mathbf{A}_{id} = \begin{bmatrix} 2.786 & -1.301 & 0.8157 \\ 2 & 0 & 0 \\ 0 & 0.5 & 0 \end{bmatrix}, \quad \mathbf{B}_{id} = \begin{bmatrix} 0.5 \\ 0 \\ 0 \end{bmatrix}$$

$$\mathbf{C}_{id} = \begin{bmatrix} 0.1879 & 0 & 0 \\ 0 & -0.1614 & 0 \\ 0 & 0 & 0.1367 \end{bmatrix}$$

The process and measurement noise covariances for the identified model are similarly adjusted:

$$\mathbf{Q}_{id} = \begin{bmatrix} q_{id1} & 0 & 0 \\ 0 & q_{id2} & 0 \\ 0 & 0 & q_{id3} \end{bmatrix}, \quad \mathbf{R}_{id} = \begin{bmatrix} r_{id} & 0 & 0 \\ 0 & r_{id} & 0 \\ 0 & 0 & r_{id} \end{bmatrix}$$

H. Cascaded Control

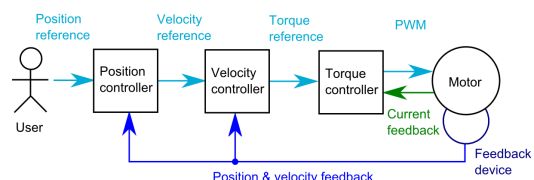


Fig. 61: The cascaded control loop

Servo drives typically utilize cascaded control loops to achieve optimal performance, as depicted in Figure 61. While the operation for the ED1 servo drive in the SEP is shown in Figure 62. These loops include:

- **Torque Loop:** The torque loop, also known as the current loop, operates with the highest bandwidth (16x higher than the position loop). It processes the desired torque from the velocity loop and outputs the necessary current to the servo motor, independent of position or velocity. Factory settings, particularly with Hiwin components, usually optimize torque loop parameters, though input filters can be adjusted based on the load.
- **Velocity Loop:** The velocity loop, with a bandwidth 4x higher than the position loop, adjusts torque to achieve

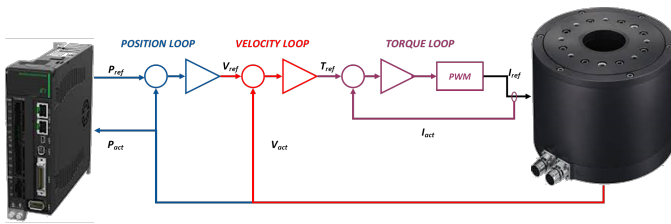


Fig. 62: The breakdown of the three loops within the SEP framework. The position loop is controlled via the Simulink model while both the velocity and torque loops are managed internally by the Hiwin servo drive

the desired velocity. This loop is load-tuned, taking its reference from the position loop.

- **Position Loop:** The position loop operates with the lowest bandwidth, generating a reference velocity from the position error. It is also tuned to the load.

The SEP operates in Cyclic Synchronous Velocity mode, with a Simulink model that includes drift compensation for precise position and velocity control. In this setup, Simulink controls the position loop. The Hiwin ED1 drive can run at 3.2 kHz in the torque loop, 1 kHz in the velocity loop, and 0.1 kHz in the position loop. If configured for torque control within the current framework, sampling and bandwidth limitations arise. The torque controller would operate at 1 kHz, which, by the Nyquist-Shannon criterion, would be effective until 500 Hz, reducing the velocity loop's effective bandwidth to 125 Hz and the position loop's bandwidth to 31.25 Hz.

I. Alternate Results

To evaluate the mitigation strategies for inertia, a virtual dynamic model is set with the following parameters:

- Mass: $m = 0.30 \text{ kg}$
- Damping: $b = 10 \text{ N} \cdot \text{s}^{-1}$
- Stiffness: $k = 100 \text{ N/m}$

The SEP arm is perturbed by pulling it $\pm 10^\circ$, and a trigger is pressed as soon as the arm is released to ensure that arm properties do not affect the results. Several trials are conducted within a 90-second window to ensure a sufficiently large data set from which the Frequency Response Functions can be obtained.

From Figure 63, the initial response resembles a standard mass-spring-damper system, for both the red and green responses. The system has a stiffness slightly lower than 0 dB, there is a small damping trough at the cross-over frequency 20 Hz after which the slope is +2 indicating normal inertia. The higher frequencies are not excited in this test therefore clear and accurate judgment cannot be made due to lower coherence.

Critical inertia compensation is evaluated by setting the accelerometer-based mass compensation to 0.30 kg as the base scenario. This cancels out the virtual mass set in the virtual dynamics block. Subsequently, augmenting it with inherent inertial compensation from the model. This removes the device's total inertia from the system. After which the

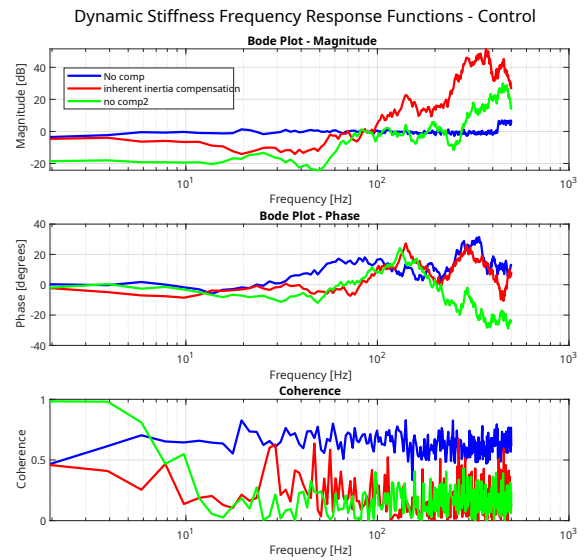


Fig. 63: Control group for the dynamic stiffness FRF

motor torque-based disturbance rejection is included to ensure stability.

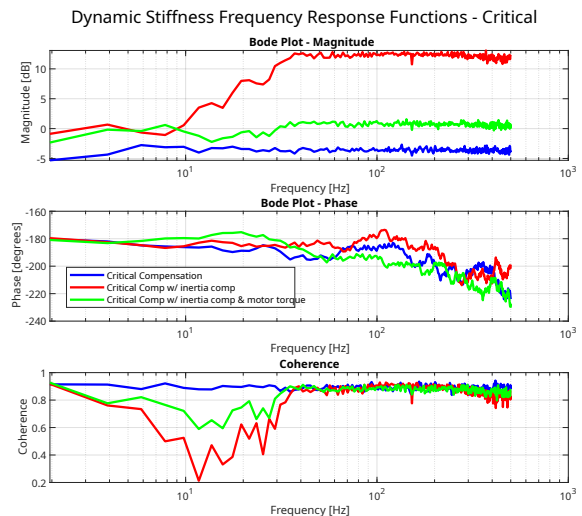


Fig. 64: Dynamic stiffness FRF for critical compensation strategies

In Figure 64, there is good coherence for the critical compensation in blue and the critical compensation with inherent inertia compensation and disturbance rejection in green. These two responses, especially the green plot, show a straight line for all frequencies around 0 dB which is expected. Only providing critical inertia compensation (shown in blue) shows the presence of some stiffness in the system by the response at -5 dB. The phase plots for the relevant frequencies which are $\leq 20 \text{ Hz}$ show a slight phase lag at the lower frequencies but remain close to zero. The response for the green plot shows a slight phase lead indicating some negative inertia characteristics.

For negative inertia compensation, the accelerometer force compensation is increased to 0.50 kg, creating approximately 200 grams of negative inertia. This experiment is repeated to evaluate the difference in performance.

Dynamic Stiffness Frequency Response Functions - Negative Inertia

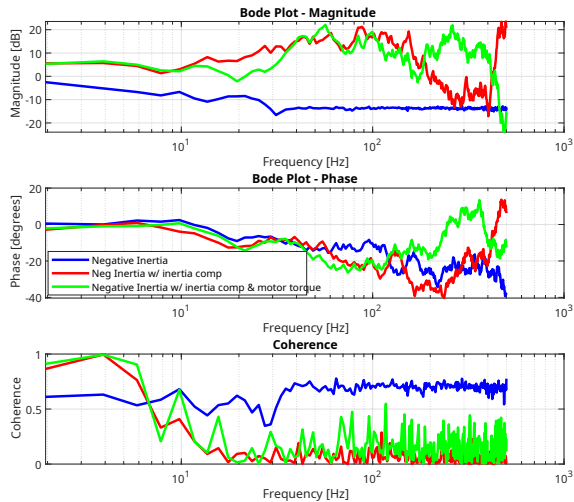


Fig. 65: Dynamic stiffness for negative inertia

Dynamic Stiffness Frequency Response Functions - Comparison

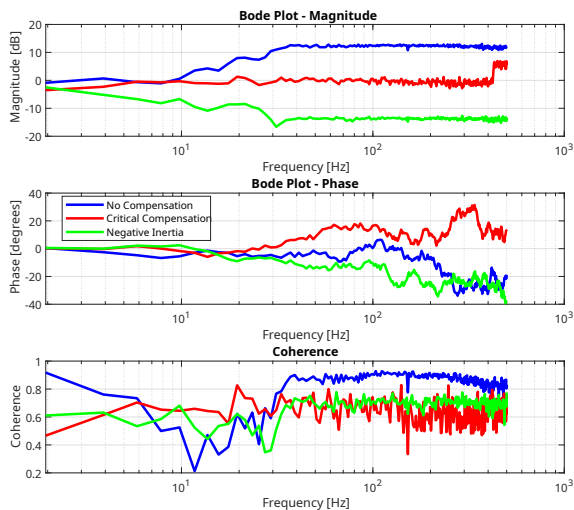


Fig. 66: Comparison of no compensation, critical compensation, and negative inertia for the dynamic stiffness FRF

Figure 65 indicates a few key trends, initially for the responses in green and red, the stiffness starts at a +8 dB showing some negative stiffness in the system. After this, there is a slight trough at 8 Hz for both responses showing some positive damping. From here the results diverge slightly. They both have a -2 slope, the red plot has it until 30 Hz while the green slope has it until 20 Hz. After this, the response is incoherent due to low coherence. The blue plot however has the highest coherence, it starts with some positive stiffness and has a peak at 10 Hz (crossover frequency) before a clear -2

slope up until 30 Hz, after which there is a gradual negative slope for the unexcited higher frequencies. Another sign of the presence of negative inertia is the positive phase lead from 12 Hz to 36 Hz, further indicating the presence of negative inertia in the system.

Finally, comparisons of no compensation, critical compensation, and negative inertia are shown in Figure 66. Trends suggest that coherence at higher frequencies is insufficient for conclusive results, but the presence of negative inertia becomes more apparent when compared with the other test cases.

Coherence at higher frequencies requires improvement of higher-frequency excitation. Variations in responses within similar trails highlight the need for precise triggering to capture significant signals. Comparing coherent results clarifies the differences between rendered virtual inertia, critical inertia (0 Kg) and negative inertia.

J. The Initial Admittance Controller

This subsection contains the initial controller scheme for the admittance controller.

- Figure 67 shows the admittance controller.
- Figure 68 shows the motor initialization block.
- Figure 69 shows the force input block, similar blocks are used for accelerometer for calibration.
- Figure 70 shows the virtual dynamics block.
- Figure 71 shows the velocity controller.

K. The Inertia Compensation Admittance Controller

- Figure 72 shows the modified velocity controller with feedforward dynamics.
- Figure 73 shows the complete admittance framework with inertia compensation.
- Figure 74 shows the inertia compensation block.
- Figure 75 shows the deadband PDFs for finding an optimal deadband.

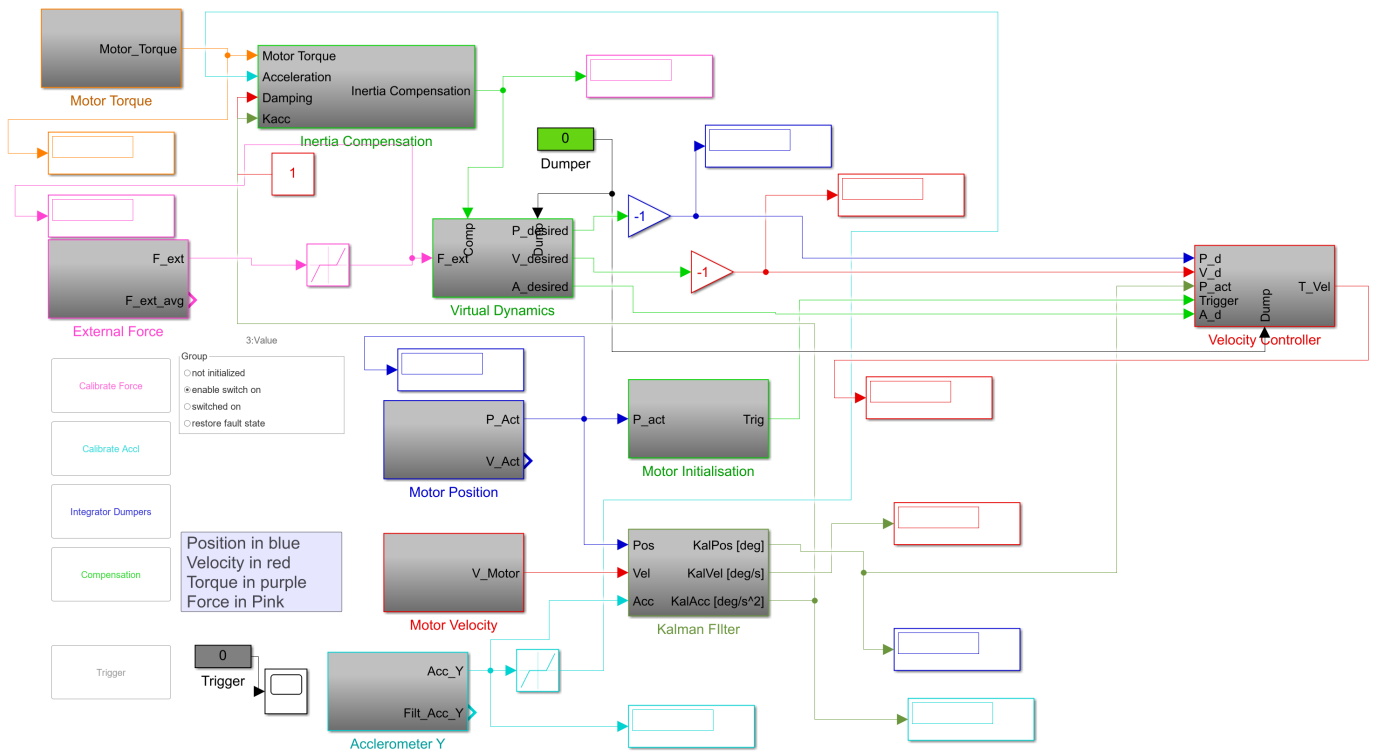


Fig. 67: The initial admittance controller framework in Simulink with external force block as an input, virtual dynamics creating the desired reference, velocity controller enforcing it and rest of the modules augmenting the operation

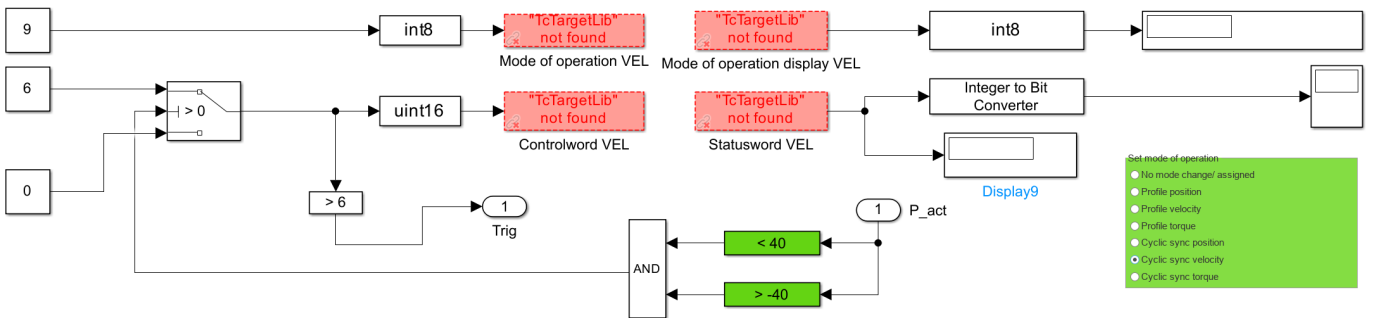


Fig. 68: Motor Initialization

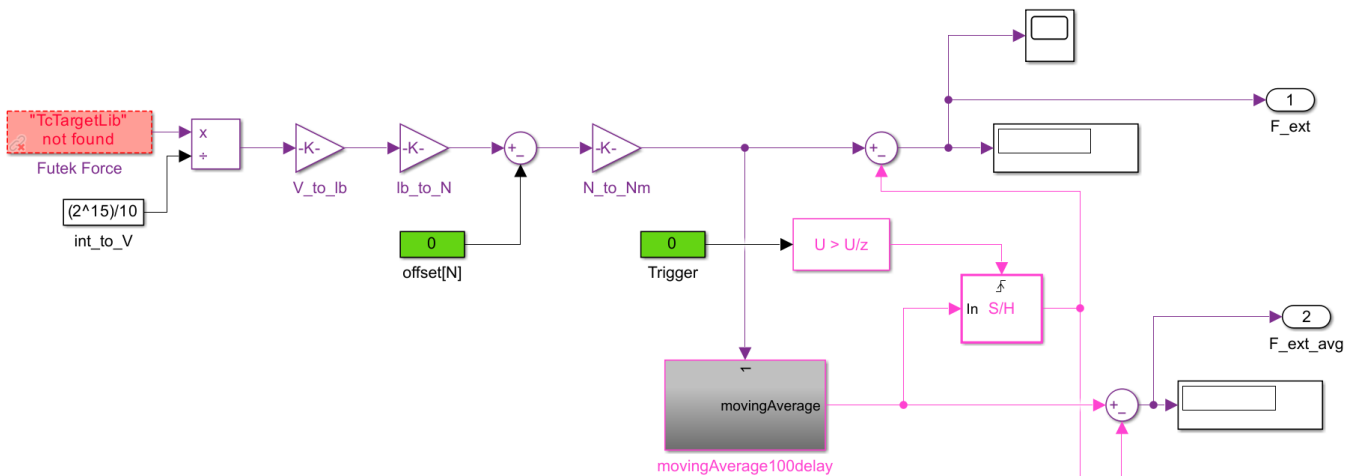


Fig. 69: External Force

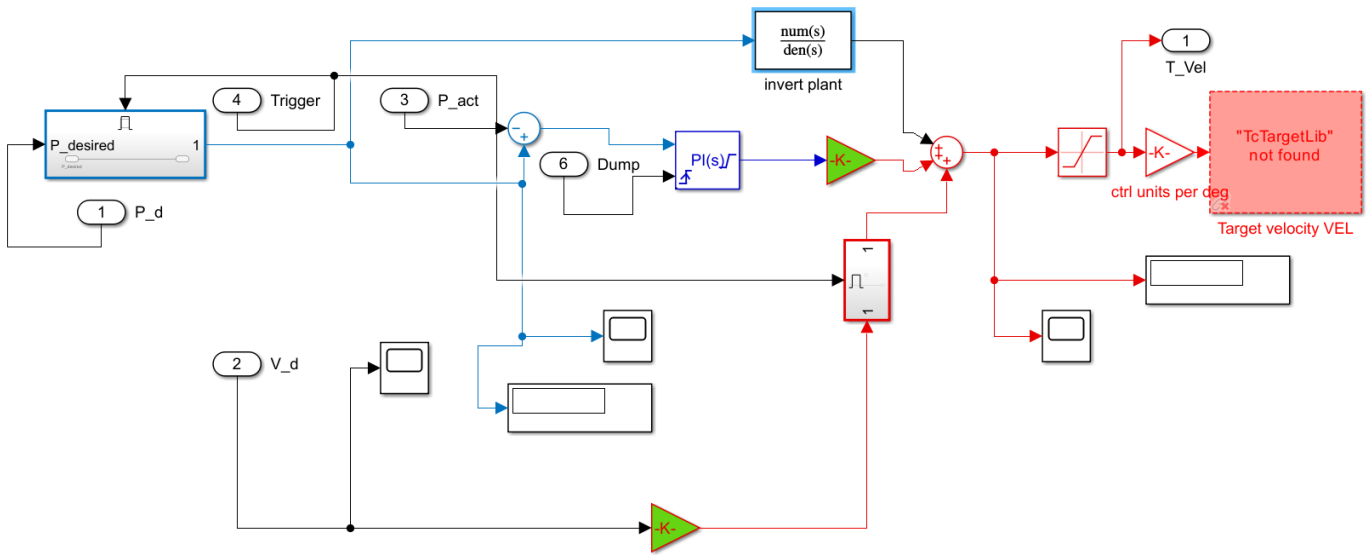


Fig. 72: The inverted plant with a second-order lowpass filter combined with feedback controller to improve system dynamics

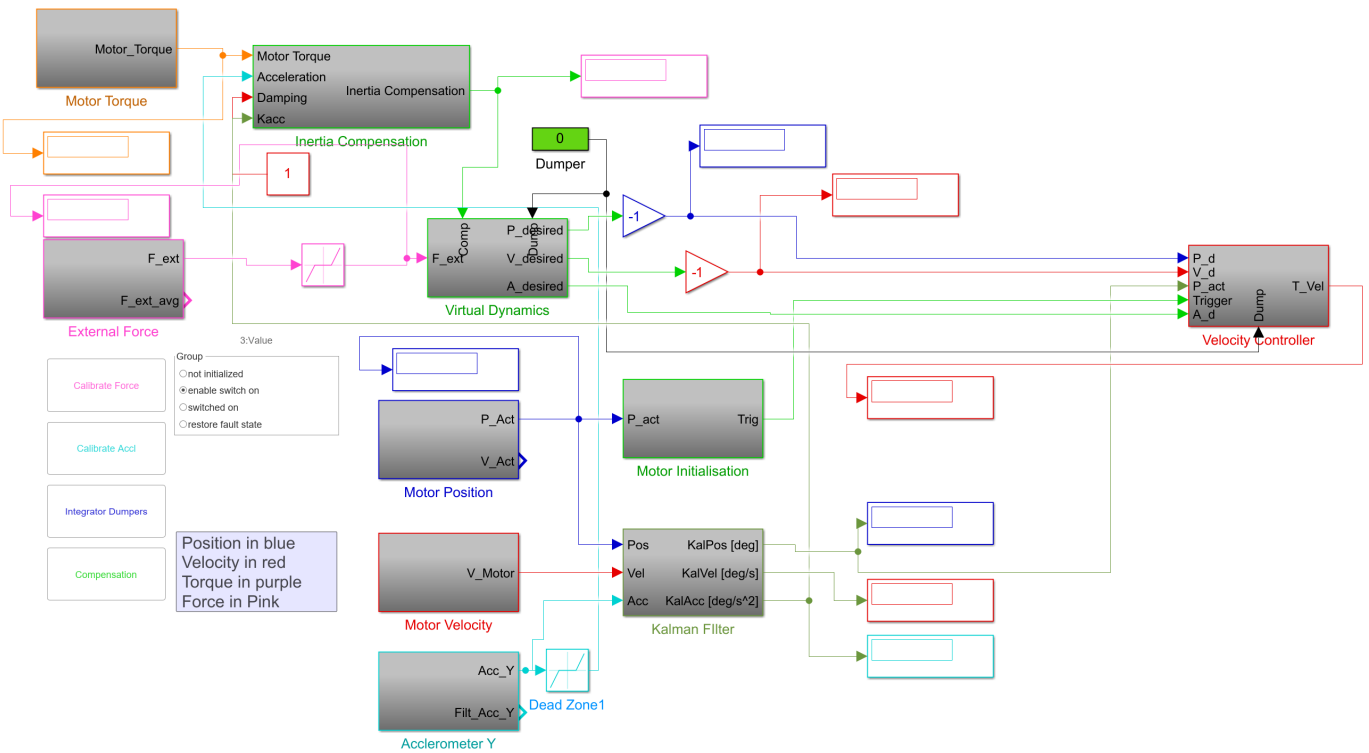


Fig. 73: Complete control scheme with inertia compensation block

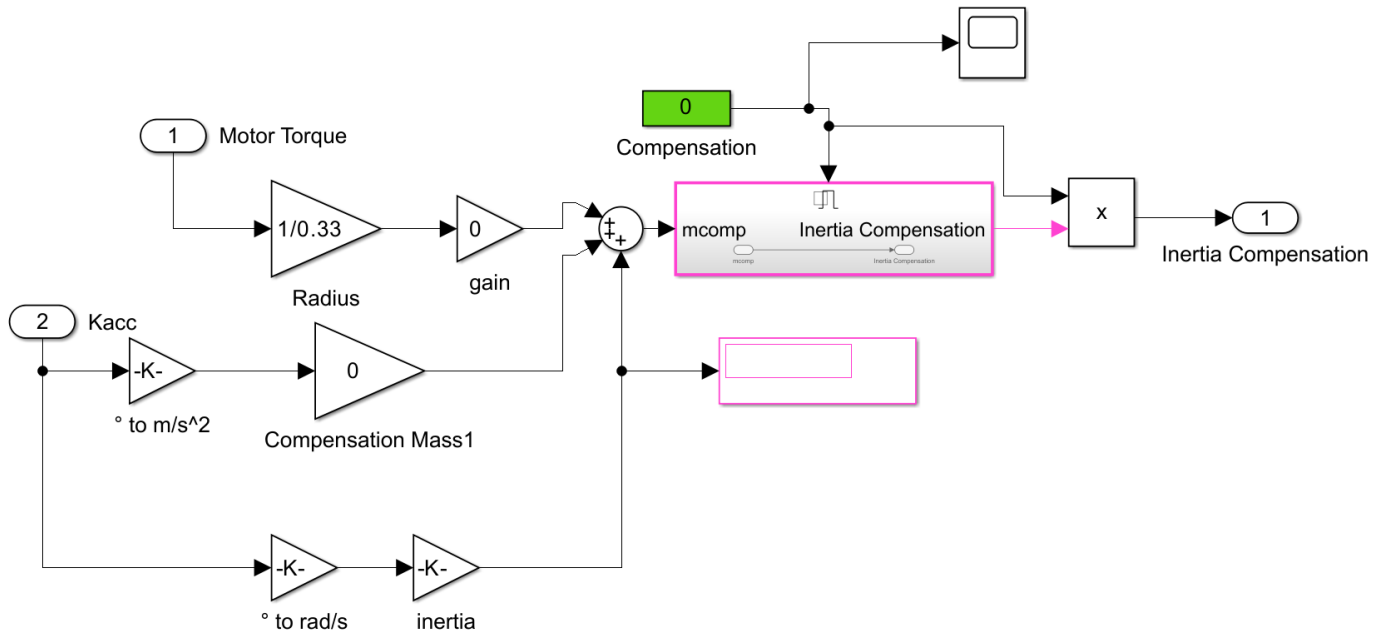
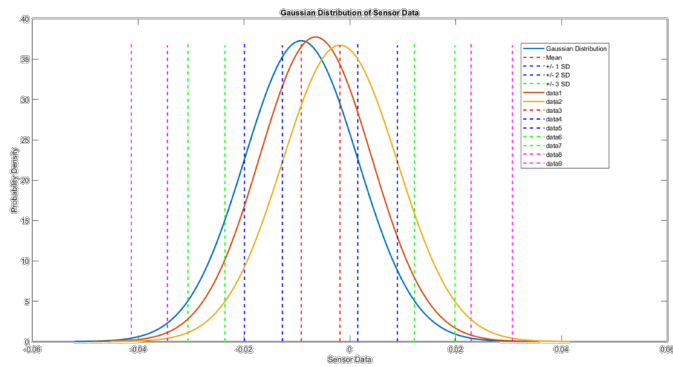
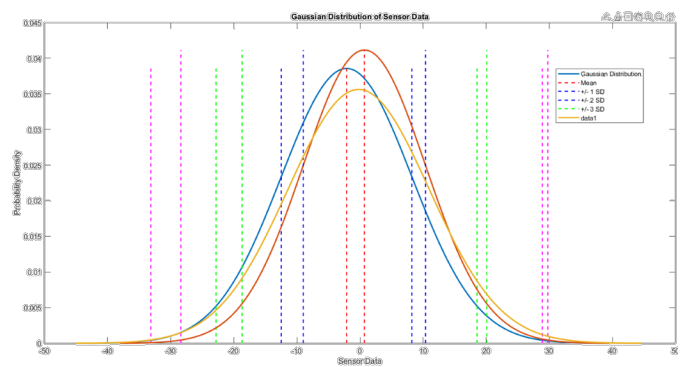


Fig. 74: Inertia compensation block



(a) Probability density function for force sensor



(b) Probability density function for accelerometer

Fig. 75: PDF analysis to determine safe noise levels for deadband implementation